



저작자표시-비영리-변경금지 2.0 대한민국

이용자는 아래의 조건을 따르는 경우에 한하여 자유롭게

- 이 저작물을 복제, 배포, 전송, 전시, 공연 및 방송할 수 있습니다.

다음과 같은 조건을 따라야 합니다:



저작자표시. 귀하는 원저작자를 표시하여야 합니다.



비영리. 귀하는 이 저작물을 영리 목적으로 이용할 수 없습니다.



변경금지. 귀하는 이 저작물을 개작, 변형 또는 가공할 수 없습니다.

- 귀하는, 이 저작물의 재이용이나 배포의 경우, 이 저작물에 적용된 이용허락조건을 명확하게 나타내어야 합니다.
- 저작권자로부터 별도의 허가를 받으면 이러한 조건들은 적용되지 않습니다.

저작권법에 따른 이용자의 권리는 위의 내용에 의하여 영향을 받지 않습니다.

이것은 [이용허락규약\(Legal Code\)](#)을 이해하기 쉽게 요약한 것입니다.

[Disclaimer](#)

Doctor of Philosophy

Development of the transition metal oxides with enhanced  
processability for interface engineering in polymer solar cells

The Graduate School  
of the University of Ulsan  
Department of Physics  
Hong Nhan Tran

Development of the transition metal oxides with enhanced  
processability for interface engineering in polymer solar cells

Supervisor: Prof. Shinuk Cho

A Dissertation

Submitted to

the Graduate School of the University of Ulsan

In partial Fulfillment of the Requirements

for the Degree of

Doctor of Philosophy

by

Hong Nhan Tran

Department of Physics

Ulsan, Korea

August 2021

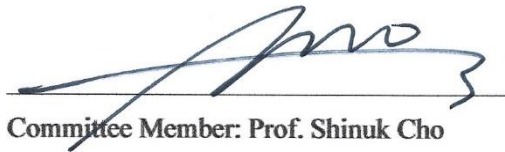
Development of the transition metal oxides with enhanced  
processability for interface engineering in polymer solar cells

This certifies that the dissertation/thesis of Hong Nhan Tran is approved.



---

Committee Chair: Prof. Sunghae Cho



---

Committee Member: Prof. Shinuk Cho



---

Committee Member: Prof. Young-Han Shin



---

Committee Member: Prof. Jung Hwa Seo



---

Committee Member: Dr. Dong Chan Lim

Department of Physics  
Ulsan, Korea  
August 2021

## Abstract

Polymer solar cells are the promising alternative candidate for silicon-based solar cells due to several advantages such as flexibility, lightweight, easy fabrication process, and low manufacturing cost. The power conversion efficiency of the non-fullerene solar cells had surpassed 18% due to the synthesis of the new p-type and n-type materials accompanied by the optimized morphology. Apart from the development of the novel high quality active materials, the researches on the new electrode interfacial layers are also necessitated to optimize the device performance and stability by controlling the charge transportation and charge separation at the interface between the polymer active layer and the electrode. Transition metal oxide is widely used as a carrier transport layer (also called as an electrode interfacial layer) in polymer solar cells. For example, ZnO, and SnO<sub>2</sub> are used for the electron transport layer while V<sub>2</sub>O<sub>5</sub>, WO<sub>3</sub>, MoO<sub>3</sub>, and NiO are used for the hole transport layer. Unfortunately, the transition metal oxide layer, which was prepared by sol-gel method, usually needs high annealing temperature (above 200 °C) to remove the organic ligand. The high temperature annealing process for the transition metal oxide layer will restrict the application of polymer solar cells in the flexible electronics industry because the flexible substrate cannot stand with a temperature above 100 °C. Therefore, it is essential to study on the annealing-free transition metal oxide layer that can applied in the polymer solar cells.

In this thesis, the novel annealing-free solution-process Molybdenum oxide (MoO<sub>x</sub>) and Nickel oxide (NiO) were successfully developed and applied in polymer solar cells as the hole transport layer. The MoO<sub>x</sub> and NiO layer exhibited excellent hole transporting properties without post-annealing process. In addition, the effect of the solvent additive on the morphology of the polymer-polymer solar cells was also investigated.

In chapter 1 of this thesis, we briefly introduced the fundamental of polymer solar cells and the various characterization methods for polymer solar cells.

In chapter 2, the effect of three different additives (1-chloronaphthalene, 1,8-diiodooctane, diphenylether) on the performance of polymer-polymer solar cells based on a BHJ blend consisting of PTB7-Th as a donor and (P(NDI2OD-T2)) as an acceptor was investigated. A direct comparison of the efficiency of the solar cells with and without additive indicated that the device using the additive exhibited slightly improved performance. However, the efficiency enhancement was not significant. The optimal ratio of additive differed depending on the properties of the additive. In addition, the performances of polymer-polymer solar cells were

not significantly dependent on the type of additive. Identifying the optimal fabrication condition was critical for achieving the highest performance. It is known that the general role of an additive in polymer solar cells based on a bulk-heterojunction (BHJ) active layer was to induce good phase separation between the donor and acceptor by morphology modification. However, grazing-incidence wide-angle X-ray scattering results showed that no significant morphology change in polymer-polymer active layer was caused by the additive. Rather, our modulated impedance spectroscopy study showed that the performance enhancement in polymer-polymer solar cells with additive was because of improved recombination properties rather than improvements in crystalline morphology.

In chapter 3, the novel annealing-free  $\text{MoO}_x$  hole transport layer was developed. Typically, a charge transport layer based on transition metal oxides prepared by an anhydrous sol-gel method requires high-temperature annealing in air to achieve the desired quality. Although annealing is not a difficult process in the laboratory, it is definitely not a simple process to apply in mass production such as roll-to-roll processes because of the inevitable long cooling step that follows. Therefore, the development of an annealing-free solution-processable metal oxide is essential for the large-scale commercialization. For this reason, we developed the novel room-temperature processable annealing-free ‘aqueous’  $\text{MoO}_x$  solution and applied it in bulk-heterojunction (BHJ) polymer solar cells based on non-fullerene system PBDB-T-2F:Y6 blend. By adjusting the concentration of water in the sol-gel route for the  $\text{MoO}_x$  precursor, we successfully developed an annealing-free  $\text{MoO}_x$  hole transport layer with excellent electrical properties. The PBDB-T-2F:Y6 non-fullerene solar cell with the general  $\text{MoO}_x$  layer prepared by the anhydrous sol-gel method showed a low efficiency of 7.7% without annealing. If this anhydrous  $\text{MoO}_x$  layer was annealed at 200 °C, the efficiency was recovered to 17.1% which was normal value typically observed in conventional structure PBDB-T-2F:Y6 solar cells. However, without any annealing process, the solar cell with aqueous  $\text{MoO}_x$  exhibited comparable performance of 17.0%. In addition, the solar cell with annealing-free aqueous  $\text{MoO}_x$  exhibited better performance and stability without high-temperature annealing compared to the solar cells with PEDOT:PSS.

In chapter 4, the novel annealing-free solution-processable NiO was developed and applied in both conventional and inverted non-fullerene polymer solar cells. In general, NiO offers intrinsic p-type behavior and high thermal and chemical stability, making it promising as a hole transport layer material in inverted organic solar cells. However, its use in this application has been rare because of a wettability problem caused by use of water as a base solvent and high-

temperature annealing requirements. To overcome the wettability problem, the typical deionized (DI) water solvent was replaced with a mixed solvent of DI water and isopropyl alcohol with a small amount of 2-butanol additive. This allowed a NiO nanoparticle suspension (s-NiO) to be deposited on a hydrophobic active layer surface. An inverted non-fullerene solar cell based on a blend of p-type polymer PTB7-Th and non-fullerene acceptor IEICO-4F exhibited the high efficiency of 11.23% with an s-NiO hole transport layer, comparable to the efficiency of an inverted solar cell with a MoO<sub>x</sub> hole transport layer deposited by thermal evaporation. Conventionally structured devices including our s-NiO layer showed efficiency comparable to that of a conventional device with a PEDOT:PSS hole transport layer.

Finally, the outcomes of this thesis were summarized in chapter 5.

# Table of Contents

Abstract .....	i
Table of Contents.....	iv
List of Figures .....	vi
List of Tables.....	xi
List of Abbreviations .....	xiii
<b>Chapter 1. Introduction .....</b>	<b>1</b>
<b>1.1 Polymer solar cells .....</b>	<b>1</b>
1.1.1 History of polymer solar cells .....	1
1.1.2 Principle of polymer solar cells .....	2
1.1.3 Structure of polymer solar cells .....	4
<b>1.2 Transition metal oxides .....</b>	<b>5</b>
1.2.1 History of Transition metal oxides .....	5
1.2.2 Molybdenum (VI) oxide .....	6
1.2.3 Nickel (II) oxide .....	8
<b>1.3 Characteristics of polymer solar cell .....</b>	<b>9</b>
1.3.1 Device characterization .....	9
1.3.2 Recombination losses determined by light intensity dependence method ...	11
1.3.3 Charge carrier mobility extraction by space-charge limited current (SCLC) method .....	12
<b>Chapter 2. The effect of various solvent additives on the power conversion efficiency of polymer-polymer solar cells.....</b>	<b>14</b>
<b>2.1 Research Background .....</b>	<b>14</b>
<b>2.2. Experimental.....</b>	<b>16</b>
2.2.1 Solution Preparation .....	16
2.2.2 Device Fabrication.....	16
2.2.3 Device Characteristics .....	17
<b>2.3 Results and Discussion .....</b>	<b>17</b>
<b>2.4 Conclusion .....</b>	<b>25</b>
<b>Chapter 3. 17% non-fullerene organic solar cells with annealing-free aqueous MoO<sub>x</sub>...</b>	<b>26</b>
<b>3.1 Research Background .....</b>	<b>26</b>
<b>3.2 Experimental.....</b>	<b>28</b>



3.2.1 Preparation of the MoO <sub>x</sub> Solution .....	28
3.2.2 Device Fabrication.....	29
3.2.3 Device Characteristics .....	30
<b>3.3 Results and Discussion .....</b>	<b>31</b>
<b>3.4 Conclusion .....</b>	<b>48</b>
<b>Chapter 4. Inverted polymer solar cells with annealing-free solution-processable NiO .</b>	<b>50</b>
<b>4.1 Research Background .....</b>	<b>50</b>
<b>4.2 Experimental.....</b>	<b>52</b>
4.2.1 Preparation of the NiO nanoparticle (NiO NP) solution .....	52
4.2.2 Device Fabrication.....	52
4.2.3 Device Characteristic.....	53
<b>4.3 Results and discussion .....</b>	<b>54</b>
<b>4.4 Conclusion .....</b>	<b>69</b>
<b>Chapter 5. Summary .....</b>	<b>70</b>
<b>References.....</b>	<b>72</b>
<b>Publication List .....</b>	<b>80</b>
<b>Korean Abstract .....</b>	<b>81</b>
<b>Acknowledgments.....</b>	<b>84</b>

## List of Figures

<b>Figure 1.1</b> The report of certificated efficiency of polymer solar cells from 2000 to present...	2
<b>Figure 1.2</b> A schematic for the basic working principle of a bulk heterojunction (BHJ) solar cell with (1) Exciton is created by incident photon, (2) Exciton migrates to D-A interface, (3) Exciton dissociates into free electron and free hole, (4) Electron and hole transport to electrode, and (5) Electron and hole are collected by electrode.....	3
<b>Figure 1.3</b> The architecture of a) conventional and b) inverted polymer solar cell.....	5
<b>Figure 1.4</b> (a) The electron configuration of molybdenum, (b) The common molybdenum sources for sol-gel processing method. ....	7
<b>Figure 1.5</b> (a) The electron configuration of nickel, (b) The common nickel sources for sol-gel and co-precipitate method. ....	9
<b>Figure 1.6</b> (a) The equivalent circuit of an ideal solar cell, (b) The I-V curve of the solar cell in the illumination and dark condition.....	10
<b>Figure 2.1</b> (a) Chemical structure of photoactive materials (donor: PTB7-Th, acceptor: P(NDI2OD-T2)) and schematic illustration of the device structure, (b) Energy level diagram of polymer-polymer solar cell base on PTB7-Th:P(NDI2OD-T2) blend, (c) Chemical structure of the solvent additives. ....	18
<b>Figure 2.2</b> J-V characteristics of PTB7-Th:P(NDI2OD-T2) solar cells fabricated with various ratios of (a) CN additive, (b) DIO additive, and (c) DPE additive.....	19
<b>Figure 2.3</b> (a) J-V characteristics and (b) EQE spectra of the best PTB7-Th:P(NDI2OD-T2) solar cell fabricated using optimized conditions of solvent additives. ....	20
<b>Figure 2.4</b> AFM height images (a,b,c,d) and phase images (e,f,g,h) of optimized PTB7-Th:P(NDI2OD-T2) blend films from chlorobenzene with: (a,e) no additive, (b,f) CN 0.1% vol, (c,g) DIO 0.5% vol, (d,h) DPE 0.5% vol.....	21
<b>Figure 2.5</b> 2D-GIWAXS image of the active layer under optimized conditions with (a) no additive, (b) CN 0.1% vol, (c) DIO 0.5% vol and d) DPE 0.5% vol. The line cut profiles of 2D-GIWAXS images in the (e) in-plane and (f) out-of-plane of PTB7-Th:P(NDI2OD-T2) blend films with the optimum concentration of various solvent additives.....	22

<b>Figure 2.6</b> 2D-GIWAXS image of the active layer under non-optimized conditions with (a) no additive, (b) CN 3% vol, (c) DIO 3% vol and d) DPE 3% vol. The line cut profile of 2D-GIWAXS image in the (e) in-plane and (f) out-of-plane of PTB7-Th:P(NDI2OD-T2) blend films with a non-optimum concentration of various solvent additives. ....	24
<b>Figure 2.7</b> Intensity modulated photo-voltage spectroscopy (IMVS) of a-PCS with (a) no additives, (b) CN 0.1% vol, (c) DIO 0.5% vol and (d) DPE 0.5% vol.....	24
<b>Figure 3.1</b> (a) Schematic diagrams of the PSCs with a conventional structure as well as the chemical structure of the materials and b) the energy level diagram of the PSC with a conventional structure.....	31
<b>Figure 3.2</b> (a) <i>J-V</i> characteristics of the PBDB-T-2F:Y6 solar cells, (b) <i>J-V</i> characteristics of the PBDB-T-2F:Y6 solar cells with an-MoO <sub>x</sub> annealed at various temperatures, (c) transmittance spectra of PEDOT:PSS, an-MoO <sub>x</sub> , and aq-MoO <sub>x</sub> , and (b) <i>J-V</i> characteristics of the fullerene-based solar cell based on PTB7-Th:PC <sub>71</sub> BM.....	33
<b>Figure 3.3</b> <i>J-V</i> characteristics of the conventional polymer solar cell based on (a) PBDTPD-HT:IDIC blend films with various hole transport layers, and (b) PTB7-Th:PC <sub>71</sub> BM blend films with an anhydrous MoO <sub>x</sub> film as a function of the annealing temperature. ....	33
<b>Figure 3.4</b> (a) EQE spectra of the solar cell based on PTB7-Th and PC <sub>71</sub> BM. (b) EQE spectra of the solar cell based on PBDTPD-HT and IDIC. (c) EQE spectra of the solar cell based on PBDB-T-2F and Y6.....	34
<b>Figure 3.5</b> <i>J-V</i> characteristics of the conventional polymer solar cells based on PTB7-Th:PC <sub>71</sub> BM blend films with aqueous MoO <sub>x</sub> with various H <sub>2</sub> O concentrations. ....	36
<b>Figure 3.6</b> (a) Charge extraction (CE) current transient under 1 sun illumination and V <sub>oc</sub> conditions, (b) calculated charge extraction density, and (c) Nyquist plot of the impedance spectroscopy measurements of the polymer solar cells with various MoO <sub>x</sub> HTLs under dark conditions. ....	37
<b>Figure 3.7</b> Fourier transform infra-red (FTIR) spectroscopy of MoO <sub>x</sub> HTLs: (a) fingerprint region, (b) function group region, and (c) CH <sub>2</sub> and CH <sub>3</sub> stretch mode vibration peaks of non-annealed an-MoO <sub>x</sub> films.....	38
<b>Figure 3.8</b> FTIR spectra obtained from anhydrous MoO <sub>x</sub> layers annealed at various temperatures.....	39

<b>Figure 3.9</b> FTIR spectra obtained from aqueous MoO <sub>x</sub> layers annealed at various temperatures. .....	39
<b>Figure 3.10</b> XPS spectra of (a) Mo 3d and (b) O 1s core level peaks obtained from the MoO <sub>x</sub> layers.....	41
<b>Figure 3.11</b> Schematic illustration of the expected chemical structures of the an-MoO <sub>x</sub> and aq-MoO <sub>x</sub> precursor solutions. ....	42
<b>Figure 3.12</b> UPS spectra of MoO <sub>x</sub> layers. ....	43
<b>Figure 3.13</b> Energy band diagrams of aq-MoO <sub>x</sub> and an-MoO <sub>x</sub> with and without annealing layers obtained from UPS measurements. ....	44
<b>Figure 3.14</b> Hole mobilities of OPVs based on PBDB-T-2F:Y6 blend films with various hole transport layers as PEDOT:PSS, anhydrous MoO <sub>x</sub> and aqueous MoO <sub>x</sub> . The hole-only devices configuration is ITO/HTL/PBDB-T-2F:Y6/evaporated MoO <sub>x</sub> /Ag. ....	44
<b>Figure 3.15</b> Atomic Force Microscope (AFM) images of (a) an-MoO <sub>x</sub> without annealing, (b) an-MoO <sub>x</sub> with annealing at 200 °C, and (c) aq-MoO <sub>x</sub> without annealing, and (d) XRD results. .....	45
<b>Figure 3.16</b> Atomic Force Microscope (AFM) topography images (top) and phase image (bottom) of PBDB-T-2F:Y6 active layer casted on (a) an-MoO <sub>x</sub> without annealing, (b) an-MoO <sub>x</sub> with annealing at 200 °C, (c) aq-MoO <sub>x</sub> without annealing, and (d) PEDOT:PSS. ....	45
<b>Figure 3.17</b> Changes of (a) $J_{sc}$ , (b) $V_{oc}$ , (c) $FF$ , and (d) PCE of non-fullerene solar cell based on PBDB-T-2F:Y6 during continuous operation in air without any encapsulation. ....	46
<b>Figure 3.18</b> Storage stability performed for PTB7-Th:PC <sub>71</sub> BM solar cells. ....	47
<b>Figure 3.19</b> (a) $J$ - $V$ characteristics of the inverted polymer solar cells based on PTB7-Th:PC <sub>71</sub> BM and the (b) $J$ - $V$ characteristics of polymer solar cell based on PBDTTPD-HT:IDIC. The hole transport layers were deposited on active layer in N <sub>2</sub> or air. To obtain better adsorption with an organic active layer, 2 mg/ml of Triton X-100 was added into the PEDOT:PSS and aq-MoO <sub>x</sub> solution. ....	48
<b>Figure 4.1</b> (a) Schematic diagrams and (d) energy level diagrams of the inverted polymer solar cell. (b) Chemical structures of donor polymer material, acceptor material, and NiO precursor. (c) FTIR spectrum of NiO nanoparticle powder. ....	55

<b>Figure 4.2</b> Schematic diagram of the NiO nanoparticle synthesis procedure.....	55
<b>Figure 4.3</b> (a) and (b) FTIR spectra of sol-gel NiO film as a function of annealing temperature ranged from 200 °C to 450 °C, (c) XRD spectra of NiO nanoparticle powder. ....	56
<b>Figure 4.4</b> (a) Digital photograph of PTB7-Th:IEICO-4F active layer. (b–d) Digital photographs of (b) e-MoO <sub>x</sub> , (c) s-NiO without 2-butanol, and (d) s-NiO with 2-butanol deposited on active layers. (e–f) Contact angle measurements on active layers of drops of NiO solutions (e) without and (f) with 2-butanol.....	57
<b>Figure 4.5</b> (a) AFM topography of a polymer active layer. (b–d) AFM topography of HTL layers deposited on the polymer active layer: (b) e-MoO <sub>x</sub> and (c) s-NiO from a solution without 2-butanol and (d) s-NiO from a solution with 2-butanol.....	57
<b>Figure 4.6</b> (a) Transmittance spectra of PEDOT:PSS, e-MoO <sub>x</sub> , and s-NiO deposited on ITO substrates. (b–c) Tauc plots of (b) e-MoO <sub>x</sub> and (c) s-NiO films. ....	58
<b>Figure 4.7</b> (a) <i>J–V</i> characteristics and (b) EQE spectra of inverted polymer solar cells based on PTB7-Th:IEICO-4F blend films with s-NiO and e-MoO <sub>x</sub> as hole transport layers. (c) <i>J–V</i> characteristics and (d) EQE spectra of conventional polymer solar cells based on PTB7-Th:IEICO-4F blend films with s-NiO and PEDOT:PSS as hole transport layers. ....	59
<b>Figure 4.8</b> <i>J–V</i> characteristics of the inverted polymer solar cell based on PTB7-Th:IEICO-4F blend films with different thicknesses of NiO layer.....	60
<b>Figure 4.9</b> (a) <i>J–V</i> characteristics and (b) EQE spectra of the inverted polymer solar cell based on PTB7-Th:PC <sub>71</sub> BM blend films with s-NiO and e-MoO <sub>x</sub> as hole transport layers. (c) <i>J–V</i> characteristics and (d) EQE spectra of the conventional polymer solar cell based on PTB7-Th:PC <sub>71</sub> BM blend films with s-NiO and PEDOT:PSS as hole transport layers. ....	61
<b>Figure 4.10</b> (a) Digital photograph of PTB7-Th:PC <sub>71</sub> BM active layer. Digital photograph of (b) e-MoO <sub>x</sub> , and (c) s-NiO w/ 2-butanol deposited on active layer. ....	62
<b>Figure 4.11</b> <i>J–V</i> characteristics of the inverted polymer solar cell based on PTB7-Th:IEICO-4F blend films with ‘CLEVIOS™ HTL Solar’ hole transport layers.....	62
<b>Figure 4.12</b> (a–b) Light intensity dependence of (a) <i>J</i> <sub>sc</sub> and (b) <i>V</i> <sub>oc</sub> . (c) Hole mobilities of hole-only devices based on PTB7-Th:IEICO-4F blend films with e-MoO <sub>x</sub> and s-NiO hole transport layers and with no hole transport layer. (d) Nyquist plot of IS measurements collected under dark conditions of inverted polymer solar cells with various HTLs. ....	64

**Figure 4.13** (a) I–V curve of s-NiO film based on the structure of ITO/s-NiO/Au. (b) Absorption spectra of p-type polymer PTB7-Th and non-fullerene acceptor IEICO-4F, (c) Photoluminescence of Glass/PTB7-Th:IEICO-4F and Glass/PTB7-Th:IEICO-4F/s-NiO. .... 64

**Figure 4.15** Energy band diagrams of e-MoO<sub>x</sub> and s-NiO films based upon UPS measurements. Band gaps ( $E_g$ ) of e-MoO<sub>x</sub> and s-NiO films were extracted from transmittance spectra. .... 67

**Figure 4.16** (a–c) Surface potential images of (a) ITO, (b) ITO/PEDOT:PSS, and (c) ITO/s-NiO. (d) Summary of surface potential values of PEDOT:PSS and s-NiO deposited on ITO. 67

**Figure 4.17** Stability testing: changes in normalized (a)  $J_{SC}$ , (b)  $V_{OC}$ , (c) FF, and (d) PCE during continuous monitoring (interval: 5 min) of devices subjected to continuous illumination for 25 h. .... 68

## List of Tables

<b>Table 1.1</b> The summarized work function of TMO material which were used in OPV.....	6
<b>Table 2.1</b> Summarized photovoltaic performance characteristics of a-PSC with various ratio of CN additive.....	19
<b>Table 2.2</b> Summarized photovoltaic performance characteristics of a-PSC with various ratio of DIO additive. ....	19
<b>Table 2.3</b> Summarized photovoltaic performance characteristics of a-PSC with various ratio of DPE additive.....	20
<b>Table 2.4</b> Summarized photovoltaic performance characteristics of the best a-PSC under the optimized conditions for solvent additives.....	20
<b>Table 3.1</b> Summarized photovoltaic parameters of the conventional polymer solar cell based on PTB7-Th:PC <sub>71</sub> BM and non-fullerene solar cell based on PBDB-T-2F:Y6 or PBDTTPD-HT:IDIC. ....	34
<b>Table 3.2</b> Summarized photovoltaic parameters of the conventional polymer solar cell based on .....	35
<b>Table 3.3</b> Photovoltaic performance of the conventional polymer solar cell based on PTB7-Th:PC <sub>71</sub> BM blend films with aqueous MoO <sub>x</sub> with various H <sub>2</sub> O concentrations. ....	36
<b>Table 3.4</b> The Mo <sup>6+</sup> /Mo <sup>5+</sup> , Oxygen-HBE/Oxygen-LBE, and O atom/Mo atom ratios calculated from the XPS data. ....	42
<b>Table 3.5</b> Hole mobilities of OPVs based on PBDB-T-2F:Y6 blend films with various hole transport layers as PEDOT:PSS, anhydrous MoO <sub>x</sub> and aqueous MoO <sub>x</sub> . ....	44
<b>Table 4.1</b> Photovoltaic performance parameters of inverted and conventionally structured polymer solar cells based on PTB7-Th:IEICO-4F blend films with s-NiO layers.....	58
<b>Table 4.2</b> Photovoltaic performance of the inverted polymer solar cell based on PTB7-Th:IEICO-4F blend films with different thicknesses of NiO layer.....	60
<b>Table 4.3</b> Photovoltaic performance parameters of inverted and conventionally structured polymer solar cells based on PTB7-Th:PC <sub>71</sub> BM blend films with s-NiO layers.....	62
<b>Table 4.4</b> Photovoltaic performance of the inverted polymer solar cell based on PTB7-Th:IEICO-4F blend films with ‘CLEVIOS™ HTL Solar’ hole transport layers.....	63

**Table 4.5** Summary of the parameters obtained from UPS data of various HTL layers: PEDOT:PSS, e-MoO<sub>x</sub> and s-NiO. The notations E<sub>g</sub>, WF, IP, Φ<sub>e</sub>, and Φ<sub>h</sub> respectively denote the optical band gap, work function, ion potential, electron injection barrier, and hole injection barrier.....66



## List of Abbreviations

Abbreviations	Descriptions
AFM	Atomic force microscopy
an-MoO <sub>x</sub>	Anhydrous MoO <sub>x</sub>
a-PSCs	All-polymer solar cell
aq-MoO <sub>x</sub>	Aqueous MoO <sub>x</sub>
BHJ	Bulk heterojunction
CB	Chlorobenzene
CF	Chloroform
CN	1-chloronaphthalene
DIO	1,8-diiodooctane
DPE	Diphenylether
e-MoO <sub>x</sub>	Evaporation MoO <sub>x</sub>
EQE	External quantum efficiency
ETL	Electron transport layer
FF	Fill factor
FTIR	Fourier transform infrared spectroscopy
FTO	Fluorine-doped tin oxide
GIWAXS	Grazing-incidence wide-angle X-ray scattering
HOMO	High occupied molecular orbital
HR-XRD	High-resolution X-ray diffraction spectroscopy
HTL	Hole transport layer
IMVS	Intensity modulated photo-voltage spectroscopy
IPA	Isopropanol alcohol
I <sub>sc</sub>	Short-circuit current
ITO	Indium tin oxide
J <sub>sc</sub>	Short-circuit current density
KPFM	Kelvin probe force microscopy
LUMO	Low occupied molecular orbital
MoO <sub>3</sub> ; MoO <sub>2</sub> ; MoO <sub>x</sub>	Molybdenum oxide
M-PEDOT	Modified PEDOT:PSS
NiO; NiO <sub>x</sub>	Nickel oxide

OLED	Organic light-emitting diode
OPV	Organic photovoltaic
PCE	Power conversion efficiency
PEDOT:PSS	Poly(3,4-ethylenedioxythiophene)poly(styrenesulfonate)
PSCs	Polymer solar cells
RuO <sub>x</sub>	Ruthenium oxide
SCLC	Space-charge limited current
s-NiO	Solution-processable NiO
TEM	Transmission electron microscopy
TMO	Transition metal oxides
V <sub>oc</sub>	Open-circuit voltage
VO <sub>x</sub> ; V <sub>2</sub> O <sub>5</sub>	Vanadium oxide
WF	Work function
WO <sub>3</sub>	Tungsten oxide
ZnO	Zinc oxide

---

# Chapter 1. Introduction

## 1.1 Polymer solar cells

### 1.1.1 History of polymer solar cells

The demand for renewable energy keeps increasing these days due to the depletion of fossil fuels and their harmful impact on the environment. Among various renewable energy sources, solar energy is considered as a key to clean energy for sustainable future due to its large abundance. The solar cells, which are the devices that converted solar energy into electricity, are usually divided into three generations up to recent years. The first generation is the solar cells based on single or multi-crystalline silicon, which are relatively expensive to fabricate thus exhibited high cost per watt of electricity. The second generation contains a category of solar cells based on amorphous silicon, which is much cheaper to produce, thereby lowering the cost per watt compared with the first-generation cells. The term third generation is used for various types of silicon-free solar cells such as organic-based solar cells (small molecules or semiconducting polymer), nanocrystal-based solar cells, dye-sensitized solar cells, etc. Among them, the polymer-based solar cells have received the most attention in recent years due to several advantages like flexibility, lightweight devices, easy fabrication process with solution processing method, and low manufacturing cost. It is believed that the polymer solar cell is a promising alternative candidate for silicon-based solar cells.

In 1977, the electrical conductivity of polymer was discovered by Alan Heeger, Hideki Shirakawa, and Alan MacDiarmid, who were jointly awarded the Nobel Prize in Chemistry in 2000. From that milestone, a large number of studies on polymer solar cells have been developed and studied. **Figure 1.1** shows the report of certificated efficiency of polymer solar cells from 2000 to present. In an early stage, the solar cell efficiency of ~ 3% was reported with the polymer active layer based on a blend of p-type polymer P3HT and n-type fullerene acceptor PCBM. Since then, the efficiency was increased rapidly up to 11% through the synthesis of new low bandgap p-type polymers including PTB7-Th and PffBT4T-2OD. Furthermore, between 2014 and 2018, the efficiency was increased a bit slowly due to the inevitable problems of PCBM and its derivatives. Fortunately, the recent discovery of the new n-type non-fullerene acceptor was a game-changer in the research of polymer solar cells. The efficiency of non-fullerene polymer solar cell was boosted up to 18% due to the optimization of morphology and energy level configuration.<sup>[1]</sup> Apart from the development of the novel high quality active materials, the researches on the new electrode interfacial layers are also necessitated to optimize

the device performance and stability by controlling the charge transportation and charge separation at the interface between the polymer active layer and the electrode. The fully optimized charge transport will open up a bright future for polymer solar cells.

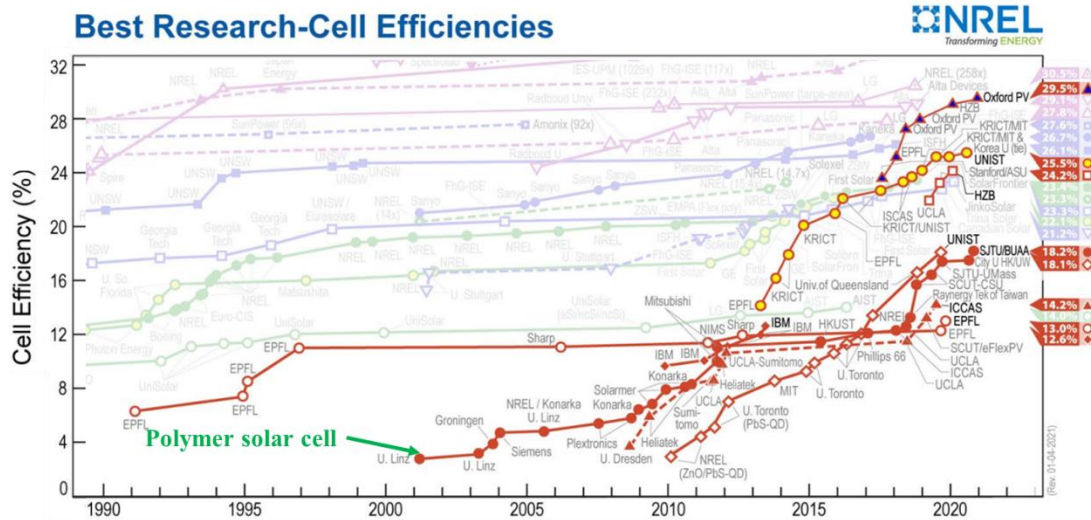


**Figure 1.1** The report of certificated efficiency of polymer solar cells from 2000 to present.

### 1.1.2 Principle of polymer solar cells

Before describing the principle of polymer solar cells, some definitions related to organic semiconductor are needed to define.

- First, the energy band diagram of organic semiconductor was described. From the literature, the organic semiconductor band structure is divided into High Occupied Molecular Orbital (HOMO) and Low Occupied Molecular Orbital (LUMO). The energy gap between HOMO and LUMO is defined as the bandgap of the organic semiconductor.
- Second, the formation of exciton in the organic semiconductor was described. As a result of the internal photoelectric effect, when the incident light (i.e. photon) with the energy higher than the organic semiconductor bandgap was absorbed by the organic semiconductor, an electron from the HOMO will be excited into the LUMO that leaving a hole in the HOMO, which is defined as electron-hole pair or exciton. The excited electron and excited hole were still suffering an attractive force that given by Coulomb's law as  $F = \left(\frac{1}{4\pi\epsilon_r\epsilon_0}\right)\left(\frac{q_1q_2}{r^2}\right)$  with  $q$ ,  $\epsilon_0$ ,  $\epsilon_r$ , and  $r$  are the elementary charges, absolute permittivity, relative permittivity, and the distance between excited electron and excited hole, respectively. Since the organic semiconductor has a low value of  $\epsilon_r$ , the exciton is experienced a relatively high attractive force so that the thermal energy at room

temperature is not sufficient to dissociate it into free electron and free hole. Therefore, the exciton easily relaxes its energy into the ground state.

A schematic for the basic operation principle of a bulk heterojunction (BHJ) solar cell was shown in **Figure 1.2**. For simplicity, a basic design of the polymer solar cell is the sandwich structure that consists of a polymer active layer between the transparent conducting electrode and the metal electrode. The polymer active layer is a binary blend of p-type polymer and n-type acceptor, which act as the donor and the acceptor, respectively. When the incident light was absorbed by the polymer active layer, the excitons were generated inside the donor phase. Then, these excitons will diffuse to the donor-acceptor interface and some portion of them will recombine (radiative or non-radiative) before reaching that interface. To maximize the excitons collection probability at the donor-acceptor interface, the phase domain of the polymer active layer should be equivalent to the average exciton diffusion length, approximately 5 - 20 nm. When the excitons reach the donor-acceptor interface, they are separated into the free electrons and free holes due to the energy difference between  $LUMO_{Donor}$  and  $LUMO_{Acceptor}$ . The free electrons will transport from the donor phase into the acceptor phase while the free holes remain in the donor phase due to the blocking barrier created by  $HOMO_{Donor}$  and  $HOMO_{Acceptor}$ . Finally, the opposite charges must travel inside the respective phases and reach the collecting electrodes. To eliminate the charges recombination at the electrodes, the ohmic contact should be formed at the interface of electrodes and polymer active layer.

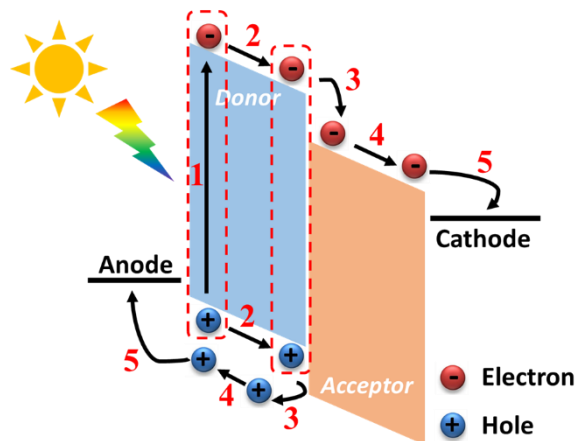


**Figure 1.2** A schematic for the basic working principle of a bulk heterojunction (BHJ) solar cell with (1) Exciton is created by incident photon, (2) Exciton migrates to D-A interface, (3) Exciton dissociates into free electron and free hole, (4) Electron and hole transport to electrode, and (5) Electron and hole are collected by electrode.

### 1.1.3 Structure of polymer solar cells

The simplest structure of polymer solar cell is shown in **Figure 1.2**. In fact, the interfacial layer, or carrier transport layer, is placed between the electrode and polymer active layer to resolve the energy level mismatch between the cathode and  $\text{LUMO}_{\text{Acceptor}}$  (or the anode and  $\text{HOMO}_{\text{Donor}}$ ). **Figure 1.3** shows the typical architecture of polymer solar cells that can be categorized as the conventional architecture and inverted architecture depended on the flow of holes (or electrons) toward the transparent conducting electrode, respectively. In the conventional polymer solar cell, the transparent conductive substrate, such as indium tin oxide (ITO) or fluorine-doped tin oxide (FTO), acts as the anode electrode. Then, the hole transport layer, typically a conducting polymer poly(3,4-ethylenedioxythiophene)-poly(styrenesulfonate) (PEDOT:PSS) or solution-processable transition metal oxide such as molybdenum oxide ( $\text{MoO}_3$ ), nickel oxide (NiO), tungsten oxide ( $\text{WO}_3$ ), etc. was coated on the ITO substrate by spin coating technique. Next, the polymer active layer and electron transport layer (ETL), for example, zinc oxide (ZnO), were consequently spun coat on the hole transport layer (HTL). Finally, a low work function metal, for example, aluminum (Al) was thermally evaporated on the electron transport layer to finalize the device. Although the efficiency of the conventional polymer solar cell is good and reproducible, it also shows several disadvantages. The conventional architecture has low device stability due to the usage of the low work function metal for the top electrode, which will be easily oxidized. Furthermore, the acidity of PEDOT:PSS layer may corrode the ITO substrate that leading to device instability. Moreover, the polymer active layer, particularly the blend system based on fullerene, exhibited the vertical phase separation during the film formation due to the difference of the surface energy between the p-type polymer and the n-type acceptor. The acceptor phase is mainly concentrated at the bottom of the polymer active layer whereas the donor phase is concentrated at the top of the polymer active layer. The wrong distribution of donor and acceptor phase is unfavorable for the charge transportation in the conventional structure, where the electrons should flow to the top electrode and the holes should flow to the bottom transparent electrode. In consequence, the conventional structure polymer solar cell exhibits instability performance and unfavored charge transportation.

The disadvantage of conventional structure can be overcome with the inverted structure polymer solar cell. In the inverted structure, the electron transport layer, commonly solution-processable ZnO, was deposited on the ITO substrate. Next, the polymer active layer was spun coat on the electron transport layer. Finally, the transition metal oxide, commonly  $\text{MoO}_x$ , and

the high work function silver (Ag) were consequently deposited on the polymer active layer by thermal evaporation. Since the donor phase was distributed near the interface of polymer active layer and hole transport layer and vice versa, the unfavorable transportation problem was solved. Furthermore, the stability issue was also solved since the inverted structure used a high work function electrode (Ag), which was less oxidized compared with Al. Finally, the inverted structure can apply to the all-solution-processing polymer solar cell due to the recent development of the low-temperature (below 80 °C) solution-processable transition metal oxide and solution-processable silver. By using the roll-to-roll process, the large-area polymer solar cell can be fabricated along with the reduction of production cost.

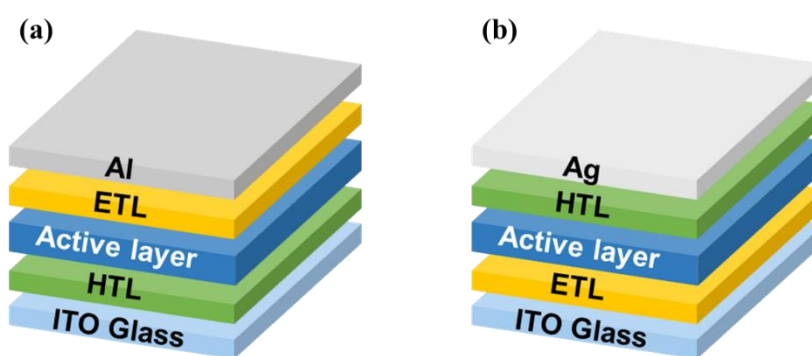


**Figure 1.3** The architecture of a) conventional and b) inverted polymer solar cell.

## 1.2 Transition metal oxides

### 1.2.1 History of Transition metal oxides

Generally, transition metals are defined as the elements with partially filled d orbitals, which were contained up to nine electrons in the outer shell. Most transition metals have multiple oxidation states because transition metals have d-orbitals which are exhibited various oxidation states. In the form of oxide, the transition metal oxides (TMO) exhibit unique electrical properties and optical properties. For this reason, TMOs have been extensively studied over the last decades. The first application of TMO, such as molybdenum oxide ( $\text{MoO}_x$ ), vanadium oxide ( $\text{VO}_x$ ), and ruthenium oxide ( $\text{RuO}_x$ ), were served as the hole-injection-layer in an organic light-emitting diode (OLED) in 1996. Since then, the numerous studies about TMO were rapidly increased, which were mostly focused on the applications in organic electronic devices, for examples, carrier-transport layer in the organic photovoltaic (OPV), carrier-injection layer in OLED, and interconnection layer in tandem OLED and OPV, etc. Most TMO films exhibited high bandgap (above 3 eV), which was beneficial to apply as an interfacial layer in both OPV and OLED. Furthermore, TMO films also showed a favorable work function for carrier

transportation, i.e. high work function for serving as the hole transport layer and vice versa in OPV. For these reasons, TMO films are the best candidate for the carrier transport layer in OPV. **Table 1.1** shows the summarized work function of TMO material which were used in OPV. In this thesis, we focused on the application of TMO, such as MoO<sub>x</sub> and nickel oxide (NiO), as the HTL in the OPV devices.

**Table 1.1** The summarized work function of TMO material which were used in OPV.

Chemical name	Work function
Solution-process Molybdenum oxide	5.1 eV ~ 5.2 eV
Evaporation Molybdenum oxide	5.9 eV ~ 6.3 eV
Nickel oxide	5.1 eV ~ 5.2 eV
Tungsten oxide	5.3 eV
Vanadium oxide	5.2 eV
Copper oxide	5.2 eV ~ 5.3 eV
Titanium oxide	4.7 eV
Zinc oxide	4.7 eV

### 1.2.2 Molybdenum (VI) oxide

Molybdenum (Mo) is a transition metal with an atomic number of 42 and has 6 valance electrons. The electron configuration can be described as [Kr] 4d<sup>5</sup>5s<sup>1</sup>. Molybdenum has two oxide formulas as molybdenum (IV) dioxide (MoO<sub>2</sub>) and molybdenum (VI) trioxide (MoO<sub>3</sub>), and MoO<sub>2</sub> has higher conductivity than MoO<sub>3</sub>. Unfortunately, MoO<sub>2</sub> exhibits a low bandgap of 1.83 eV compared with the high bandgap of MoO<sub>3</sub> of 3.2 eV.<sup>[2]</sup> The high absorption loss in the visible wavelength of MoO<sub>2</sub> will restrict its usage in optoelectronic devices where high transparency is required. Therefore, MoO<sub>3</sub> is chosen as the HTL in the inverted polymer solar cells due to its high transparency and low melting point. In the inverted polymer solar cells, the careful control of evaporation temperature is required since the high evaporation temperature may hinder the electrical properties of the polymer active layer. MoO<sub>3</sub> exhibits a low melting point of 795 °C compared with that of other TMO as NiO of 1955 °C and Tungsten (VI) oxide (WO<sub>3</sub>) of 1,473 °C. For this reason, MoO<sub>3</sub> is commonly used as HTL in the inverted polymer.

The deposition of MoO<sub>3</sub> by thermal evaporation method has the disadvantage that it cannot be applied in large-scale production due to the complicated setup and high operation cost. The solution-processable MoO<sub>3</sub> is found as the best alternative to resolve this problem. Liu et al.



reported about the aqueous  $\text{MoO}_3$  solution prepared by the hydration method with the precursor ammonium molybdate  $((\text{NH}_4)_6\text{Mo}_7\text{O}_{24})$ .<sup>[3]</sup> However, the large-scale  $\text{MoO}_3$  cluster remained in the film that leading to the reduction in PCE due to the non-uniform  $\text{MoO}_3$  film. Using the same precursor ammonium molybdate, Murase et al. develop the layered structure  $\text{MoO}_3$  with the post-deposition annealing temperature of 100 °C. Besides ammonium molybdate, molybdenyl acetylacetonate ( $\text{MoO}_2(\text{acac})_2$ ) was alternatively used as molybdenum source for the sol-gel processing. Zilberberg et al. reported on the sol-gel process  $\text{MoO}_3$  film prepared by spin coating the  $\text{MoO}_2(\text{acac})_2$ /isopropanol solution on ITO and kept in air for 1 hour for hydrolysis. Then the  $\text{MoO}_3$  was treated with the annealing temperature of 150 °C in  $\text{N}_2$  to archive the high work function of 5.3 eV.<sup>[4]</sup> Later then, the Heeger group reported on sol-gel  $\text{MoO}_3$  solution prepared by diluted  $\text{MoO}_2(\text{acac})_2$  in both anhydrous and aqueous methanol along with the post-annealing temperature of 100 °C.<sup>[5]</sup> All of these above sol-gel solutions are only applicable to the conventionally structured polymer solar cell with a rigid substrate. The usage of the high post-annealing temperature (above 100 °C) prevents their application in the inverted polymer solar cell since most polymer active material cannot stand with high annealing temperature. On the other hand, the high annealing temperature also restricts the application of TMO on the flexible substrate, where heat sensitivity is a big issue. Therefore, there is a need for a study on the annealing-free transition metal oxide layer applied in the polymer solar cell. **Figure 1.4** shows the electron configuration of molybdenum and the common molybdenum sources for the sol-gel method.

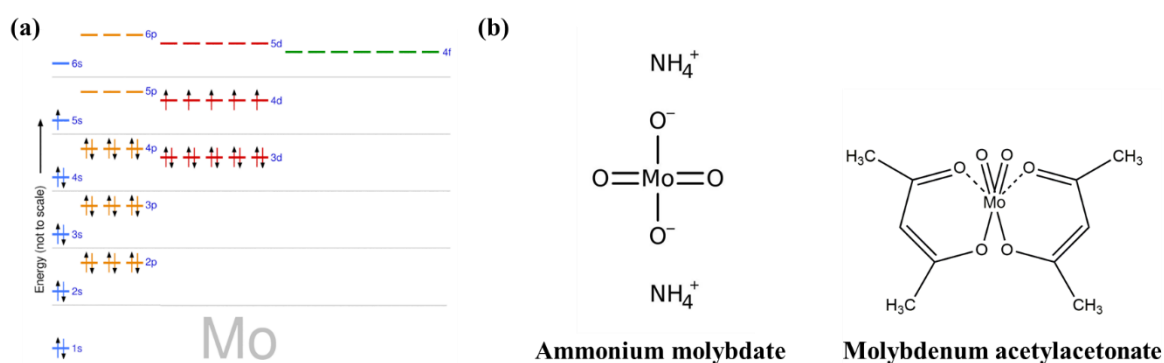


**Figure 1.4** (a) The electron configuration of molybdenum, (b) The common molybdenum sources for sol-gel processing method.

### 1.2.3 Nickel (II) oxide

Nickel (Ni) is a transition metal with an atomic number of 28 and has 2 valence electrons. The electron configuration can be described as  $[\text{Ar}] 3d^8 4s^2$ . nickel (II) oxide formula is NiO, which is often non-stoichiometric. The stoichiometric NiO powder shows a green color, whereas the non-stoichiometric NiO<sub>x</sub> powder shows black color. Pure stoichiometric NiO is a perfect insulator with an approximate conductivity of  $10^{-13} \text{ S cm}^{-1}$  while the non-stoichiometric NiO<sub>x</sub> has a conductivity of  $10^{-7} \text{ S cm}^{-1}$ .<sup>[6]</sup> Furthermore, non-stoichiometric NiO<sub>x</sub> has nickel deficiency (or excess oxygen) accommodated by nickel vacancies. One Ni<sup>2+</sup> vacancy produces two Ni<sup>3+</sup> ions which are contributed as dopants for p-type doping in NiO<sub>x</sub> film.<sup>[7,8]</sup> NiO<sub>x</sub> is commonly used as HTL in the polymer solar cell, mostly in the conventionally structured solar cell. As stated in section 1.2.2, NiO has a high evaporation temperature which will restrict its application in the inverted structure polymer solar cell.

There are various methods to prepare the solution process NiO such as solvothermal, sol-gel, combustion, etc. Among them, sol-gel is the most widely used method due to its easy preparation. Steirer et. al. reported about NiO film deposited on ITO by spin coating the Ni precursor ink followed with the post-annealing temperature as 300 °C for one hour.<sup>[9]</sup> Later then, Mustafa et. al. developed a thin NiO film by spin coating the nickel acetylacetonate (Ni(acac)) diluted in toluene with the post-annealing temperature of 400 °C.<sup>[10]</sup> Manders et. al. reported about the NiO solution by diluted nickel acetate tetrahydrate (Ni(CH<sub>3</sub>COO)<sub>2</sub>·4H<sub>2</sub>O) in ethanol with monoethanolamine (NH<sub>2</sub>CH<sub>2</sub>CH<sub>2</sub>OH) as a stabilizer ligand.<sup>[11]</sup> The NiO film was heated at 275 °C for one hour to obtain a high-quality film. The above studies indicated that NiO film fabricated with the sol-gel NiO solution needs to anneal at high temperature to remove the organic ligand and obtain the original form of NiO. Therefore, there were many efforts to reduce the post-annealing temperature of NiO film. Recently, the NiO nanoparticles synthesized by the co-precipitate method with a precursor of nickel nitrate hexahydrate (Ni(NO<sub>3</sub>)<sub>2</sub>·6H<sub>2</sub>O) exhibited high work function and good hole transportation properties at low temperature (below 100 °C).<sup>[12]</sup> The NiO solution was prepared by dispensing NiO nanoparticles in deionized (DI) water. Then, it was spun coating on ITO substrate without applying post-annealing temperature. For this result, the NiO nanoparticle dispersions are widely used in conventional polymer solar cells to alternate the PEDOT:PSS layer. Even the low-temperature solution-processable NiO was developed, this solution was not applicable for inverted solar cells since its solvent was DI water which was hard to spin coating on the hydrophobic surface as a polymer active layer. Therefore, there is a need for a new method to deposit the NiO nanoparticle dispersion on the polymer

active layer in the inverted solar cell. **Figure 1.5** shows the electron configuration of nickel and the common nickel sources for the sol-gel and co-precipitate method.

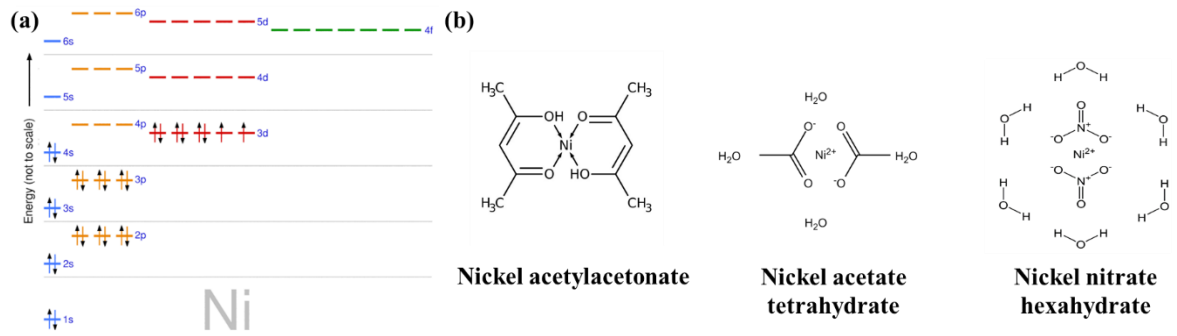


**Figure 1.5** (a) The electron configuration of nickel, (b) The common nickel sources for sol-gel and co-precipitate method.

### 1.3 Characteristics of polymer solar cell

#### 1.3.1 Device characterization

On the laboratory scale, the solar cell characteristic can be determined by measuring the I-V curve of the solar cell under the artificial sunlight source. The sunlight flux density ( $S_d$ ) is calibrated as  $100 \text{ mW.cm}^{-2}$  or 1 sun. In working conditions, the solar cell is connected to a load resistance ( $R_L$ ) followed the Ohm's law.

$$R_L = \frac{U}{I} \quad (1.1)$$

**Figure 1.6a** shows the equivalent circuit of an ideal solar cell that consisted of the photocurrent generator ( $I_{ph}$ ) in parallel with a diode and they are connected to the load resistance  $R_L$ . A diode current ( $I_D$ ) and the ideal solar cell current ( $I$ ) are described by the followed equation, respectively.

$$I_D = I_0 \left( \exp \left( \frac{q.U}{k_B.T} \right) - 1 \right) \quad (1.2)$$

$$I = I_0 \left( \exp \left( \frac{q.U}{k_B.T} \right) - 1 \right) - I_{ph} \quad (1.3)$$

$I_0$  is the diode saturation current or the leakage current, which is a unique characteristic of the solar cell. In dark condition, the generated photocurrent ( $I_{ph}$ ) is equal to zero leading to the dark-current ( $I_{dark}$ ) of the solar cell is equal to  $I_D$ . For this result, the I-V curve of the solar cell in dark condition shows the diode characteristic. Under illumination condition, the I-V curve of the solar cell exhibits two important conditions such as short-circuit condition and open-circuit condition. In the short-circuit condition ( $R_L = 0$  and  $V = 0$ ), the short-circuit current ( $I_{SC}$ ) in

equation (1.3) can be written as  $I_{SC} = -I_{ph}$  with  $I_{ph} \gg I_0$ . In the open-circuit condition ( $R_L = \infty$  and  $I = 0$ ), the open-circuit voltage in equation 1.3 can be written as

$$I_0 \left( \exp\left(\frac{q \cdot V_{OC}}{k_B T}\right) - 1 \right) = I_{SC} \quad (1.4)$$

$$V_{OC} \approx \frac{k_B T}{q} \ln\left(\frac{I_{SC}}{I_0}\right) \quad (1.5)$$

As seen from equation 1.5,  $I_0$  plays an important role in the maximization of  $V_{OC}$ . The leakage current  $I_0$  can be minimized with the optimization of the charge transportation at the interface of the active layer and electrode. The optimization of  $J_{SC}$  and  $V_{OC}$  is very crucial for maximizing the efficiency of a solar cell. **Figure 1.6b** shows the I-V curve of the solar cell in the illumination and dark condition. From the illumination I-V curve, there is only one point that the product of current and voltage is maximum, which are denoted as  $I_{mp}$  and  $V_{mp}$ , respectively. That point is called the maximum point and the maximum power of the solar cell can be described as

$$P_{max} = I_{mp} \cdot V_{mp} \quad (1.6)$$

The  $P_{max}$  is displayed as the grey rectangle in **Figure 1.6b** and the ratio of  $P_{max}$  to the product of  $J_{SC}$  and  $V_{OC}$  is defined as the fill factor (FF).

$$FF = \frac{I_{mp} \cdot V_{mp}}{I_{SC} \cdot V_{OC}} \quad (1.7)$$

The solar cell efficiency ( $\eta$ ) is defined as the ratio of solar cell maximum power and the power of sunlight ( $P_{in} = A \cdot S_d$ ) illuminated to the solar cell with  $A$  is the area of solar cell and  $S_d$  is the solar flux density, particularly  $100 \text{ mW} \cdot \text{cm}^2$ .

$$\eta = \frac{P_{max}}{P_{in}} = \frac{I_{SC} \cdot V_{OC} \cdot FF}{A \cdot S_d} \quad (1.8)$$

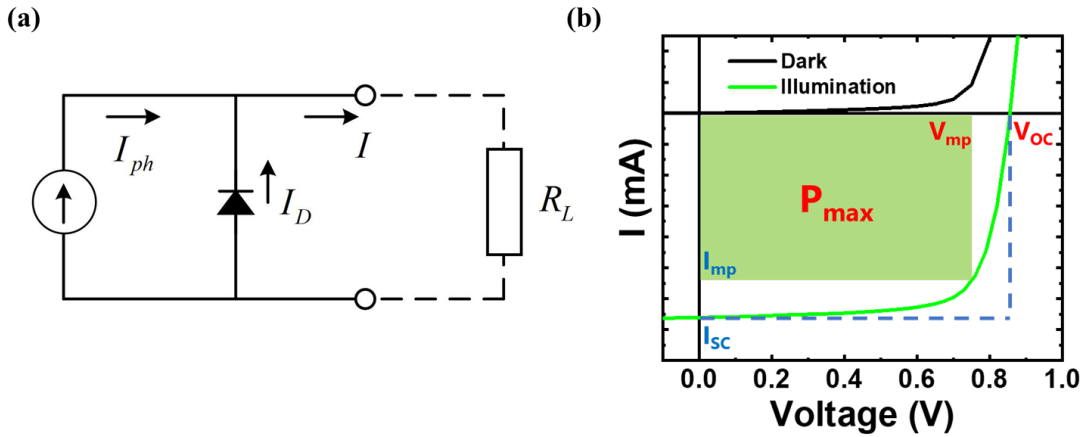


**Figure 1.6** (a) The equivalent circuit of an ideal solar cell, (b) The I-V curve of the solar cell in the illumination and dark condition.

### 1.3.2 Recombination losses determined by light intensity dependence method

Recombination losses and optical losses are the two factors that hindered the performance of the solar cell. There are two types of recombination; germinate recombination and non-germinate recombination.<sup>[13]</sup> In an ideal case, one incident photon absorbed by the polymer active layer will create one electron-hole pair. The electron-hole pair will migrate to the donor-acceptor interface, then it was separated into a free hole and a free electron. However, there is a probability that the electron-hole pair recombines before reaching the donor-acceptor interface due to its short lifetime. Furthermore, there is also a probability that the separated charges will recombine right after the electron-hole pair was separated. All the above recombination events are originated from one photon and these recombinations are defined as germinate recombination. On the other hand, non-germinated recombination is defined as the recombination of the free electron and free hole which originated from a different photon. The non-germinate recombination is divided into three types depending on their mechanism such as monomolecular, bimolecular, and trimolecular. In monomolecular recombination, the trap states, which were originated from the internal defect states of the polymer active layer or interfacial defect states between polymer active layer and carrier transport layer, were created within the energy bandgap. The free charge carrier will recombine with the opposite charge carrier that was trapped at the trap states. For this reason, this recombination is denoted as monomolecular recombination since there is only one charge carrier involved in the recombination process. The bimolecular recombination occurs when a free hole and a free electron recombine with each other. The bimolecular recombination can be radiative or non-radiative. The trimolecular recombination, or Auger recombination, occurs when a free hole recombines with a free electron and the released energy will excite an electron from the HOMO to the LUMO. Monomolecular recombination and bimolecular recombination are mainly dominant in polymer solar cells.

Non-germinate recombination in the polymer solar cell can be determined by measuring the current density-voltage (J-V) characteristic of the solar cell under different incident light intensity. From the literature, the short-circuit current density ( $J_{SC}$ ) exhibits power-law dependence upon light intensity ( $I$ ), which can be expressed as  $J_{SC} \propto I^\alpha$ . From the linear fitting of  $\ln(J_{SC})$ - $\ln(I)$  plot, the  $\alpha$  value can be extracted. Note that, in the ideal case of short-circuit condition, all the generated carriers are completely collected by the electrodes without bimolecular recombination. In other words, the  $\alpha$  value is equal to one and the  $J_{SC}$  shows

perfectly linear dependence with the light intensity. The more deviation from  $\alpha = 1$  indicates that bimolecular recombination is more dominant in the short-circuit condition.

Similarly,  $V_{OC}$  also exhibited a linear relationship with the logarithm of light intensity ( $\ln I$ ), which can be expressed as  $V_{OC} \propto n(kT/q)\ln(I)$ , where  $k$  is the Boltzmann constant,  $T$  is the absolute temperature,  $q$  is the elementary charge, and the ideality factor  $n$  is determined from the linear fitting of  $V_{OC}$ - $\ln(I)$  plot. The ideality factor  $n$  value of 1 indicates bimolecular recombination, whereas the  $n$  value of 2 indicates pure monomolecular recombination.<sup>[14]</sup> The more deviation from  $n = 1$  indicates that monomolecular recombination is more dominant in the open-circuit condition. The dominance of monomolecular recombination indicates that the defect states are likely occurred in the polymer solar cell. In summary, the light intensity dependence method is a powerful tool to determine the monomolecular recombination and the bimolecular recombination of the polymer solar cell.

### 1.3.3 Charge carrier mobility extraction by space-charge limited current (SCLC)

#### method

Space-charge is the concept that unipolar charges are continuously distributed over a region of space. Due to the strong recombination probability of the conducting medium, space-charge are only occurred at the low conducting medium that having low charge carrier mobility. Since the polymer active layer shows low carrier mobility ( $\approx 10^{-3} \text{ cm}^2 \text{ V}^{-1} \text{ s}^{-1}$ ), the concept of space-charge can be applied. For measuring the SCLC of the polymer active layer, the hole-only device and the electron-only device are needed. In particular, the usual hole-only device structure is ITO/HTL/Active layer/HTL/Ag and the usual electron-only device structure is ITO/ETL/Active layer/ETL/Al. Normally, the HTL exhibits both hole transportation property and electron blockage property. In dark condition, when a voltage (V) is applied to the hole-only device, holes are injected into the polymer active layer from one electrode, and electrons are blocked at the opposite electrode. A similar concept is applied in case of the electron-only device. With the assumption that the charge mobility is uniform inside the polymer active layer, the steady-state current density  $J_{SCLC}$  can be written as

$$J_{SCLC} = \frac{9}{8} \mu_{SCLC} \epsilon_r \epsilon_0 \frac{V^2}{d^3} = \frac{9\epsilon_r \epsilon_0}{8d^3} \mu_{SCLC} V^2 \quad (1.9)$$

In equation 1.9,  $d$  is the thickness of polymer active layer,  $\mu_{SCLC}$  is the charge carrier mobility,  $\epsilon_r$  and  $\epsilon_0$  are the dielectric constant of the active layer and the vacuum permittivity, respectively. From the  $(J_{SCLC})^{0.5}$ - $V$  plot, the hole mobility, or electron mobility, of the polymer active layer can be extracted. Furthermore, the SCLC method can be used to examine the carrier

transportation properties of the new material that acted as the carrier transport layer. For example, two hole-only devices were fabricated with the structure as ITO/PEDOT:PSS/active layer/HTLs/Ag, where HTLs were evaporation  $\text{MoO}_x$  or solution-processable NiO. By comparing the extracted hole mobility of two devices, the hole transportation properties of the HTLs can be evaluated since the only difference between them is the HTLs.

## **Chapter 2. The effect of various solvent additives on the power conversion efficiency of polymer-polymer solar cells**

*This chapter is reproduced in part with permission of “Current Applied Physics, Vol 18, Issue 5, Pages 534-540”. Copyright 2018 Korean Physical Society. Published by Elsevier B.V.*

### **2.1 Research Background**

Organic photovoltaic (OPV) cells have gained increasing attention due to their unique advantages such as inexpensive, easy fabrication, rapid energy payback time, light weight, and mechanical flexibility.<sup>[15–18]</sup> Despite significant progress in the area of bulk-heterojunction (BHJ) solar cells based on a mixture of semiconducting conjugated polymers and soluble fullerene derivatives over the past decade,<sup>[19–22]</sup> there have been continuous attempts to replace soluble fullerene acceptors to overcome their various problems including relatively high cost, poor thermal/photochemical stability, and limited light absorption in the visible-near infrared region. Among these problems, the most serious is the thermal stability of soluble fullerenes. In general, fullerenes tend to aggregate under elevated temperatures, resulting in deteriorated morphology and reduced solar cell lifetimes.<sup>[23–25]</sup>

The most popular approach to replace fullerene acceptors in BHJ solar cells is the fabrication of all-polymer solar cells (a-PSCs), in which both donor and acceptor materials that absorb light and transport charges are semiconducting polymers.<sup>[26–29]</sup> As with BHJ solar cells with fullerene acceptors, proper phase separation of n-type polymer and p-type polymer to form bi-continuous charge transport networks is also essential for achieving high efficiency in a-PSCs.<sup>[30–32]</sup> In contrast to solar cells with fullerene acceptors (in which spontaneous phase separation occurs), the deposition of all-polymer photoactive layers with good phase separation is not easy because the photoactive layer of a-PSCs consists of two n-type and p-type polymers having similar mechanical properties. Thus, control of the morphology of the photoactive layer is more critical in a-PSCs.

There have been several methods to control the morphology of the photo-active layer including post-thermal annealing, solvent annealing, and the use of additives. Among them, the additive method is the most widely used for BHJ solar cells with fullerene acceptors. The same basic approaches are used in a-PSCs. The same solvent additives, i.e., 1-chloronaphthalene (CN)<sup>[33–35]</sup>, 1,8-diiodooctane (DIO)<sup>[36–38]</sup>, and diphenylether (DPE)<sup>[39–41]</sup> were used to induce better phase-separated morphologies in the photo-active layer of all-polymer solar cells. It is



well known that the above three additives (CN, DIO, and DPE) have quite different characteristics. For example, DIO can dissolve fullerenes well, but it is a poor solvent for conjugated polymers. CN is a good solvent for both fullerene derivatives and conjugated polymers. DPE can also dissolve both fullerene acceptor and polymers. However, the solubility of DPE is relatively lower than that of CN. Despite these different characteristics, processing additives for a-PSCs have been guided by empirical methods without any clear distinctions.

In this work, we have investigated the effect of three different additives (DIO, CN and DPE) on the performance of a-PSCs based on a BHJ blend consisting of poly[4,8-bis(5-(2-ethylhexyl)thiophen-2-yl)benzo[1,2-b:4,5-b']dithiophene-alt-3-fluorothieno[3,4-b]thiophene-2-carboxylate] (PTB7-Th) as a donor and poly[[N,N'-bis(2-octyldodecyl)-naphthalene-1,4,5,8-bis(dicarboximide)-2,6-diyl]-alt-5,5'-(2,2'-bithiophene)] (P(NDI2OD-T2)) as an acceptor. Similar to the results of previous literature, we showed that the device using the additive exhibited slightly improved performance compared to the device without an additive. However, the efficiency enhancement was not significant. We found that only the optimum points differed based on the type of additive. Only a small amount of CN (which is a good solvent for both fullerene derivatives and conjugated polymers) was required to reach the optimization point. The optimum performance for DIO, which is the most widely used additive in all-polymer solar cells, was obtained at 0.5%. The highest efficiency of 5.55% was revealed from the device processed with 0.5% DPE additive. This efficiency was higher than devices processed with CN or DIO. The role of the additive in polymer solar cells based on a BHJ active layer is to induce good phase separation between the donor and acceptor by morphology enhancement. However, grazing-incidence wide-angle X-ray scattering (GIWAXS) results showed that there was no significant morphology change in the polymer-polymer active layer based on the additive. On the other hand, the intensity modulated photovoltage spectroscopy study showed that a slight increase in the efficiency caused by the additive was due to the change in the recombination characteristics. Overall, our results indicated that the device performances of all-polymer solar cells were not significantly dependent on the type of solvent additive. Rather, determining the optimal fabrication conditions was more critical for achieving the best performance.

## 2.2. Experimental

### 2.2.1 Solution Preparation

PTB7-th (weight-average molecular weight=114 kDa and polydispersity index=2.2) and P(NDI2OD-T2) (weight-average molecular weight=90 kDa and polydispersity index=2.8) were purchased from 1-Material, Inc. Anhydrous solvents such as 1,8-diiodooctane (DIO), 1-chloronaphthalene (CN), diphenylether (DPE) and chlorobenzene (CB) were purchased from Sigma-Aldrich and were used as received. PTB7-Th:P(NDI2OD-T2) (1.3:1 by weight) blend solutions with a total concentration of 12 mg/mL were dissolved in CB. Next, CN, which acted as a solvent additive, was added to the blend solution with volume fractions from 0% to 3% to identify the optimized volume fraction of the solvent additive. The same procedure was performed for DIO and DPE, respectively. All solutions were stirred over 24 h at room temperature in a N<sub>2</sub>-filled glovebox. The 0.75M ZnO precursor solutions were prepared by dissolving zinc acetate dehydrate [Zn(CH<sub>3</sub>COO)<sub>2</sub>·2H<sub>2</sub>O] (Sigma-Aldrich Co., 99.9%) in 2-methoxyethanol (Sigma-Aldrich Co., 99.8%) containing ethanolamine as a stabilizer. The solution was stirred at 60°C for 3 h and then at room temperature for 10 h before spin-coating.

### 2.2.2 Device Fabrication

The inverted bulk heterojunction (BHJ) all-polymer solar cells were fabricated using an ITO/ZnO/PTB7-Th:P(NDI2OD-T2)/MoO<sub>3</sub>/Ag structure. The patterned indium-tin oxide (ITO) was coated on a glass substrate. The substrates were subjected to ultrasonication in deionized water, acetone and isopropyl alcohol, respectively. They were then dried in an oven at 100°C for several hours. Once dried, the substrates were treated with UV zone in 60 mins to increase the hydrophilicity. A ZnO film was coated on the cleaned ITO substrates by spin coating ZnO precursor at 2000 rpm and then annealing at 200 °C for 1 hour in air. The ZnO film was cooled to room temperature and then subjected into an N<sub>2</sub>-filled glovebox to make the solar cell active layer. After passing through a 0.45 μm PTFE syringe filter, the blend solution with and without solvent additive was spin-cast onto the ZnO layer with a spin speed ranging from 2000 rpm to 2500 rpm to create an approximately 100 nm thick active layer. Then, the substrates were placed in the evaporation chamber to make approximately 5 nm of MoO<sub>3</sub> and 100 nm of Ag under a high vacuum pressure less than 10<sup>-6</sup> Torr. The active surface area of the device, as defined by a metal shadow mask, was 0.13 cm<sup>2</sup>.

### 2.2.3 Device Characteristics

The surface morphologies of BHJ layers were measured by using an atomic force microscope (AFM, Nanocute, SII NanoTechnology). The current density-voltage (J-V) curves of the solar cell devices were obtained using a Keithley 2401 source measurement unit under AM1.5G simulated illumination (100 mW/cm<sup>2</sup>). The standard Si-photodiode detector with a KG-3 filter (Newport Co., Oriel) was used to calibrate the intensity of the simulated sunlight. All devices were measured under an inert environment using a solar simulator inside a N<sub>2</sub>-filled glove box. The external quantum efficiency (EQE) of the optimized solar cell performance was determined by IQE-200B (Newport Co., Oriel). Intensity modulated photovoltage spectroscopy (IMVS) was carried out by using an impedance analyzer (IVIUM tech., IviumStat), which measures the optoelectronic frequency response in the frequency range from 1 MHz to 1 Hz. The DC and AC components of the illumination were supplied by the red emission LED ( $\lambda=635$  nm), which was in the absorption range of the donor and acceptor polymer. The modulation depth of the AC component superimposed on the DC light was 10%. IMVS were obtained under open-circuit conditions. The recombination time ( $\tau_r$ ) of the photo-generated charges was obtained from the minimum frequency in the Nyquist plot of IMVS results by setting  $\tau_r = (2\pi f_{\min}(\text{IMVS}))^{-1}$ .

### 2.3 Results and Discussion

**Figure 2.1a** shows a schematic illustration of the device architecture as well as the chemical structures of the photoactive layer materials. a-PSCs were fabricated with an inverted configuration of ITO/ZnO/PTB7-Th:P(NDI2OD-T2)/MoO<sub>3</sub>/Ag. The optimized ratio of PTB7-Th:P(NDI2OD-T2) blend was 1.3:1 (w:w) with a total concentration of 12 mg/ml in chlorobenzene (CB). Details related to the solar cell fabrication process are provided in the experimental section. The energy level diagram shown in **Figure 2.1b** indicates that PTB7-Th:P(NDI2OD-T2) solar cells have good energy level configurations for the photovoltaic effect. **Figure 2.1c** shows the chemical structures of the processing additives utilized in this study.

To make a proper comparison between solar cell performances based on the characteristics of the additives, we initially investigated the optimum ratio of each additive in a-PSC. Note that the control device without processing additive yielded a power conversion efficiency (PCE) of 4.51% with a short-circuit current ( $J_{sc}$ ) of 11.92 mA/cm<sup>2</sup>, an open-circuit voltage ( $V_{oc}$ ) of 0.80 V, and a fill-factor (FF) of 0.473. **Figure 2.2a** shows the current density (J) vs. voltage (V) characteristics of PTB7-Th:P(NDI2OD-T2) solar cells fabricated with various ratios of CN additive. The a-PSC with CN additive showed a highest efficiency of 5.26% at 0.1 vol.% of

CN. The performance of the solar cells gradually decreased with increasing CN ratio. For the solar cells with DIO additive (which is most frequently used in a-PSCs), the best efficiency was 0.5 vol.% as shown in **Figure 2.2b**. The achieved PCE was 5.40% with a  $J_{sc}$  of 12.15 mA/cm<sup>2</sup>, a  $V_{oc}$  of 0.80 V, and a FF of 0.549. After the maximum at 0.5%, the PCE was gradually decreased with increasing DIO content. Even though DPE has characteristics similar to the CN additive, the optimal point of DPE was completely different from that of CN. Rather, it has the same optimal point as DIO. **Figure 2.2c** shows the J-V characteristics of PTB7-Th:P(NDI2OD-T2) solar cells fabricated with various ratios of DPE additive. The best performing solar cell with 0.5 vol.% DPE additive yield a PCE of 5.53% with a  $J_{sc}$  of 12.64 mA/cm<sup>2</sup>, a  $V_{oc}$  of 0.80 V, and a FF of 0.547. The detailed performance data for CN, DIO, and DPE additive obtained during the optimization process are summarized in **Table 2.1**, **Table 2.2**, and **Table 2.3**, respectively.

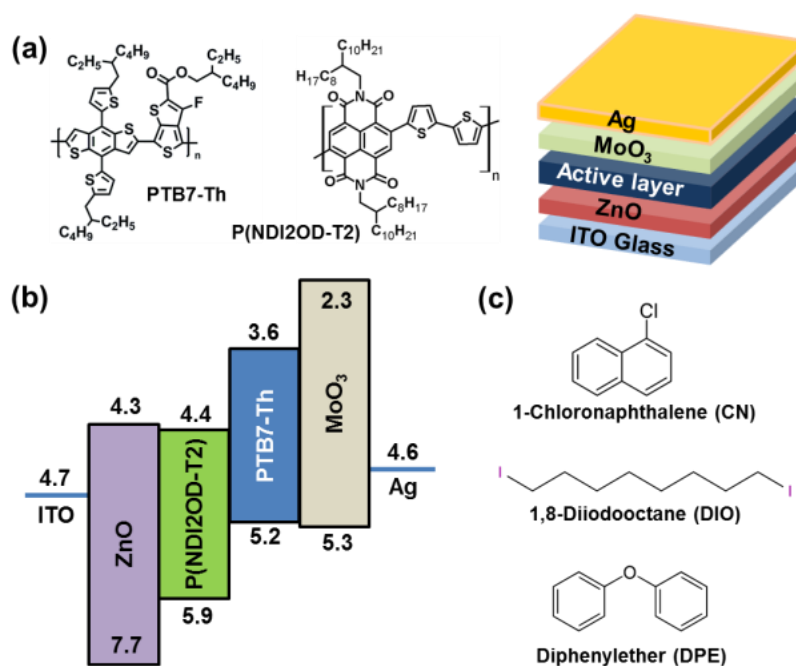


**Figure 2.1** (a) Chemical structure of photoactive materials (donor: PTB7-Th, acceptor: P(NDI2OD-T2)) and schematic illustration of the device structure, (b) Energy level diagram of polymer-polymer solar cell base on PTB7-Th:P(NDI2OD-T2) blend, (c) Chemical structure of the solvent additives.

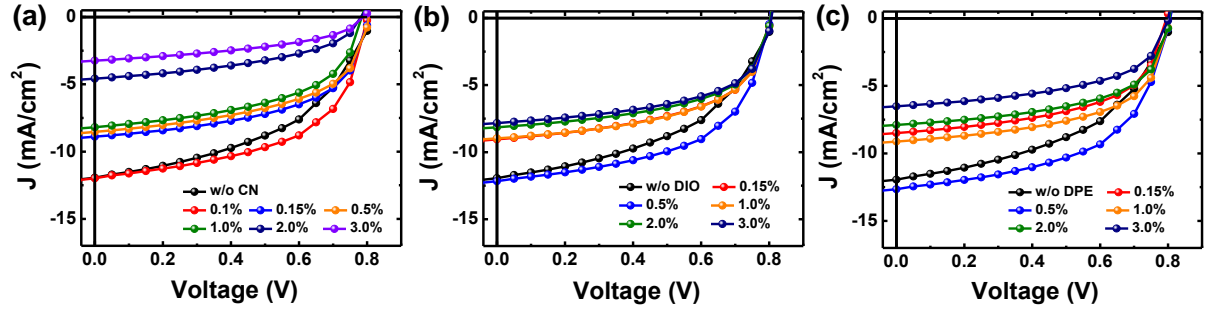


**Figure 2.2** J-V characteristics of PTB7-Th:P(NDI2OD-T2) solar cells fabricated with various ratios of (a) CN additive, (b) DIO additive, and (c) DPE additive.

**Table 2.1** Summarized photovoltaic performance characteristics of a-PSC with various ratio of CN additive.

Condition	$J_{sc}$ [mA/cm <sup>2</sup> ]	$V_{oc}$ [V]	FF [%]	PCE [%]
w/o CN	11.92	0.80	0.473	4.51
0.10 %vol	11.96	0.81	0.543	5.26
0.15 %vol	8.89	0.80	0.545	3.88
0.50 %vol	8.53	0.80	0.531	3.62
1.00 %vol	8.20	0.78	0.524	3.35
2.00 %vol	4.58	0.78	0.460	1.64
3.00 %vol	3.24	0.79	0.440	1.13

**Table 2.2** Summarized photovoltaic performance characteristics of a-PSC with various ratio of DIO additive.

Condition	$J_{sc}$ [mA/cm <sup>2</sup> ]	$V_{oc}$ [V]	FF [%]	PCE [%]
w/o DIO	11.92	0.80	0.473	4.51
0.15 %vol	9.04	0.80	0.544	3.93
0.50 %vol	12.15	0.81	0.549	5.40
1.00 %vol	8.97	0.80	0.550	3.95
2.00 %vol	8.15	0.80	0.555	3.62
3.00 %vol	7.83	0.81	0.560	3.55

**Table 2.3** Summarized photovoltaic performance characteristics of a-PSC with various ratio of DPE additive.

Condition	$J_{sc}$ [mA/cm <sup>2</sup> ]	$V_{oc}$ [V]	FF [%]	PCE [%]
w/o DPE	11.92	0.80	0.473	4.51
0.15 %vol	8.50	0.80	0.550	3.74
0.50 %vol	12.64	0.80	0.547	5.53
1.00 %vol	9.13	0.80	0.573	4.19
2.00 %vol	7.90	0.80	0.565	3.57
3.00 %vol	6.52	0.80	0.533	2.78

**Table 2.4** Summarized photovoltaic performance characteristics of the best a-PSC under the optimized conditions for solvent additives.

Condition	$J_{sc}$ [mA/cm <sup>2</sup> ]	$V_{oc}$ [V]	FF [%]	PCE Avg <sup>a</sup> [%]	PCE Best [%]
w/o Additive	11.92	0.80	0.473	4.39	4.51
CN (0.1%.vol)	11.96	0.81	0.543	5.10	5.26
DIO (0.5%.vol)	11.96	0.81	0.557	5.25	5.40
DPE (0.5%.vol)	12.64	0.80	0.550	5.41	5.56

<sup>a</sup>The average PCE was calculated from values measured over 15 devices.

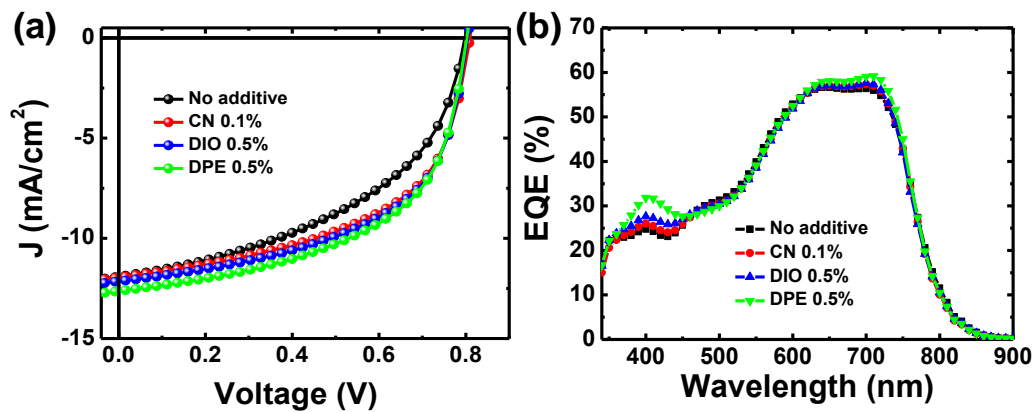


**Figure 2.3** (a) J-V characteristics and (b) EQE spectra of the best PTB7-Th:P(NDI2OD-T2) solar cell fabricated using optimized conditions of solvent additives.

**Figure 2.3a** shows J-V curves obtained from the best solar cell for each additive for comparison. A comparison between the solar cells without additive and with additive indicates that the additive in a-PSC mainly led to improvement in FF. The device using the DPE additive

showed slightly better performance compared to others. This slightly better performance appears to be mainly due to the  $J_{sc}$  improvement. However, the difference was almost negligible. **Figure 2.3b** shows EQE spectra obtained from the highest efficiency cells in each case. Details related to the best performing devices are summarized in **Table 2.4**.

In conventional BHJ solar cells based on polymer donors and fullerene acceptors, additives induce better phase separation between the polymer and fullerene. This well-developed phase separation morphology between active materials offers  $J_{sc}$  improvement by forming good penetration pathways for holes and electrons. In addition, the good phase separation morphology of the active layer can also reduce non-geminate recombination losses, thereby improving FF. To explore these points in a-PSCs based on PTB7-Th:P(NDI2OD-T2), we investigated the morphology of the active layer by using atomic force microscopy (AFM) and a grazing-incidence wide-angle X-ray scattering (GIWAXS). **Figure 2.4** shows the AFM height and phase images of PTB7-Th:P(NDI2OD-T2) thin films with and without additives. A relatively well formed short fibril network structure was observed from phase images in all samples. In addition, slightly enlarged grains were observed in the samples with additives. However, the morphological differences between the samples with CN, DIO or DPE were difficult to identify with AFM measurements.

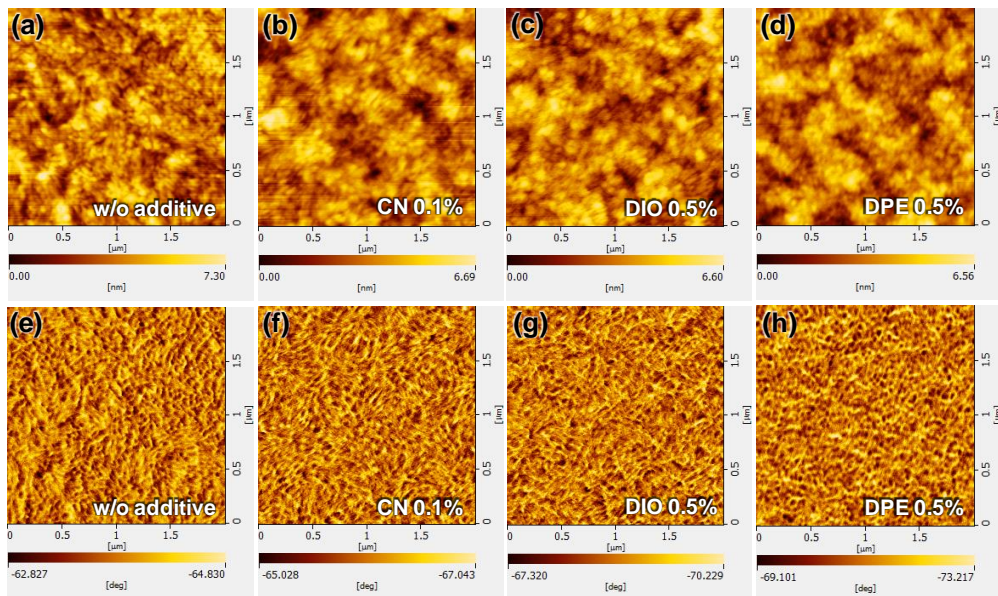


**Figure 2.4** AFM height images (a,b,c,d) and phase images (e,f,g,h) of optimized PTB7-Th:P(NDI2OD-T2) blend films from chlorobenzene with: (a,e) no additive, (b,f) CN 0.1% vol, (c,g) DIO 0.5% vol, (d,h) DPE 0.5% vol.

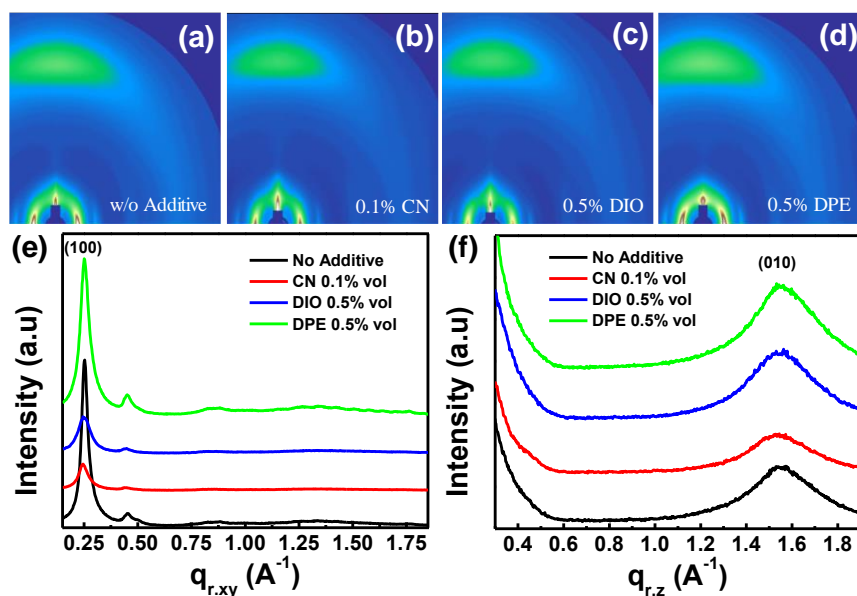


**Figure 2.5** 2D-GIWAXS image of the active layer under optimized conditions with (a) no additive, (b) CN 0.1% vol, (c) DIO 0.5% vol and d) DPE 0.5% vol. The line cut profiles of 2D-GIWAXS images in the (e) in-plane and (f) out-of-plane of PTB7-Th:P(NDI2OD-T2) blend films with the optimum concentration of various solvent additives.

**Figure 2.5** shows the results of a grazing-incidence wide-angle X-ray scattering (GIWAXS) performed to investigate the morphology differences induced by different additives. The in-plane and out-of-plane line cut profiles are presented in **Figure 2.5e** and **Figure 2.5f**, respectively. All samples showed a (100) lamellar peak in the in-plane line cut profile and a (010)  $\pi$ - $\pi$  stacking peak in the out-of-plane line cut profile. The (100) lamellar peak and the (010)  $\pi$ - $\pi$  stacking peak in each condition were located at the same position at  $q_{r,xy}=0.25 \text{ \AA}^{-1}$  and  $q_{r,z}=1.56 \text{ \AA}^{-1}$ , respectively. The absence of the (010)  $\pi$ - $\pi$  stacking peak in the in-plane line cut profile indicated that polymers have face-on orientation, wherein the  $\pi$ - $\pi$  stacking direction is vertical to the substrate. The out-of-plane line cut of GIWAXS showed that the  $\pi$ - $\pi$  spacing of the polymers was in the range of 3.5-4.5 nm. The in-plane line cut of GIWAXS showed that the lamella spacing of the polymers was approximately 25 nm.

The overall results of GIWAXS indicate that the morphological features of all-polymer photoactive layers were not affected by the presence of additive or the type of additive. However, this is only true when the additive is used at the optimum ratio. It appears that the morphology of the active layer is disturbed if it deviates from the optimum ratio. For non-optimized additive ratios, mixing of face-on orientation and edge-on orientation was observed in 2D-GIWAXS obtained from the samples with 3.0%.vol of CN, DIO, and DPE as shown in **Figure 2.6**. In the case of CN and DPE additive, the (200) lamellar peak was clearly observed.



The (200) peak is the feature of high order crystalline P(NDI2OD-T2) with edge-on orientation to the substrate.<sup>[42,43]</sup> The intensity of the (200) lamellar peak of crystalline P(NDI2OD-T2) with 3% CN additive was higher than that of crystalline P(NDI2OD-T2) with 3% DPE additive, which means that the amount of edge-on oriented crystalline P(NDI2OD-T2) domain was higher in the active layer with 3% CN additive. Generally, photoactive layers with face-on orientation in a-PSCs show higher performance than the photoactive layer with edge-on orientation due to the reduction in geminate recombination.<sup>[44,45]</sup> Therefore, an increase in edge-on oriented crystalline domain of P(NDI2OD-T2) can suppress the performance of the solar cell. For this reason, the a-PCS with CN additive showed the largest difference in efficiency between the optimized ratio and 3% additive (see **Table 2.1**). For the same reason, the a-PCS with DIO additive (which has no (200) lamella peak) showed the smallest difference in efficiency between the optimized ratio and 3% additive (see **Table 2.2**).

If there is no morphology difference between solar cells with no additives and solar cells with additives, what causes the difference in efficiency? **Table 2.4** shows that the difference in solar cell efficiency is due to the difference in FF.<sup>[46,47]</sup> In cases where  $V_{oc}$  and  $I_{sc}$  are similar, the difference in FF is most likely due to the recombination of charge carriers. To investigate the recombination process in a-PSCs with and without additive, we performed intensity modulated photovoltage spectroscopy (IMVS) as shown in **Figure 2.7**. IMVS was performed under open-circuit conditions. In an open-circuit configuration, the solar cell reaches steady-state at the open-circuit potential, which means that the rate of charge injection is equal to the charge recombination rate. Thus, IMVS provides information about the carrier lifetime and electron-hole recombination dynamics under open-circuit conditions. In IMVS, the frequency semi-circle minimum in the complex plane corresponds to the recombination time. The calculated recombination times were 2.00  $\mu s$  for the a-PCS without additive, 2.16  $\mu s$  for the a-PCS with 0.1% CN, 2.34  $\mu s$  for the a-PCS with 0.5% DIO, and 2.52  $\mu s$  for the a-PCS with 0.5% DPE. The results for recombination time coincided with the solar cell efficiency. Therefore, we concluded that the efficiency enhancement in the device with additives originated from the improved recombination process. The increased recombination resistance is presumably due to a change in the microstructure of the active layer due to the effect of the additive.

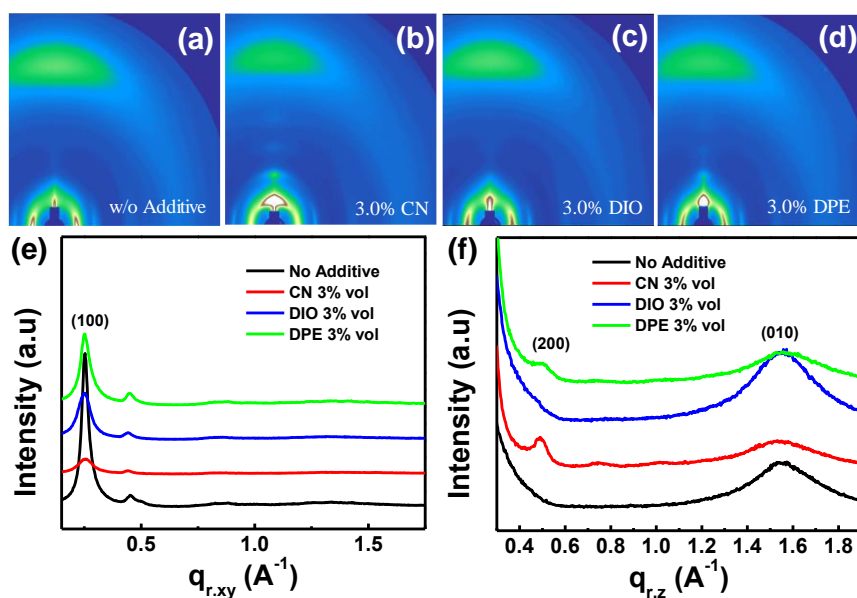


**Figure 2.6** 2D-GIWAXS image of the active layer under non-optimized conditions with (a) no additive, (b) CN 3% vol, (c) DIO 3% vol and (d) DPE 3% vol. The line cut profile of 2D-GIWAXS image in the (e) in-plane and (f) out-of-plane of PTB7-Th:P(NDI2OD-T2) blend films with a non-optimum concentration of various solvent additives.

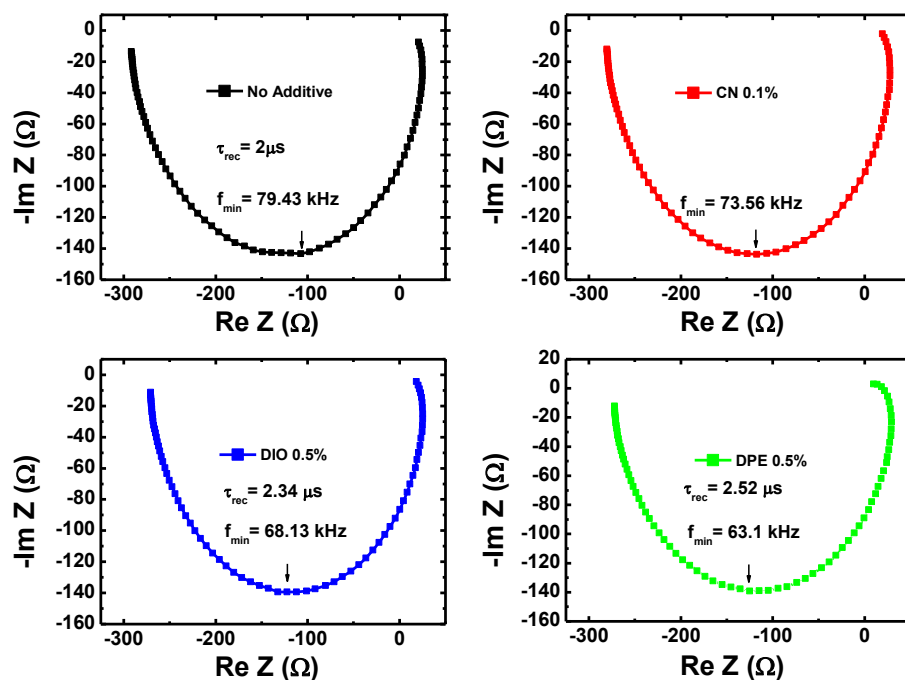


**Figure 2.7** Intensity modulated photo-voltage spectroscopy (IMVS) of a-PCS with (a) no additives, (b) CN 0.1% vol, (c) DIO 0.5% vol and (d) DPE 0.5% vol.

## 2.4 Conclusion

In summary, we have investigated the effect of three different additives (DIO, CN, DPE) on the performance of polymer-polymer solar cells based on a BHJ mixture consisting of PTB7-Th as a donor and P(NDI2OD-T2) as an acceptor. A comparison of the efficiency between the solar cell without additive and the device with additive indicated that the device using the additive exhibited an improved performance, similar to the results of previous literature. However, the efficiency enhancement was not significant. Moreover, the performances of polymer-polymer solar cells were not significantly dependent on the type of additive. We found that only the optimum points differed depending on the type of additive.

In general, the role of additive in organic solar cells based on the BHJ active layer is to induce good phase separation between the donor and acceptor. However, GIWAXS results showed that there was no significant morphology change in the polymer-polymer active layer due to the additive. All polymer-polymer active layers with the optimal additive ratio had only face-on orientation, which is a good condition for achieving higher efficiency in polymer-polymer solar cells. On the other hand, non-optimized conditions resulted in polymer-polymer active layers with a mixture of face-on orientation and edge-on orientation. This is likely the reason for the decrease in efficiency observed for excess additive. IMVS measurements showed that the performance enhancements in solar cells with additive were because of reduced recombination rather than crystalline morphology improvements.

## Chapter 3. 17% non-fullerene organic solar cells with annealing-free aqueous MoO<sub>x</sub>

*This chapter is reproduced in part with permission of “Advanced Science, Vol 7, Issue 21, 2002395”. Copyright 2020 The Authors. Published by Wiley-VCH GmbH.*

### 3.1 Research Background

Polymer solar cells (PSCs) based on organic semiconductors are considered the most promising candidate as a future mobile energy source due to their advantages, including light weight, low cost, flexibility, and simple fabrication process with the possibility of printable or roll-to-roll mass production.<sup>[18,48–52]</sup> The power conversion efficiency (PCE) of single junction polymer solar cells has steadily increased and recently reached over 16% due to the development of novel high quality donor and acceptor materials.<sup>[53–56]</sup> The increment of the efficiency of polymer solar cells was achieved by not only the development of higher performing new donor and acceptor materials, but also by improving the quality of charge transport layers (or called electrode buffer layers) such as the hole transport layer (HTL) and electron transport layer (ETL) inserted between the active layer and electrodes.<sup>[57]</sup> It is clearly known that the inserted charge transport layers induce significantly improved efficiency by enhancing the charge extraction property and reducing leak currents which occur due to undesirable opposite charge flow. In addition, charge transport layers also have a significant influence on the stability of PSCs.

In earlier studies on polymer solar cells, poly(3,4-ethylenedioxythiophene):poly(styrenesulfonate) (PEDOT:PSS) was the most popular hole transporting material because of its high conductivity and well-matched work-function (~5.1 eV) for the highest occupied molecular orbital (HOMO) level of general donor polymers.<sup>[58–61]</sup> However, since it is known that the acidity of PEDOT:PSS may cause degradation of both the ITO electrode and active layer,<sup>[62–64]</sup> there has been extensive research on HTL materials to replace PEDOT:PSS. Among the several materials that can be utilized as an alternative to PEDOT:PSS, the most prominent candidate materials are transition metal oxides such as MoO<sub>3</sub>, V<sub>2</sub>O<sub>5</sub>, NiO, and WO<sub>3</sub> due to their good charge transport properties and high stability.<sup>[9,65–67]</sup> In particular, MoO<sub>3</sub> is the most widely utilized as a HTL in PSCs.

There are many ways to prepare the molybdenum oxide buffer layer, including a wet chemical sol-gel method, thermal evaporation, chemical vapor deposition, and pulsed laser deposition.<sup>[68–71]</sup> Normally, solution-processable MoO<sub>x</sub> prepared by the sol-gel method has

been mainly utilized for PSCs with a conventional structure. In the case of inverted PSCs, the thermal evaporation method is preferred for the deposition of the MoO<sub>x</sub> HTL. This is because of the necessity of a high temperature annealing step to achieve the desired hole transporting property in the case of solution-processable MoO<sub>x</sub>. Unfortunately, normal organic-based photovoltaic materials are not able to withstand high temperature annealing well. Moreover, the high-temperature annealing process also acts as a disadvantage in the fabrication of flexible devices because general flexible substrates are not able to withstand high-temperature annealing above 150 °C. Therefore, the development of annealing-free solution-processable metal oxides including MoO<sub>x</sub> is essential for the large-scale commercialization of flexible PSCs.

Depending on the nature of the base solvent, the sol-gel method can be classified into two routes: an aqueous sol-gel method and anhydrous sol-gel method. The difference between these two routes is whether water is used as the base solvent or not. In the aqueous sol-gel route, water and alcoholic solvents are used as the reaction medium, while in the anhydrous sol-gel route, only organic solvents are used as the reaction medium. Typically, MoO<sub>x</sub> prepared by the anhydrous sol-gel method using MoO<sub>2</sub>(acac)<sub>2</sub> is needed for high-temperature curing to result in high quality. For example, Li and coworkers reported that MoO<sub>x</sub> HTL deposited by spin coating of a precursor solution prepared through the dilution of MoO<sub>2</sub>(acac)<sub>2</sub> in anhydrous isopropanol is needed for high temperature annealing over 150 °C in air.<sup>[72]</sup> Riedl et al. also reported that the MoO<sub>x</sub> film prepared by solution processing required high temperature annealing over 150 °C in a N<sub>2</sub> atmosphere to obtain a high work function of 5.3 eV.<sup>[4]</sup>

In our present work, we developed annealing-free solution-processable ‘aqueous’ MoO<sub>x</sub> (aq-MoO<sub>x</sub>), and applied it in a bulk-heterojunction (BHJ) PSC. An important reason for the high-temperature annealing step after MoO<sub>x</sub> film deposition is to remove the ligands. We found that the acetylacetonate ligand of MoO<sub>2</sub>(acac)<sub>2</sub> can be easily removed through the simple hydrolysis caused by a small amount of water. By adjusting the concentration of water in the sol-gel route for the MoO<sub>x</sub> precursor, we successfully developed an annealing-free MoO<sub>x</sub> HTL with excellent electrical properties. The non-fullerene solar cell based on a blend of poly[(2,6-(4,8-bis(5-(2-ethylhexyl-3-fluoro)thiophen-2-yl)-benzo)[1,2-b:4,5-b']dithiophene))-alt-(5,5-(1',3'-di-2-thienyl-5',7'-bis(2-ethylhexyl)benzo[1',2'-c:4',5'-c']dithiophene-4,8-dione) (PBDB-T-2F, also called PM6) and non-fullerene acceptor (2,2'-((2Z,2'Z)-((12,13-bis(2-ethylhexyl)-3,9-diundecyl-12,13-dihydro-[1,2,5]thiadiazolo[3,4-e]thieno[2,"3":4',5']thieno[2',3':4,5]pyrrolo[3,2-g]thieno[2',3':4,5]thieno[3,2-b]indole-2,10-diyl)bis(methanylylidene))bis(5,6-difluoro-3-oxo-2,3-dihydro-1H-indene-2,1-diylidene))dimalononitrile) (Y6) with the general MoO<sub>x</sub>

layer prepared by the anhydrous sol-gel method showed a poor efficiency of 7.7% without annealing. If this anhydrous MoO<sub>x</sub> (an-MoO<sub>x</sub>) layer was annealed at 200 °C, the efficiency was recovered to 17.1% which was normal value typically observed in conventional structure PBDB-T-2F:Y6 solar cells. However, without any annealing process, the solar cell with aq-MoO<sub>x</sub> exhibited comparable performance of 17.0%. In addition, the solar cell with annealing-free aq-MoO<sub>x</sub> exhibited better performance and stability without high-temperature annealing compared to the solar cells with PEDOT:PSS. A similar trend was observed in a fullerene system solar cell based on a blend of poly[4,8-bis(5-(2-ethylhexyl)thiophen-2-yl)benzo[1,2-b:4,5-b']dithiophene-alt-3-fluorothieno[3,4-b]thiophene-2-carboxylate] (PTB7-Th) and [6,6]-phenyl-C71-butyric acid methyl ester (PC<sub>71</sub>BM). The PTB7-Th:PC<sub>71</sub>BM solar cell with non-annealed an-MoO<sub>x</sub> showed very low efficiency of 1.37%, while the solar cell with annealing-free aq-MoO<sub>x</sub> exhibited a higher efficiency and better stability without high-temperature annealing compared to the solar cells with PEDOT:PSS.

## 3.2 Experimental

### 3.2.1 Preparation of the MoO<sub>x</sub> Solution

Molybdenum dioxydiacetylacetonate (MoO<sub>2</sub>(acac)<sub>2</sub> 99%) was purchased from Sigma-Aldrich and used as the precursor material for the aqueous and anhydrous MoO<sub>x</sub> solutions. For the anhydrous solution, MoO<sub>2</sub>(acac)<sub>2</sub> (12 mg mL<sup>-1</sup>) was diluted in 10 mL of anhydrous ethanol 99.9% and stirred for 1 hour to obtain a clear and colorless solution. In the case of the aqueous solution, MoO<sub>2</sub>(acac)<sub>2</sub> (12 mg mL<sup>-1</sup>) was diluted in a mixture of 1 mL anhydrous ethanol 99.9% (Sigma-Aldrich) and 9 mL of deionized water. Ethanol was added to improve the solubility of MoO<sub>2</sub>(acac)<sub>2</sub> and hydrophilicity of aq-MoO<sub>x</sub> solution. The aqueous solution was stirred for 1 hour to obtain a light-blue solution. Both aqueous and anhydrous solutions were kept at room temperature for aging over 10 days, which are needed for completely hydrolysis process of MoO<sub>x</sub> solution, to obtain ready to use dark-blue color solutions. To prepare the MoO<sub>x</sub> solution used for the inverted polymer solar cell, Triton X-100 (Sigma-Aldrich) was mixed with the MoO<sub>x</sub> aqueous solution at a ratio of 2:4 (mg:mL), which is denoted as ratio 0.5. The Triton X-100:MoO<sub>x</sub> solution was ultrasonicated for 2 hours and kept at room temperature.

### 3.2.2 Device Fabrication

The conventional bulk heterojunction (BHJ) polymer solar cells were fabricated using an ITO/MoO<sub>x</sub>/PTB7-Th:PC<sub>71</sub>BM/ZnO/Al structure. The patterned indium-tin oxide (ITO) substrates were subjected to ultrasonication in deionized water, acetone, and isopropyl alcohol, respectively. They were then dried in an oven at 100 °C for several hours. Once dried, the substrates were treated with UV for 60 minutes to increase the hydrophilicity. The MoO<sub>x</sub> film was coated on the cleaned ITO substrates by spin coating the aqueous MoO<sub>x</sub> solution or anhydrous MoO<sub>x</sub> solution at 5,000 rpm followed by annealing at 50 °C or 200 °C for 10 minutes in air. Then, the MoO<sub>x</sub> film was cooled to room temperature and then placed into an N<sub>2</sub>-filled glovebox to make the solar cell active layer. The PTB7-Th:PC<sub>71</sub>BM (1:1.5 by weight) blend solution was prepared by dissolving in chlorobenzene with 3% DIO as an additive to achieve better phase separation. The PBDTPD-HT:IDIC (1:1.5 by weight) blend solution was prepared by dissolving in chloroform with 0.6% DIO additive. The PBDB-T-2F:Y6 (1:1.2 by weight) blend solution was prepared by dissolving in chloroform with 0.5% CN additive. The solution was stirred for 1 day before using. After passing through a 0.45 μm PTFE syringe filter, the blend solution was spin-cast onto the MoO<sub>x</sub> layer with a spin speed ranging from 900 rpm to 1,100 rpm to create an approximately 100 nm thick active layer of PTB7-Th:PC<sub>71</sub>BM. In case of PBDTPD-HT:IDIC and PBDB-T-2F:Y6, a spin speed ranging from 3000 rpm to 4000 rpm is used. A ZnO nanoparticle solution (2.5 wt% in IPA) diluted in IPA at a ratio of 1:5 was spin coated on top of the active layer at 5,000 rpm. The devices were kept inside the glovebox for 1 hour for drying at room temperature. Then, the devices were placed in the evaporation chamber to make 100 nm of Al under a high vacuum pressure of less than 10<sup>-6</sup> Torr. The active surface area of the device, as defined by a metal shadow mask, was 0.13 cm<sup>2</sup>. For the reference device, PEDOT:PSS (CLEVIOS PH1000), which was substituted for the MoO<sub>x</sub> layer, was spin-coated on top of ITO substrate at 5,000 rpm and annealed at 150 °C in air.

The inverted bulk heterojunction (BHJ) polymer solar cells were fabricated using an ITO/ZnO/PTB7-Th:PC<sub>71</sub>BM/MoO<sub>x</sub>/Ag structure. A ZnO nanoparticle solution (2.5 wt% in IPA) diluted in IPA at a ratio of 1:1 was spin-coated on top of the ITO substrate at 5,000 rpm and annealed at 85 °C for 10 minutes in air. Then, the ZnO film was cooled to room temperature and then placed in a N<sub>2</sub>-filled glovebox to make the solar cell active layer. The PTB7-Th:PC<sub>71</sub>BM blend solution was spin-cast onto the ZnO layer at 1,000 rpm. A Triton X-100:MoO<sub>x</sub> aqueous solution was spin-coated on top of the active layer at 3,000 rpm and the devices were dried inside the glovebox for 1 hour without using any post-treatment annealing

temperature. For the reference device, modified PEDOT:PSS (M-PEDOT) was spin-coated on top of the active layer at 5,000 rpm and annealed at 80 °C for 10 minutes. Then, the devices were placed in the evaporation chamber to make 100 nm of Ag under a high vacuum pressure of less than  $10^{-6}$  Torr and the active surface area of the device was 0.13 cm<sup>2</sup>. The non-fullerene polymer solar cell was fabricated using the same procedure described above, except that PBDTTPD-HT:IDIC was used as the polymer active layer.

### 3.2.3 Device Characteristics

The current density-voltage curves of the solar cell devices were obtained using a Keithley 2401 source measurement unit under AM1.5G simulated illumination (100 mW/cm<sup>2</sup>). A standard Si photodiode detector with a KG-3 filter (Newport Co., Oriel) was used to calibrate the intensity of the simulated sunlight. All devices were measured under an inert environment using a solar simulator inside a N<sub>2</sub>-filled glove box. The external quantum efficiency (EQE) of the optimized solar cell performance was determined by the IQE-200B (Newport Co., Oriel). The absorption and transmittance spectra of MoO<sub>x</sub> were measured by using a UV-VIS spectrophotometer (Varian, Carry 5000). The surface morphologies of the MoO<sub>x</sub> layers and Triton X-100:MoO<sub>x</sub> layer were measured by using an atomic force microscope (AFM, Nanocute, SII NanoTechnology). UPS and XPS were carried out with an ESCALAB 250-XI surface analysis system equipped with a He-discharge lamp providing He-I photons with an energy of 21.22 eV for UPS analysis and a monochromatic Al-K $\alpha$  X-ray gun with a photon energy of 1,486.6 eV for the XPS investigation. The base vacuum pressure of the analysis system was  $\approx 10^{-7}$  Torr. The Fermi edge was calibrated using a clean Au film and all spectra were plotted with respect to the determined Fermi level. All XPS measurements were calibrated with reference to the Au 4f<sub>7/2</sub> core level (83.98 eV) of a freshly deposited Au film. All binding energies were normalized with the C 1s peak as an internal standard. CE and CELIV were conducted using the CE and CELIV analyzer functions of an organic semiconductor parameter test system (McScience T4000) under 1.0 sun at V<sub>OC</sub> conditions. Fourier transformed infrared spectroscopy (FTIR) was conducted using a Bruker Invenio R spectrometer. Impedance spectroscopy (IS) was carried out by using an impedance analyzer (IVIUM tech, IviumStat) under dark conditions, which measured the optoelectronic frequency response in the frequency range of 1 MHz to 1 Hz. The thickness of various hole transport layers was determined by using Stylus Profilometry (Bruker Dektak XT). The hole mobilities of various hole transport layers (HTLs)/active layer were measured by the steady-state space-charge-limited current (SCLC) method. The structures of the hole-only device were ITO/HTLs/PBDB-T-2F:Y6/MoO<sub>x</sub>/Ag.



The hole mobility of HTLs/active layer was determined by Mott-Gurney law in the SCLC trap free regime, by using the slope of  $J^{0.5}$  vs  $V$ .

### 3.3 Results and Discussion

**Figure 3.1a** shows the schematic diagrams of the PSCs with a conventional structure and the chemical structures of the materials used in this study. Molybdenyl acetylacetonate [ $\text{MoO}_2(\text{acac})_2$ ] was used as the starting material for preparing the an- $\text{MoO}_x$  and aq- $\text{MoO}_x$  solutions. The details regarding the fabrication of the an- $\text{MoO}_x$  and aq- $\text{MoO}_x$  solutions are described in the Experimental Section. **Figure 3.1b** shows the energy level diagram of the PSC with the conventional structure. To investigate the effect of aq- $\text{MoO}_x$  on non-fullerene solar cells, a combination of PBDB-T-2F and non-fullerene acceptor Y6,<sup>[73,74]</sup> and a combination of poly[1-(5-(4,8-bis(5-(2-ethylhexyl)thiophen-2-yl)-6-methylbenzo[1,2-b:4,5-b']dithiophen-2-yl)-4-hexylthiophen-2-yl)-3-(4-hexyl-5-methylthiophen-2-yl)-5-octyl-4H-thieno[3,4-c]pyrrole-4,6(5H)-dione] (PBDTTPD-HT) and 2,2'-((2Z,2'Z)-((4,4,9,9-tetrahexyl-4,9-dihydro-s-indaceno[1,2-b:5,6-b']dithiophene-2,7-diyl)bis(methanylylidene))bis(3-oxo-2,3-dihydro-1H-indene-2,1-diylidene))dimalononitrile (IDIC) were utilized as the donor and acceptor materials.<sup>[75]</sup> For the fullerene-based active layer, PTB7-Th and  $\text{PC}_{71}\text{BM}$  were used as the photoactive materials. For the electrons transport layer, solution-processable ZnO nanoparticles (nanoparticle suspension) that can be processed at room temperature were used.

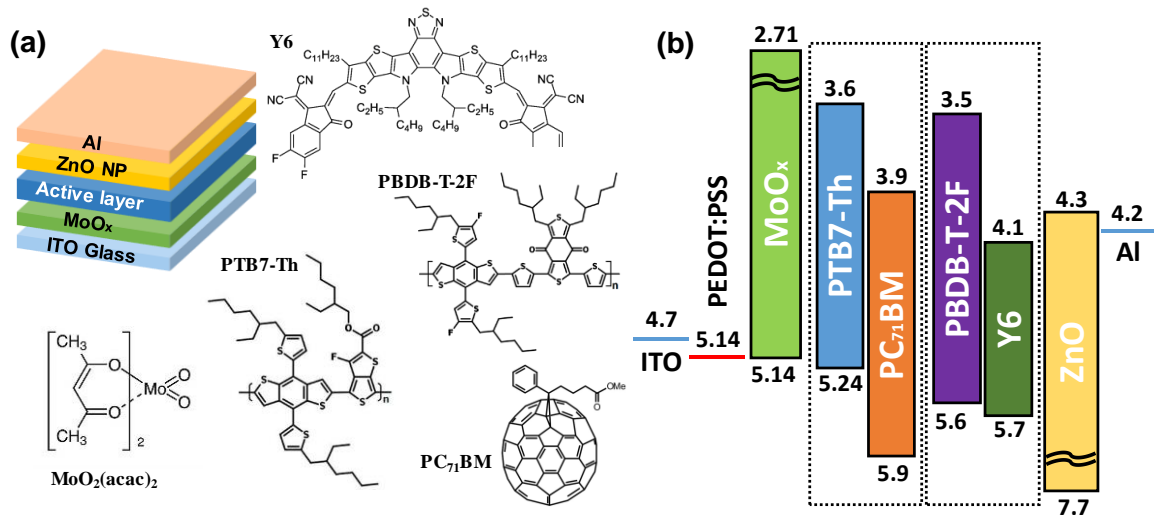


**Figure 3.1** (a) Schematic diagrams of the PSCs with a conventional structure as well as the chemical structure of the materials and b) the energy level diagram of the PSC with a conventional structure.

**Figure 3.2a** and **Figure 3.2d** show the current density ( $J$ ) versus voltage ( $V$ ) characteristics of the PBDB-T-2F:Y6 non-fullerene solar cells (**Figure 3.2a**) and PTB7-Th:PC<sub>71</sub>BM solar cells (**Figure 3.2d**) fabricated using aq-MoO<sub>x</sub> or an-MoO<sub>x</sub>, respectively. In addition, the  $J$ - $V$  characteristics and photovoltaic parameters of the PBDTTPD-HT:IDIC was shown in **Figure 3.3a**. The  $J$ - $V$  results obtained from the device with the PEDOT:PSS HTL are presented for comparison. Note that the PEDOT:PSS film was annealed at 150 °C after spin-coating. The external quantum efficiency (EQE) spectra of the PBDB-T-2F:Y6, PBDTTPD-HT:IDIC non-fullerene solar cells, and PTB7-Th:PC<sub>71</sub>BM solar cells are presented in **Figure 3.4**. The details related to the performance of PTB7-Th:PC<sub>71</sub>BM, PBDTTPD-HT:IDIC, and PBDB-T-2F:Y6 solar cells are listed in **Table 3.1**. The PBDB-T-2F:Y6 solar cell with the non-annealed an-MoO<sub>x</sub> HTL showed a very low power conversion efficiency of 7.7% with a relatively low short-circuit current density ( $J_{sc}$ ) of 20.50 mA/cm<sup>2</sup>, an open-circuit voltage ( $V_{oc}$ ) of 0.826 V, and a fill factor ( $FF$ ) of 45.2%. These results are inevitable consequences of the general non-annealed MoO<sub>x</sub> HTL prepared by the anhydrous sol-gel method because there was no chance to remove the ligands from the MoO<sub>x</sub> HTL without high-temperature annealing. In fact, if the MoO<sub>x</sub> HTL is prepared with high-temperature annealing at 200 °C, the efficiency of the solar cell fabricated with the an-MoO<sub>x</sub> HTL recovered to a normal level of 17.1% with a  $J_{sc}$  of 27.43 mA/cm<sup>2</sup>, a  $V_{oc}$  of 0.845 V, and a  $FF$  of 73.8%. However, the solar cell with aq-MoO<sub>x</sub> prepared by the aqueous sol-gel method showed almost comparable performance to the solar cell with the annealed an-MoO<sub>x</sub> HTL, even without high-temperature annealing. Note that the aq-MoO<sub>x</sub> HTL was kept at 50 °C for 5~10 minutes to dry the surface because a hydrophobic organic active layer was not deposited well on top of the aq-MoO<sub>x</sub> HTL without removing surface moisture. The solar cell with aq-MoO<sub>x</sub> yields a PCE of 17.0% with a  $J_{sc}$  of 27.53 mA/cm<sup>2</sup>, a  $V_{oc}$  of 0.843 V, and a  $FF$  of 73.1%. The solar cell with aq-MoO<sub>x</sub> exhibited better performance compared to the solar cell with the PEDOT:PSS HTL. Moreover, the performance of PBDB-T-2F:Y6 solar cells with the aq-MoO<sub>x</sub> HTL did not change even after annealing at high temperatures of up to 200°C, as shown in **Figure 3.2b** (see **Table 3.2** for details performance). The optical properties of these three MoO<sub>x</sub> HTLs did not differ significantly from each other, as shown in **Figure 3.2c**. However, the MoO<sub>x</sub> HTL exhibited a slightly higher transmittance in the visible region compared to PEDOT:PSS.

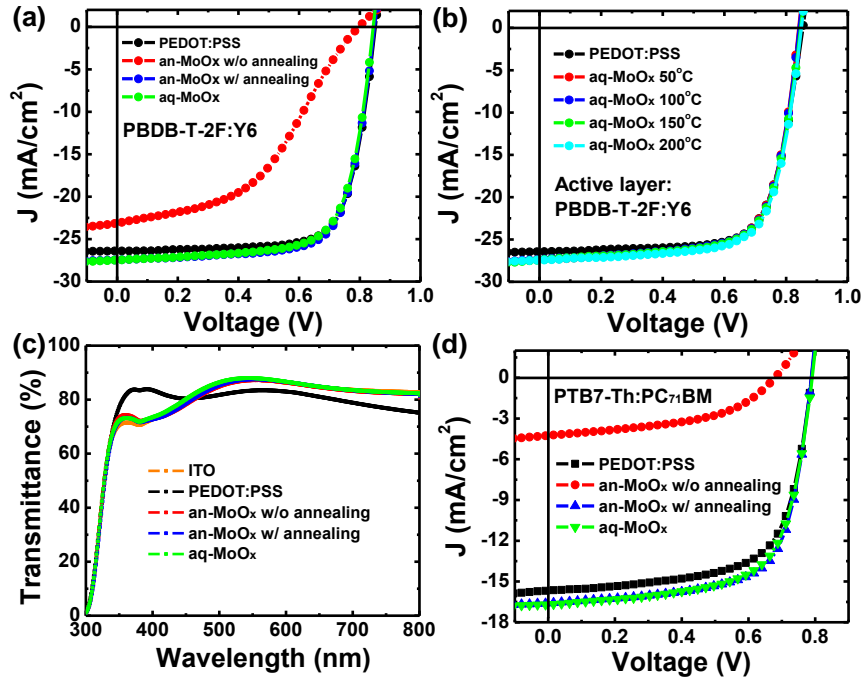


**Figure 3.2** (a)  $J$ - $V$  characteristics of the PBDB-T-2F:Y6 solar cells, (b)  $J$ - $V$  characteristics of the PBDB-T-2F:Y6 solar cells with aq-MoO<sub>x</sub> annealed at various temperatures, (c) transmittance spectra of PEDOT:PSS, an-MoO<sub>x</sub>, and aq-MoO<sub>x</sub>, and (d)  $J$ - $V$  characteristics of the fullerene-based solar cell based on PTB7-Th:PC<sub>71</sub>BM.

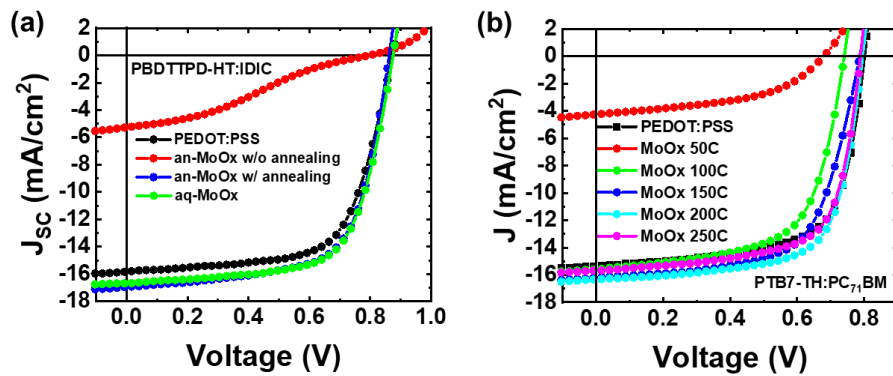


**Figure 3.3**  $J$ - $V$  characteristics of the conventional polymer solar cell based on (a) PBDTTPD-HT:IDIC blend films with various hole transport layers, and (b) PTB7-Th:PC<sub>71</sub>BM blend films with an anhydrous MoO<sub>x</sub> film as a function of the annealing temperature.

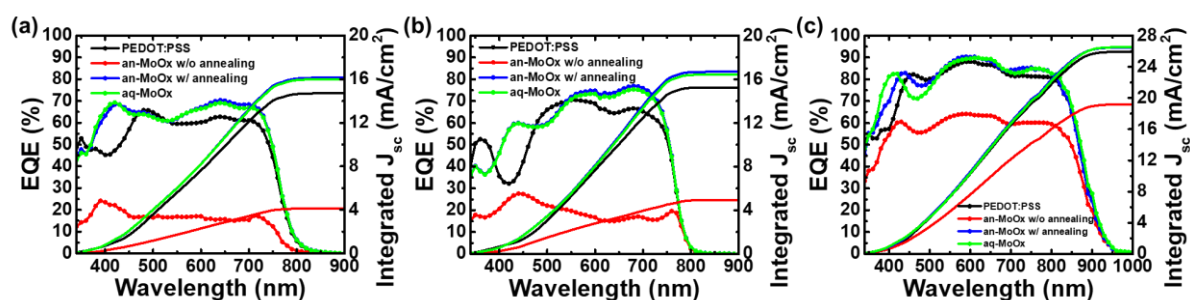


**Figure 3.4** (a) EQE spectra of the solar cell based on PTB7-Th and PC<sub>71</sub>BM. (b) EQE spectra of the solar cell based on PBDTTPD-HT and IDIC. (c) EQE spectra of the solar cell based on PBDB-T-2F and Y6.

**Table 3.1** Summarized photovoltaic parameters of the conventional polymer solar cell based on PTB7-Th:PC<sub>71</sub>BM and non-fullerene solar cell based on PBDB-T-2F:Y6 or PBDTTPD-HT:IDIC.

Active Layer	Description	JV J <sub>sc</sub> [mA/cm <sup>2</sup> ]	EQE J <sub>sc</sub> [mA/cm <sup>2</sup> ]	V <sub>oc</sub> [V]	FF [%]	Best PCE [%]
	PEDOT:PSS	26.50	26.14 (98.6%)	0.854	0.735	16.6
PBDB-T-2F & Y6	Anhydrous MoO <sub>x</sub>	20.50	20.02 (97.6%)	0.826	0.452	7.7
	Anhydrous MoO <sub>x</sub> (200 °C)	27.43	26.87 (97.9%)	0.845	0.738	17.1
	Aqueous MoO <sub>x</sub>	27.53	26.91 (97.7%)	0.843	0.731	17.0
	PEDOT:PSS	15.82	15.25 (96.4%)	0.871	0.661	9.1
PBDTTPD-HT & IDIC	Anhydrous MoO <sub>x</sub>	5.27	4.92 (93.4%)	0.801	0.302	1.3
	Anhydrous MoO <sub>x</sub> (200 °C)	16.94	16.70 (98.6%)	0.861	0.661	9.6
	Aqueous MoO <sub>x</sub>	16.68	16.43 (98.5%)	0.872	0.671	9.7
	PEDOT:PSS	15.67	14.88 (94.9%)	0.791	0.673	8.3
PTB7-Th & PC <sub>71</sub> BM	Anhydrous MoO <sub>x</sub>	4.25	4.12 (96.9%)	0.683	0.479	1.4
	Anhydrous MoO <sub>x</sub> (200 °C)	16.60	16.35 (98.5%)	0.791	0.682	9.0
	Aqueous MoO <sub>x</sub>	16.69	16.20 (97.1%)	0.790	0.671	8.9

**Table 3.2** Summarized photovoltaic parameters of the conventional polymer solar cell based on “PBDB-T-2F:Y6 with an aqueous MoO<sub>x</sub> film” and “PTB7-Th:PC<sub>71</sub>BM with an anhydrous MoO<sub>x</sub> film” as a function of the annealing temperature.

Active Layer	Description	JV J <sub>sc</sub> [mA/cm <sup>2</sup> ]	V <sub>oc</sub> [V]	FF [%]	Best PCE [%]
PBDB-T-2F & Y6	PEDOT:PSS	26.44	0.86	0.72	16.25
	Aqueous MoO <sub>x</sub> 50 °C	27.40	0.84	0.71	16.27
	Aqueous MoO <sub>x</sub> 100 °C	27.30	0.84	0.70	16.21
	Aqueous MoO <sub>x</sub> 150 °C	27.28	0.85	0.70	16.19
	Aqueous MoO <sub>x</sub> 200 °C	27.38	0.85	0.70	16.38
PTB7-Th & PC <sub>71</sub> BM	PEDOT:PSS	15.67	0.79	0.67	8.27
	Anhydrous MoO <sub>x</sub> 50 °C	4.25	0.68	0.48	1.37
	Anhydrous MoO <sub>x</sub> 100 °C	15.59	0.74	0.64	7.33
	Anhydrous MoO <sub>x</sub> 150 °C	16.20	0.79	0.64	8.15
	Anhydrous MoO <sub>x</sub> 200 °C	16.60	0.79	0.68	8.96
	Anhydrous MoO <sub>x</sub> 250 °C	15.68	0.79	0.68	8.43

A similar trend was observed in the fullerene-based solar cell using PTB7-Th:PC<sub>71</sub>BM (see **Figure 3.2d**). The solar cell with the non-annealed an-MoO<sub>x</sub> HTL showed a PCE of just 1.4% with a poor *FF* (47.9%) and a very low *J<sub>sc</sub>* (4.25 mA/cm<sup>2</sup>) together with a larger series resistance. When the an-MoO<sub>x</sub> HTL was annealed at 200 °C, however, the efficiency was recovered to 9.0% (see **Figure 3.3b** and **Table 3.2**). With the aq-MoO<sub>x</sub> HTL, the PTB7-Th:PC<sub>71</sub>BM solar cell exhibited a comparable efficiency of 8.9% even without any annealing process. The J-V curves and photovoltaic parameters of polymer solar cells based on PTB7-Th:PC<sub>71</sub>BM with aq-MoO<sub>x</sub> with various H<sub>2</sub>O concentrations were shown in **Figure 3.5** and **Table 3.3**.

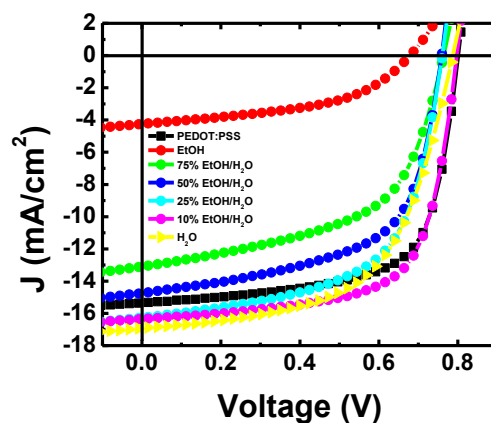


**Figure 3.5** *J-V* characteristics of the conventional polymer solar cells based on PTB7-Th:PC<sub>71</sub>BM blend films with aqueous MoO<sub>x</sub> with various H<sub>2</sub>O concentrations.

**Table 3.3** Photovoltaic performance of the conventional polymer solar cell based on PTB7-Th:PC<sub>71</sub>BM blend films with aqueous MoO<sub>x</sub> with various H<sub>2</sub>O concentrations.

Condition	$J_{sc}$ [mA/cm <sup>2</sup> ]	$V_{oc}$ [V]	FF [%]	PCE [%]
PEDOT:PSS	15.35	0.80	0.67	8.29
EtOH 100%	4.25	0.68	0.48	1.37
EtOH 75% / H <sub>2</sub> O 25%	13.10	0.76	0.55	5.51
EtOH 50% / H <sub>2</sub> O 50%	14.75	0.76	0.60	6.73
EtOH 25% / H <sub>2</sub> O 75%	16.28	0.76	0.61	7.51
EtOH 10% / H <sub>2</sub> O 90%	16.36	0.80	0.67	8.76
H <sub>2</sub> O 100%	16.92	0.79	0.58	7.74

In the evaluation of the solar cell performance, the aq-MoO<sub>x</sub> HTL clearly performed better than the PEDOT:PSS HTL. **Figure 3.6a** shows the charge extraction (CE) current, which was measured under 1-sun illumination and  $V_{oc}$  conditions. From this CE current, the CE density was deduced, as shown in **Figure 3.6b**. The CE density results were consistent with the *J-V* characteristics. In the case of the device with the PEDOT:PSS HTL, the calculated CE density was  $1.09 \times 10^{14}$  cm<sup>-2</sup>. The device with the non-annealed an-MoO<sub>x</sub> HTL showed a one order of magnitude lower CE density of  $6.93 \times 10^{13}$  cm<sup>-2</sup> than the device with the PEDOT:PSS HTL. However, similar to the *J-V* results, the CE density of the device with the an-MoO<sub>x</sub> HTL significantly increased with high temperature annealing at 200 °C. In the case of the device with

the aq-MoO<sub>x</sub> HTL, although the calculated CE density value was slightly lower than that of the device with the annealed an-MoO<sub>x</sub> HTL ( $1.35 \times 10^{14} \text{ cm}^{-2}$ ), it clearly showed a better CE density value ( $1.23 \times 10^{14} \text{ cm}^{-2}$ ) than that of the device with the PEDOT:PSS HTL.

The improved electrical properties of the aq-MoO<sub>x</sub> HTL were also observed in the impedance spectroscopy (IS) study. The Nyquist plots of the IS results measured under dark conditions are shown in **Figure 3.6c**. All of the devices exhibited one semicircle without a transmission line (TL), which indicates that all devices undergo strong recombination.<sup>[76]</sup> In general, this feature can be interpreted using the Gerischer impedance model, where the square root of the product of the recombination resistance ( $R_{\text{rec}}$ ) and transportation resistance ( $R_{\text{tr}}$ ) can be described as the Gerischer resistance ( $R_{\text{G}}$ ).<sup>[77,78]</sup> The device with the annealed an-MoO<sub>x</sub> HTL or aq-MoO<sub>x</sub> HTL exhibited a higher  $R_{\text{G}}$  (or  $R_{\text{rec}}$ , which is inversely proportional to the recombination rate) than the device with the non-annealed an-MoO<sub>x</sub> HTL or PEDOT:PSS. Since all devices have the same structure except for the MoO<sub>x</sub> layer, the difference of  $R_{\text{G}}$  definitely resulted from the charge transportation at the MoO<sub>x</sub> layer and charge recombination at the interface. A higher  $R_{\text{G}}$  corresponds to a lower recombination probability, which indicates better charge transport ability without recombination. Therefore, the IS results shown in **Figure 3.6c** clearly indicate that the charge transport properties of the aq-MoO<sub>x</sub> HTL was better than that of the PEDOT:PSS HTL.

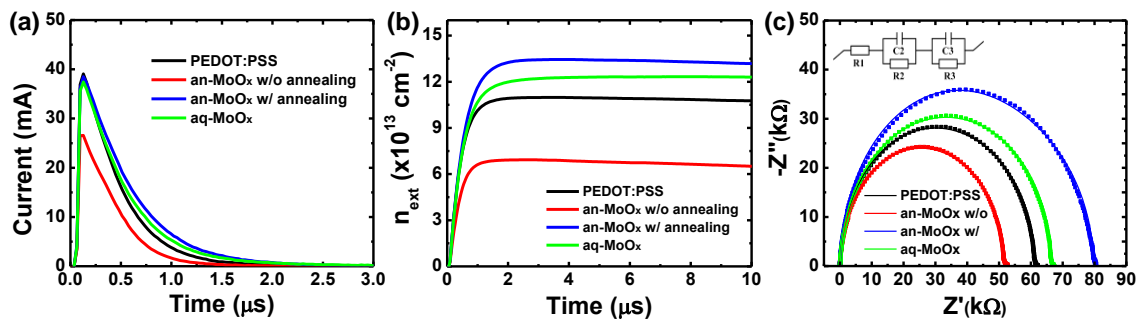


**Figure 3.6** (a) Charge extraction (CE) current transient under 1 sun illumination and  $V_{\text{oc}}$  conditions, (b) calculated charge extraction density, and (c) Nyquist plot of the impedance spectroscopy measurements of the polymer solar cells with various MoO<sub>x</sub> HTLs under dark conditions.

Normally, in metal oxide layers prepared by an anhydrous sol-gel method, high-temperature curing is conducted to remove ligands which provide solubilizing power in metal oxide nanoparticles. To explore the chemical structure differences between the an-MoO<sub>x</sub> HTL and aq-MoO<sub>x</sub> HTL, Fourier transform infra-red (FTIR) spectroscopy was performed, as shown in

**Figure 3.7.** The non-annealed an-MoO<sub>x</sub> layer showed clear evidence of the characteristic peaks of acetylacetonate in the fingerprint region including a C=C stretch at 1,573 cm<sup>-1</sup>, C=O stretch at 1,530 cm<sup>-1</sup>, C=O stretch + C-H bending at 1,422 cm<sup>-1</sup>, CH<sub>3</sub> symmetrical bending at 1,354 cm<sup>-1</sup>, C=C stretch + C-CH<sub>3</sub> stretch at 1,280 cm<sup>-1</sup>, and CH<sub>3</sub> rocking at 1,029 cm<sup>-1</sup>.<sup>[79-81]</sup> In addition, the non-annealed an-MoO<sub>x</sub> layer also exhibited a broad peak at 3,300 cm<sup>-1</sup>, which is attributed to the O-H stretch vibration of ethanol, and two C-H stretch peaks near 2,980 cm<sup>-1</sup>, which are attributed to acetylacetonate (**Figure 3.4b**).<sup>[82]</sup> However, in the an-MoO<sub>x</sub> layer cured at 200 °C, all carbon related peaks disappeared, which indicates that acetylacetonate ligands were successfully removed by the curing process. The chemical structure change of the an-MoO<sub>x</sub> layer as a function of the curing temperature is presented in **Figure 3.8**. The removal of acetylacetonate peaks from the an-MoO<sub>x</sub> layer was only completed at 200 °C, which is good agreement with previous literatures.<sup>[4,72]</sup> For the aq-MoO<sub>x</sub> layer, however, the acetylacetonate peaks almost vanished in the FTIR spectra even without a curing process. The aq-MoO<sub>x</sub> layer showed a bending and stretching vibrations of H<sub>2</sub>O at 1,620 cm<sup>-1</sup> and 3,300 cm<sup>-1</sup>, respectively. Therefore, it can be concluded that all of the acetylacetonate ligands were already removed from the solution state by the hydrolysis effect resulting from the added water. The FTIR spectra of the aq-MoO<sub>x</sub> layer as a function of the curing temperature is shown in **Figure 3.9**. With increasing curing temperature, only water peaks were removed. However, the presence of water does not seem to significantly influence the performance of the solar cells (**Figure 3.2d**).

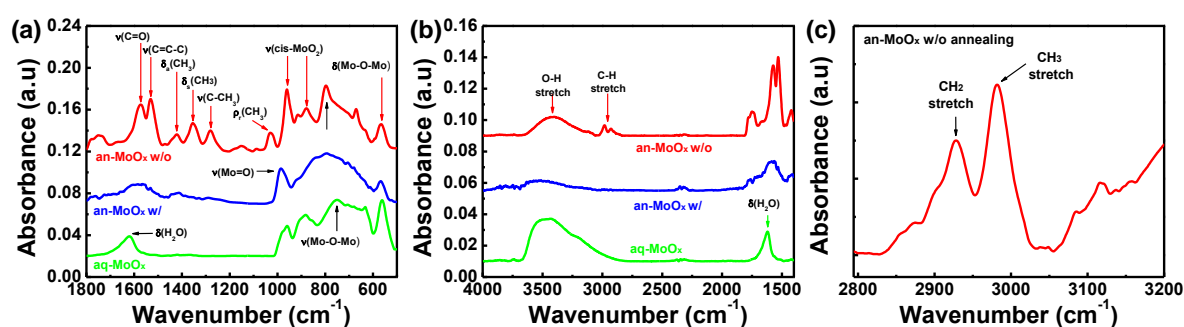


**Figure 3.7** Fourier transform infra-red (FTIR) spectroscopy of MoO<sub>x</sub> HTLs: (a) fingerprint region, (b) function group region, and (c) CH<sub>2</sub> and CH<sub>3</sub> stretch mode vibration peaks of non-annealed an-MoO<sub>x</sub> films.



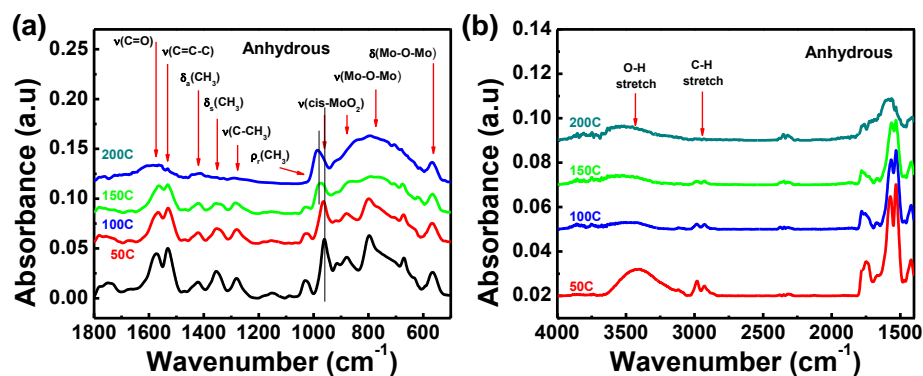


**Figure 3.8** FTIR spectra obtained from anhydrous MoO<sub>x</sub> layers annealed at various temperatures.

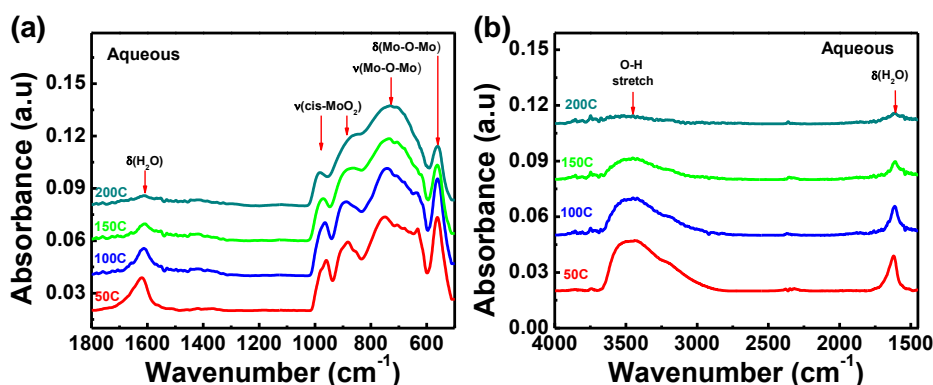


**Figure 3.9** FTIR spectra obtained from aqueous MoO<sub>x</sub> layers annealed at various temperatures.

The non-annealed an-MoO<sub>x</sub> exhibited peaks at 960 cm<sup>-1</sup>, 880 cm<sup>-1</sup>, 800 cm<sup>-1</sup>, and 564 cm<sup>-1</sup>. The peak at 800 cm<sup>-1</sup> was characterized as the C-H out-of-plane bending mode originating from acetylacetonate. The doublet peak at 960 cm<sup>-1</sup> and 880 cm<sup>-1</sup> was characterized as the stretching mode of cis-MoO<sub>2</sub>, O=Mo=O, while the peak at 564 cm<sup>-1</sup> was identified as the bending mode of Mo-O-Mo.<sup>[83,84]</sup> The peak in the range of 850 cm<sup>-1</sup> to 600 cm<sup>-1</sup> was identified as the stretching mode of Mo-O-Mo.<sup>[72,79,85]</sup> In addition, only non-annealed an-MoO<sub>x</sub> exhibited the CH<sub>2</sub> stretching mode at 2,927 cm<sup>-1</sup> (**Figure 3.7c**), which indicates the possibility of interaction between ethanol and MoO<sub>2</sub>(acac)<sub>2</sub>. Based on all of the FTIR results, it can be concluded that the non-annealed an-MoO<sub>x</sub> film could be described as Mo<sub>2</sub>O<sub>5</sub>(acac)<sub>2</sub>(EtOH)<sub>2</sub>.<sup>[83]</sup> In the an-MoO<sub>x</sub> film annealed at high temperature, the C-H out-of-plane bending mode peak at 800 cm<sup>-1</sup> disappeared due to the decomposition of the acetylacetonate ligand. Furthermore, the cis-MoO<sub>2</sub> peak at 880 cm<sup>-1</sup> disappeared and the peak at 960 cm<sup>-1</sup> was slightly shifted to 985 cm<sup>-1</sup>, which is attributed to Mo=O stretching. In addition, the CH<sub>2</sub> stretching mode peak also disappeared. All of these phenomena observed after high-temperature annealing can be interpreted as the

process of conversion from the cis-MoO<sub>2</sub> form with ligands to a form close to MoO<sub>3</sub>.<sup>[86]</sup> For the aq-MoO<sub>x</sub>, the overall features of the spectrum in the 1,100-500 cm<sup>-1</sup> region were similar to annealed an-MoO<sub>x</sub>. No C-H related peaks were observed. The broad peak at 880 cm<sup>-1</sup> in aq-MoO<sub>x</sub> was interpreted as a MoO<sub>3</sub>(H<sub>2</sub>O)<sub>x</sub> stretching mode. The IR spectrum of aq-MoO<sub>x</sub> showed a similar feature of molybdenum trioxide hydrates.<sup>[83,86,87]</sup> Although the intermediate hydrate Mo<sub>2</sub>O<sub>5</sub>(acac)<sub>2</sub>(H<sub>2</sub>O)<sub>2</sub> state was not observed in our study, the overall FTIR results clearly indicate that MoO<sub>2</sub>(acac)<sub>2</sub> was successfully converted to (MoO<sub>3</sub>)<sub>n</sub>(H<sub>2</sub>O)<sub>2n+1</sub> without high temperature curing due to hydrolysis with added water.

X-ray photoelectron spectroscopy (XPS) analysis was carried out to more clearly elucidate the state of the Mo atoms. **Figures 3.10a** and **3.10b** show the XPS spectra of the Mo 3d and O 1s peaks, respectively. For the Mo 3d peaks, by using the Gaussian fitting method, the two Mo 3d peaks were divided into two doublets originating from the spin-orbital splitting. The major doublet (higher intensity) at 232.8 eV and 236.02 eV belonged to the Mo<sup>6+</sup> oxidation state, while the minor doublet (lower intensity) at 231.7 eV and 234.5 eV belonged to the Mo<sup>5+</sup> oxidation state.<sup>[4]</sup> The atomic concentration ratio of Mo<sup>6+</sup>/Mo<sup>5+</sup> was determined from the proportion of the integrated peak area of each component. The Mo<sup>6+</sup>/Mo<sup>5+</sup> ratios were 3.86 and 4.59 for an-MoO<sub>x</sub> without annealing and aq-MoO<sub>x</sub>, respectively. For an-MoO<sub>x</sub> with annealing, the Mo<sup>6+</sup>/Mo<sup>5+</sup> ratio was 5.13. The O 1s peak was analyzed as two peaks by Gaussian fitting. The lower binding energy peak (oxygen-LBE) at 530.7 eV is assigned to bonding with the Mo atom, while the higher binding energy peak (oxygen-HBE) at 531.7 eV is attributed to the oxygen associated with the acetylacetonate ligand.<sup>[72]</sup> The oxygen-HBE/oxygen-LBE ratios were 1.28, 0.41, and 0.94 for an-MoO<sub>x</sub> without annealing, an-MoO<sub>x</sub> with annealing, and aq-MoO<sub>x</sub>, respectively.

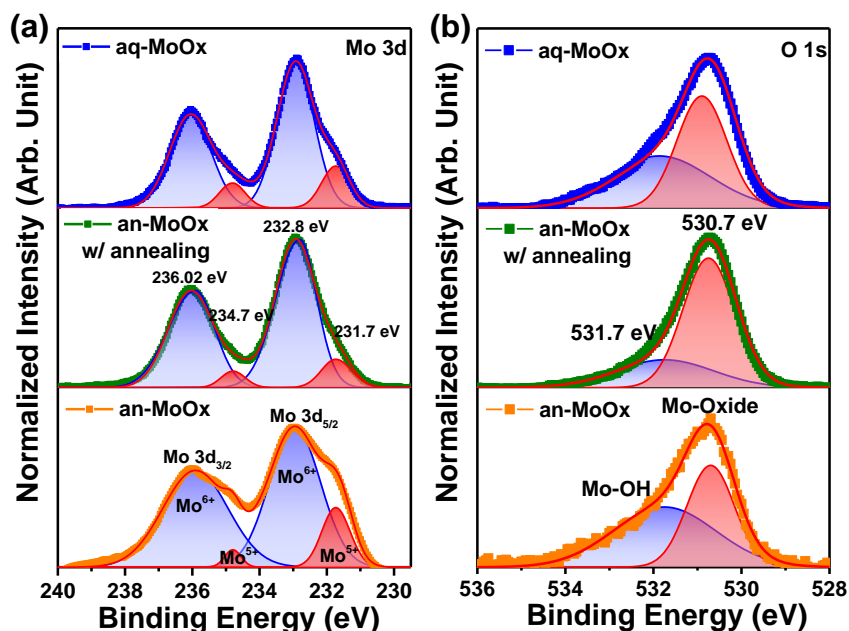


**Figure 3.10** XPS spectra of (a) Mo 3d and (b) O 1s core level peaks obtained from the MoO<sub>x</sub> layers.

Among the three MoO<sub>x</sub> HTLs, the annealed an-MoO<sub>x</sub> showed a higher Mo<sup>6+</sup>/Mo<sup>5+</sup> ratio and lower oxygen-HBE/oxygen-LBE ratio compared to an-MoO<sub>x</sub> without annealing, which means that the Mo<sup>6+</sup> fraction and oxygen-LBE fraction were enhanced after high-temperature annealing. These results clearly indicate that Mo<sup>5+</sup> was further oxidized to Mo<sup>6+</sup> due to decomposition of the acetylacetonate ligand.<sup>[88]</sup> A similar trend was observed in the comparison between annealed an-MoO<sub>x</sub> and aq-MoO<sub>x</sub>. The aq-MoO<sub>x</sub> showed a higher Mo<sup>6+</sup>/Mo<sup>5+</sup> ratio and lower oxygen-HBE/oxygen-LBE ratio compared to an-MoO<sub>x</sub> without annealing. Therefore, we can conclude that water removed the acetylacetonate ligand from MoO<sub>2</sub>(acac)<sub>2</sub> and oxidized Mo atoms to the highest oxidation state of Mo<sup>6+</sup>. Interestingly, the Mo:O stoichiometry of all MoO<sub>x</sub> layers was below than 1:3, which indicates that all MoO<sub>x</sub> layers were sub-stoichiometric. This is the reason why we used MoO<sub>x</sub> instead of MoO<sub>3</sub>. The Mo:O stoichiometry is listed in **Table 3.4**. Consequently, we clearly confirmed that the acetylacetonate ligand can be removed not only by high-temperature curing but also by the hydrolysis process of water. Based on the results of the FTIR and XPS studies, the expected chemical structures of the an-MoO<sub>x</sub> and aq-MoO<sub>x</sub> precursor solutions are illustrated in **Figure 3.11**.

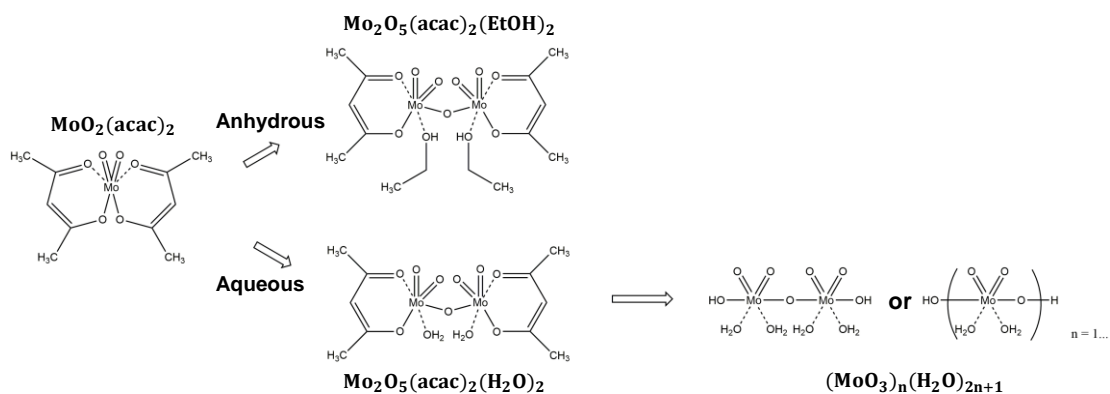


**Figure 3.11** Schematic illustration of the expected chemical structures of the an-MoO<sub>x</sub> and aq-MoO<sub>x</sub> precursor solutions.

**Table 3.4** The Mo<sup>6+</sup>/Mo<sup>5+</sup>, Oxygen-HBE/Oxygen-LBE, and O atom/Mo atom ratios calculated from the XPS data.

	Mo <sup>6+</sup> / Mo <sup>5+</sup>	Oxygen-HBE/Oxygen-LBE	Mo:O
Anhydrous MoO <sub>x</sub>	3.86	1.28	1:2.80
Anhydrous MoO <sub>x</sub> 200°C	5.13	0.41	1:2.99
Aqueous MoO <sub>x</sub>	4.59	0.94	1:2.93

To investigate the band structure difference between an-MoO<sub>x</sub> and aq-MoO<sub>x</sub>, Ultraviolet Photoelectron Spectroscopy (UPS) analysis was conducted, as shown in **Figure 3.12**. The summary of the UPS analysis is illustrated in **Figure 3.13** as band diagrams. The Fermi energy (E<sub>F</sub>) was calculated from the ITO surface and all other spectra are plotted with respect to this value. The calculated E<sub>F</sub> values were 4.74 eV and 5.14 eV for ITO and PEDOT:PSS, respectively. The vacuum levels (VLs) were determined by linear extrapolation of the secondary electron cutoffs on the high binding energy side. The valence band (VB) maximum was extracted from the onset on the low binding energy side. The relative position of the VB maximum level was determined by comparing the shift of the onset to the E<sub>F</sub> of ITO. The conduction band (CB) minimum level was estimated using the extracted VB maximum and the measured optical gaps extracted from the UV-Vis absorption spectra. All MoO<sub>x</sub> layers exhibited an optical band gap of 3.22 eV, which are in agreement with the literature data.<sup>[89]</sup> The work function (WF) of the non-annealed an-MoO<sub>x</sub> HTL was 4.74 eV, which is comparable to that of the ITO substrate. The WF of the an-MoO<sub>x</sub> HTL with annealing was enlarged due to the VL shift of 0.39 eV. In the case of aq-MoO<sub>x</sub>, the measured WF was 4.92 eV. A similar trend was

observed for the calculated hole injection barrier ( $\phi_h$ ). The deduced  $\phi_h$  values were 0.74 eV, 0.49 eV, and 0.60 eV for the non-annealed an-MoO<sub>x</sub> HTL, an-MoO<sub>x</sub> HTL with annealing, and aq-MoO<sub>x</sub>, respectively. The an-MoO<sub>x</sub> HTL with annealing showed more favorable energy level alignment for hole transport. The  $\phi_h$  value of aq-MoO<sub>x</sub> was slightly higher than that of the annealed an-MoO<sub>x</sub> HTL. This energy level difference played an important role in the performance of the polymer solar cell. All of the solar cell results were consistent with this  $\phi_h$  difference. Of course, the energy level alignment of aq-MoO<sub>x</sub> was not the best, but it is worth noting that a significant improvement was achieved without high temperature curing. To get more insight into the charge transport property at the interface between HTLs and active layer, we have measured hole mobilities using hole-only devices with structure ITO/HTLs/active layer/evaporated MoO<sub>x</sub>/Ag. The active layer thickness was 150 nm and the active layer permittivity was 3.5, as previously stated in literature.<sup>[90]</sup> The hole mobilities of various hole transport layers (HTLs)/active layer were determined by the steady-state space-charge-limited current (SCLC) method. The SCLC region and hole mobility of various HTLs/active layer were shown in **Figure 3.14** and **Table 3.5**, respectively. The hole mobility of PEDOT:PSS/PBDB-T-2F:Y6 was similar to other studies reported in literature.<sup>[73]</sup> The distinguishable difference in the hole mobility of an-MoO<sub>x</sub> with and without annealing showed a clear effect of high temperature annealing in the removal of the organic ligand. Furthermore, the hole mobility of aq-MoO<sub>x</sub> was higher than that of PEDOT:PSS. Overall, the hole mobility data in **Table 3.5** is consistent with the J-V curves of polymer solar cells.

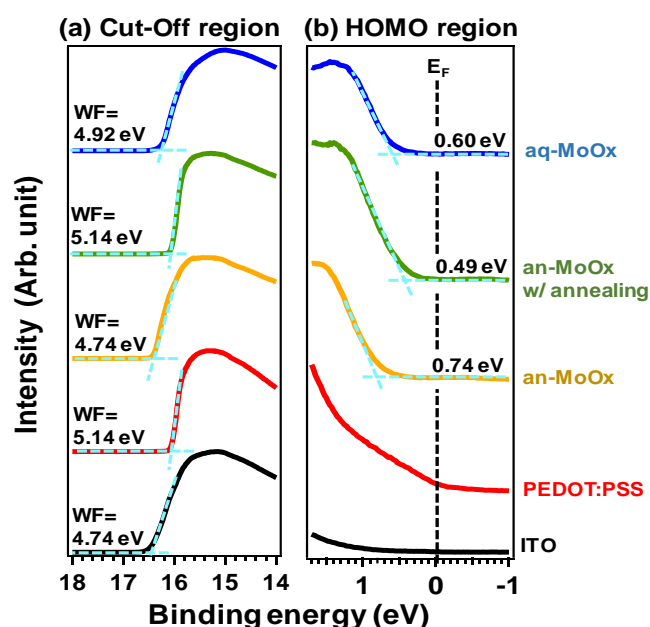


**Figure 3.12** UPS spectra of MoO<sub>x</sub> layers.

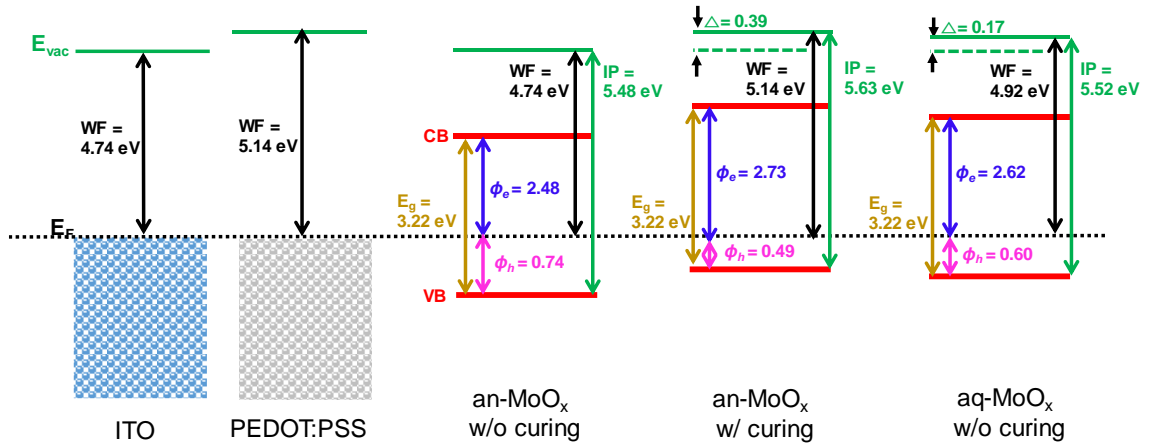


**Figure 3.13** Energy band diagrams of aq-MoO<sub>x</sub> and an-MoO<sub>x</sub> with and without annealing layers obtained from UPS measurements.

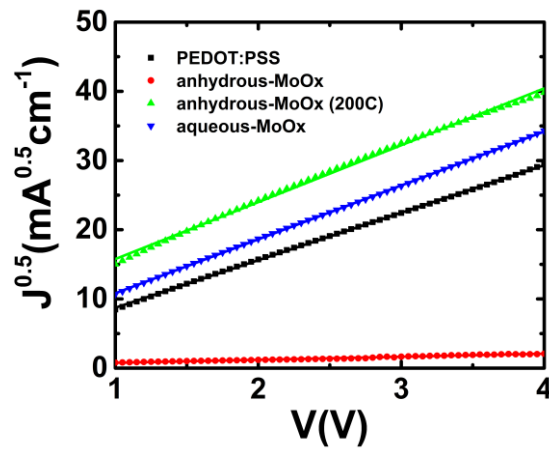


**Figure 3.14** Hole mobilities of OPVs based on PBDB-T-2F:Y6 blend films with various hole transport layers as PEDOT:PSS, anhydrous MoO<sub>x</sub> and aqueous MoO<sub>x</sub>. The hole-only devices configuration is ITO/HTL/PBDB-T-2F:Y6/evaporated MoO<sub>x</sub>/Ag.

**Table 3.5** Hole mobilities of OPVs based on PBDB-T-2F:Y6 blend films with various hole transport layers as PEDOT:PSS, anhydrous MoO<sub>x</sub> and aqueous MoO<sub>x</sub>.

Condition	Slope	$\mu_h$ (cm <sup>2</sup> · V <sup>-1</sup> · s <sup>-1</sup> )
PEDOT:PSS/PBDB-T-2F:Y6	6.87	4.57x10 <sup>-4</sup>
Anhydrous MoO <sub>x</sub> /PBDB-T-2F:Y6	0.44	1.87x10 <sup>-6</sup>
Anhydrous MoO <sub>x</sub> (200 °C)/PBDB-T-2F:Y6	8.22	6.54x10 <sup>-4</sup>
Aqueous MoO <sub>x</sub> /PBDB-T-2F:Y6	7.79	5.87 x10 <sup>-4</sup>



In addition to the energy level alignment, morphology changes can also influence the charge transport properties. However, a significant surface morphology change was not detected in the atomic force microscope (AFM) measurements (see **Figure 3.15**). Furthermore, the morphology of PBDB-T-2F:Y6 casted on various hole transport layers was also examined (see **Figure 3.16**). As shown in **Figure 3.16**, all AFM images showed similar fibril network morphology. Therefore, we concluded that the difference of the performance of the solar cell was not due to a morphology change at the interface between the MoO<sub>x</sub> HTL and active layer.

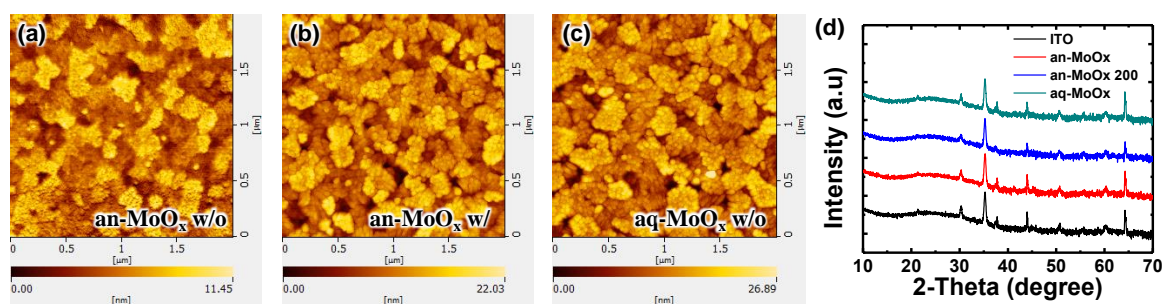


**Figure 3.15** Atomic Force Microscope (AFM) images of (a) an-MoO<sub>x</sub> without annealing, (b) an-MoO<sub>x</sub> with annealing at 200 °C, and (c) aq-MoO<sub>x</sub> without annealing, and (d) XRD results.

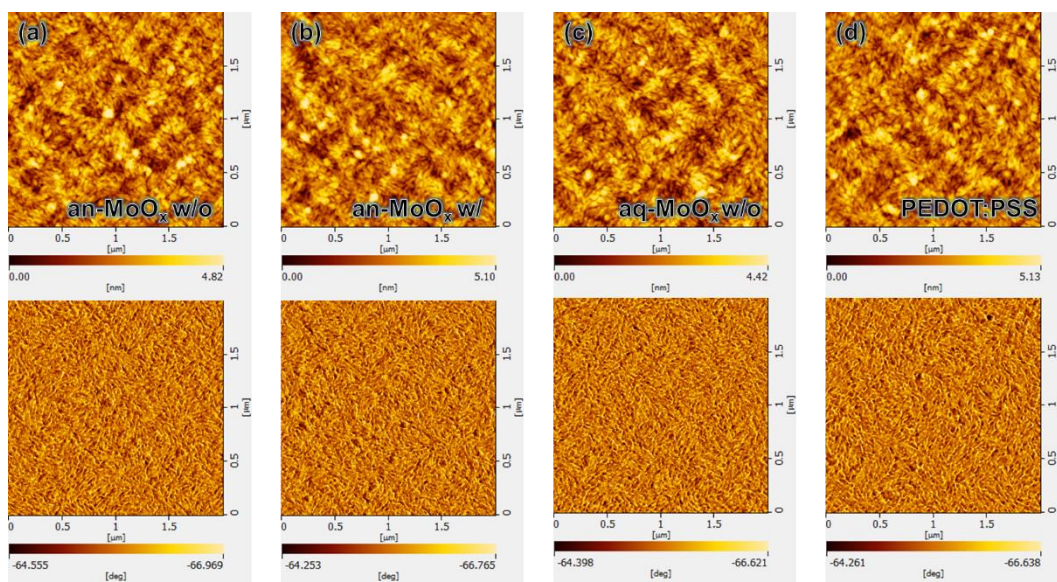


**Figure 3.16** Atomic Force Microscope (AFM) topography images (top) and phase image (bottom) of PBDB-T-2F:Y6 active layer casted on (a) an-MoO<sub>x</sub> without annealing, (b) an-MoO<sub>x</sub> with annealing at 200 °C, (c) aq-MoO<sub>x</sub> without annealing, and (d) PEDOT:PSS.

Since the aq-MoO<sub>x</sub> HTL does not require an annealing process, the water added during the sol-gel process remains in the film (**Figure 3.7**). Of course, it is expected to be in a weakly bonded form, but it is doubtful that the remaining water will affect the stability of the device.

To confirm this point, we evaluated the operation stability for the PBDB-T-2F:Y6 non-fullerene solar cells. This stability test was conducted in air without any encapsulation. **Figure 3.17** shows the changes of  $J_{sc}$ ,  $V_{oc}$ ,  $FF$ , and PCE measured continuously over 25 hours with various HTLs as PEDOT:PSS, aq-MoO<sub>x</sub> without annealing, and aq-MoO<sub>x</sub> annealed at 150C. Because of well-known weak stability of non-fullerene solar cells based on Y6, both solar cell with the PEDOT:PSS and solar cell with MoO<sub>x</sub> HTL showed continuous decreases of PCE from the beginning.<sup>[91]</sup> However, after 25 hours of operation, the solar cell with aq-MoO<sub>x</sub> showed better condition compared to the solar cell with PEDOT:PSS.

Storage stability performed for PTB7-Th:PC<sub>71</sub>BM solar cells also showed similar trend (**Figure 3.18**). The PTB7-Th:PC<sub>71</sub>BM solar cell with the PEDOT:PSS HTL showed continuous decreases of  $J_{sc}$  and  $FF$  from the beginning. After 1,000 hours, the PCE significantly decreased from 8.43% to 4.9%. In the case of the solar cell with the aq-MoO<sub>x</sub> HTL, however, all of the solar cell parameters were well maintained compared to the solar cell with PEDOT:PSS. The PCE decreased by only 9% from 8.81% to 8.01%. Therefore, it can be concluded that the aq-MoO<sub>x</sub> HTL does not significantly affect the stability even if it contains water in the film.<sup>[92]</sup>

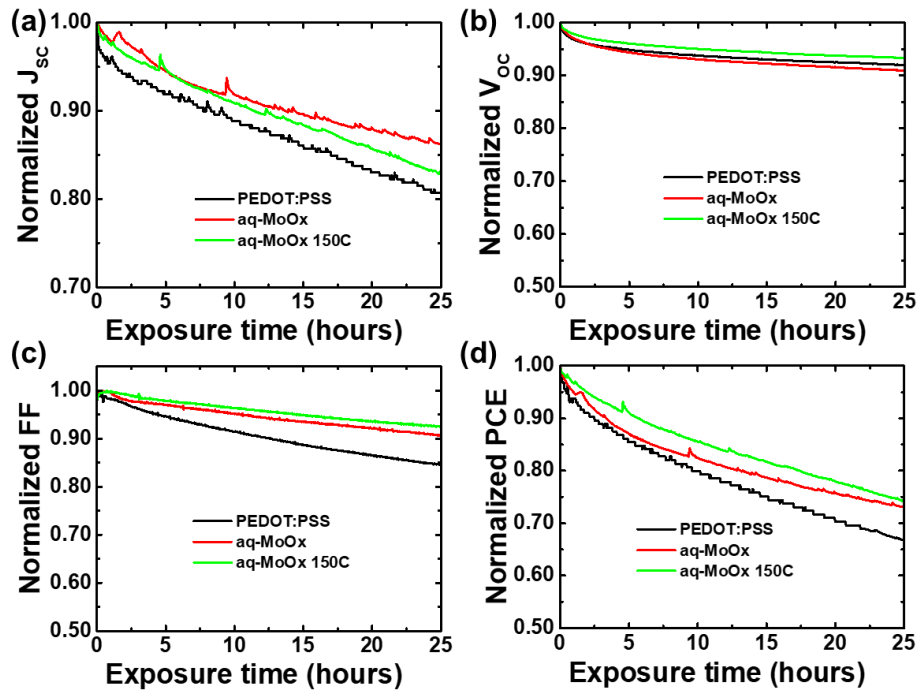


**Figure 3.17** Changes of (a)  $J_{sc}$ , (b)  $V_{oc}$ , (c)  $FF$ , and (d) PCE of non-fullerene solar cell based on PBDB-T-2F:Y6 during continuous operation in air without any encapsulation.



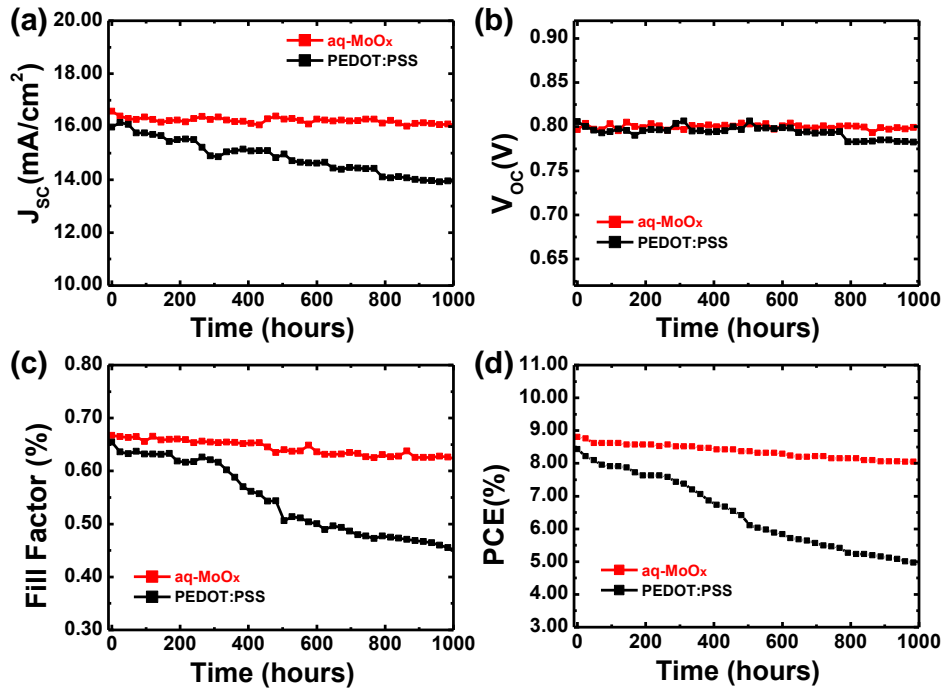


**Figure 3.18** Storage stability performed for PTB7-Th:PC<sub>71</sub>BM solar cells.

The most notable advantage of annealing-free aq-MoO<sub>x</sub> is that it allows the fabrication of an inverted solar cell employing only a solution process. Some organic photoactive materials become significantly degraded with high temperature annealing including PTB7-Th:PC<sub>71</sub>BM and PBDTTPD-HT:IDIC combinations. The PTB7-Th and PC<sub>71</sub>BM active layer allows only a maximum temperature of 80 °C. Thus, in most cases, PTB7-Th and PC<sub>71</sub>BM solar cells were fabricated with room temperature drying by keeping them in a glove box for 2-3 hours. The PBDTTPD-HT:IDIC active layer is similar as it also allows only a maximum of 100 °C annealing after active layer deposition. Therefore, the fabrication of inverted solar cells was not possible using general solution-processable HTL materials which require high-temperature curing over 150 °C. In most cases, a vacuum deposition method was utilized for the HTL construction. The use of PEDOT:PSS was also limited in the fabrication of inverted solar cells because PEDOT:PSS also needed to be dried at a temperature of at least 100 °C. However, with our aq-MoO<sub>x</sub> HTL, active layer degradation by high temperature annealing is no longer a serious problem. **Figure 3.19** shows the J-V characteristics of the PTB7-Th:PC<sub>71</sub>BM and PBDTTPD-HT:IDIC solar cell fabricated with an inverted structure. The HTLs were deposited on active layer in N<sub>2</sub> or in air. In both PTB7-Th:PC<sub>71</sub>BM and PBDTTPD-HT:IDIC active layer combinations, the solar cells with aq-MoO<sub>x</sub> showed slightly better performance compared to the solar cell with the PEDOT:PSS HTL. Somewhat lower performance compared to the solar

cell with the conventional structure was obtained because of the adsorption property. Since aq-MoO<sub>x</sub> is based on a hydrophilic solvent, it is somewhat difficult to deposit it on a hydrophobic organic photoactive layer by spin-coating. Therefore, to enhance the adsorption property, we added 2 mg/ml of Triton X-100 into the PEDOT:PSS and aq-MoO<sub>x</sub> solution.<sup>[93,94]</sup> This performance decrease was most likely caused by adding Triton X-100.

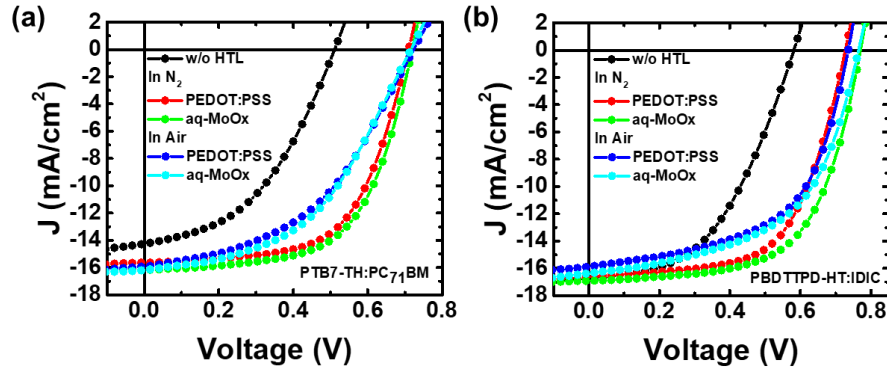


**Figure 3.19** (a) *J-V* characteristics of the inverted polymer solar cells based on PTB7-Th:PC<sub>71</sub>BM and the (b) *J-V* characteristics of polymer solar cell based on PBDTTPD-HT:IDIC. The hole transport layers were deposited on active layer in N<sub>2</sub> or air. To obtain better adsorption with an organic active layer, 2 mg/ml of Triton X-100 was added into the PEDOT:PSS and aq-MoO<sub>x</sub> solution.

### 3.4 Conclusion

In summary, we developed annealing-free solution-processable aqueous MoO<sub>x</sub> and applied it in a BHJ polymer solar cell based on a blend of PBDB-T-2F:Y6 and PTB7-Th:PC<sub>71</sub>BM. In general, the charge transport layer based on molybdenum oxides prepared by an anhydrous sol-gel method normally requires high-temperature annealing in air to achieve desired quality. As a result, the non-fullerene solar cell with the general an-MoO<sub>x</sub> HTL prepared by the sol-gel method showed a poor efficiency of 7.7% without annealing. This poor efficiency was recovered to the normal value typically observed in PBDB-T-2F:Y6 solar cells when this an-MoO<sub>x</sub> layer was annealed at 200 °C. However, the solar cell with aq-MoO<sub>x</sub> prepared by the aqueous sol-gel method showed almost comparable performance to the solar cell with the annealed an-MoO<sub>x</sub> HTL, even without high-temperature annealing. Moreover, the solar cell with aq-MoO<sub>x</sub> exhibited a higher efficiency and better stability without high-temperature annealing compared to the solar cells with PEDOT:PSS. A similar trend was observed in the fullerene-based solar cell based on PTB7-Th:PC<sub>71</sub>BM. In addition, annealing-free aq-MoO<sub>x</sub> allowed the successful fabrication of inverted PTB7-Th:PC<sub>71</sub>BM solar cell which was

impossible to fabricate using a general anhydrous  $\text{MoO}_x$  HTL which requires a high-temperature annealing process. Although high-temperature annealing is not a difficult process in laboratory scale production, it is definitely not a simple process to apply in roll-to-roll processes because of the inevitable long cooling step that follows. Thus, our aqueous method based on the hydrolysis effect can be an essential technique for large-scale roll-to-roll mass production of flexible devices.

## Chapter 4. Inverted polymer solar cells with annealing-free solution-processable NiO

*This chapter is reproduced in part with permission of “Small, sml.202101729”. Copyright 2021 Wiley-VCH GmbH.*

### 4.1 Research Background

Polymer solar cells (PSCs) occupy an important position in the expected future of mobile energy strategies due to their advantages of physical flexibility, light weight, ease of fabrication, and low manufacturing cost.<sup>[48–50,52,95]</sup> The most important requirements for commercialization of PSCs are high power conversion efficiency (PCE) and stability. Although PSC efficiency greater than 18% has been demonstrated by introducing non-fullerene acceptors such as Y6 and its derivatives, low stability under real working conditions remains a major obstacle.<sup>[91]</sup> According to studies of stability related to the structure of PSCs, it is known that cells of inverted structure exhibit better stability than those of conventional structure.<sup>[96]</sup> In addition, the Ag electrode used in inverted solar cells has better processability than the Al electrode used in conventionally structured cells, so the inverse structure is preferred for mass production based on roll-to-roll processing. Because the work function (WF) of Al is lower than that of Ag, an inverted device with Ag will undergo less oxidation and thus remain more stable.<sup>[97]</sup>

In the construction of inverted-structure solar cells, more attention should be paid to selection of the hole transport layer (HTL) deposited on the photoactive layer. PEDOT:PSS is the most widely used hole transport material in conventionally structured PSCs but is not preferred for inverted solar cells because of its hydrophilicity. PEDOT:PSS is applied as a suspended solution in water, hindering spin coating onto a hydrophobic photoactive surface. Although this wettability problem can be overcome by adding Triton X-100, methanol, or ethanol, the acidity of PEDOT:PSS remains a problem. To avoid these problems, hole transport materials based on metal oxides such as MoO<sub>3</sub>, V<sub>2</sub>O<sub>5</sub>, and NiO have been applied instead of PEDOT:PSS. MoO<sub>3</sub> HTLs are normally deposited by thermal evaporation. Although thermally evaporated MoO<sub>3</sub> layers exhibit excellent hole transport, this deposition method is not well suited to future roll-to-roll-based mass production. Moreover, solution-processable MoO<sub>3</sub> also has a wettability problem, requiring use of solvent additives such as Triton X-100 to improve wetting;<sup>[98]</sup> such additives often hinder hole transport, worsening device efficiency. V<sub>2</sub>O<sub>5</sub> can be prepared using the solution-processable precursor vanadium oxytriisopropoxide (ViPr), but

this is a highly toxic compound.<sup>[92]</sup> Also, the resulting V<sub>2</sub>O<sub>5</sub> layer must be kept in air for a long time to induce hydrolysis, which can cause serious degradation to the active layer.<sup>[99]</sup>

As an alternative metal oxide hole transport material, nickel oxide (NiO) has been applied in conventionally structured PSCs. NiO is an intrinsic p-type metal oxide semiconductor with a wide band gap, which gives it both electron blocking properties and high hole-transporting properties together with good thermal and chemical stability.<sup>[100]</sup> NiO HTLs for PSCs can be deposited by various methods such as thermal evaporation, atomic layer deposition, e-beam evaporation, and solution processing.<sup>[10,101–103]</sup> Among these, solution processing of NiO based on either a precursor solution or a nanoparticle suspension appears favorable for low-cost application in roll-to-roll processing.<sup>[10,12]</sup> However, similar to other solution-processed metal oxides, NiO must be annealed at high temperature to obtain suitable hole transport properties, normally greater than 300 °C for NiO precursor solutions and greater than 100 °C for NiO nanoparticle suspensions.<sup>[11,12]</sup> Normal organic-based photovoltaic materials are not able to withstand high-temperature annealing at greater than 300 °C. Although the annealing temperature required for NiO nanoparticle suspensions is somewhat lower than that of NiO precursor solution,<sup>[12]</sup> NiO nanoparticle suspensions are typically prepared in deionized water, hindering deposition of NiO nanoparticles on the hydrophobic polymer active layer surface. For these reasons, all PSCs using NiO hole transport layers have been fabricated with a conventional structure.

In the present work, we demonstrate the first fabrication of inverted-structure PSCs having annealing-free NiO HTLs deposited by a solution process. To overcome the wettability problem, the typical water-only solvent was replaced with a mixed solution of DI water and isopropyl alcohol with a 2-butanol additive, allowing deposition of NiO nanoparticle suspension (s-NiO) onto the hydrophobic active layer surface by spin coating. After s-NiO deposition, the devices were simply dried inside a glovebox for 10 min without annealing. An inverted non-fullerene solar cell based on a blend of p-type polymer poly[4,8-bis(5-(2-ethylhexyl)thiophen-2-yl)benzo[1,2-b:4,5-b']dithiophene-alt-3-fluorothieno[3,4-b]thiophene-2-carboxylate] (PTB7-Th, also called PCE10) and non-fullerene acceptor 2,2'-[[4,4,9,9-tetrakis(4-hexylphenyl)-4,9-dihydro-s-indaceno[1,2-b:5,6-b']dithiophene-2,7-diyl]bis[[4-[(2-ethylhexyl)oxy]-5,2thiophenediyl]methylidene(5,6-difluoro-3-oxo-1H-indene-2,1(3H)-diylidene)]]bis[propanedinitrile] (IEICO-4F) exhibited the high efficiency of 11.23% with an s-NiO HTL, an efficiency comparable to that of an inverted solar cell having a MoO<sub>x</sub> hole transport layer deposited by thermal evaporation. Furthermore, conventionally structured

devices including our s-NiO layer showed efficiency comparable to that of a conventional device having a PEDOT:PSS hole transport layer.

## **4.2 Experimental**

### **4.2.1 Preparation of the NiO nanoparticle (NiO NP) solution**

The 0.5 mol L<sup>-1</sup> nickel nitrate hexahydrate [Ni(NO<sub>3</sub>)<sub>2</sub>·6H<sub>2</sub>O] solution was prepared by adding Ni(NO<sub>3</sub>)<sub>2</sub>·6H<sub>2</sub>O into ethanol and stirring at room temperature to obtain a clear green solution. Next, the solution was adjusted to pH 10 by dropwise addition of 5 mol L<sup>-1</sup> sodium hydroxide (NaOH) solution. At this stage, Ni(OH)<sub>2</sub> precipitate formed and was filtered and rinsed with ethanol until the sodium nitrate (NaNO<sub>3</sub>) was completely removed. The precipitate was dried at 110 °C overnight to remove the organic solvent to obtain the Ni(OH)<sub>2</sub> powder. The Ni(OH)<sub>2</sub> powder was calcined at 270 °C for 2 h, yielding NiO NPs as a black powder. The NiO NP solution (s-NiO) (10 mg mL<sup>-1</sup>) was prepared by adding NiO NP powder into aqueous isopropyl propanol (70% IPA and 30% DI water). To improve coating properties and eliminate the coffee ring effect, 100 µL of 2-butanol was added into the NiO NP solution.

### **4.2.2 Device Fabrication**

Conventional bulk heterojunction polymer solar cells were fabricated using an ITO/s-NiO/PTB7-Th:IEICO-4F/ZnO/Al structure. The patterned indium tin oxide (ITO) substrates were subjected to ultrasonication in deionized water, acetone, and isopropyl alcohol, in sequence. They were dried in an oven at 100 °C for several hours. Once dried, the substrates were treated with UV for 60 min to increase their hydrophilicity. NiO film was coated onto the cleaned ITO using a two-step spin coating process: coating at 2000 rpm for 30 s and drying at 9000 rpm for 30 s to remove residual alcoholic solvent without application of heat. The NiO film was allowed to stand in air at room temperature for 30 min for complete drying. Then, the NiO film was placed into an N<sub>2</sub>-filled glovebox to allow deposition of the solar cell active layer. A blended solution of PTB7-Th and IEICO-4F (1:1.5 by weight) was prepared by dissolving in chlorobenzene with 4% CN as an additive to improve phase separation. The solution was stirred for 1 day before use. For the PTB7-Th:IEICO-4F blend solution, a two-step spin coating process was used to deposit the polymer active layer onto the NiO layer. The blended solution was passed through a 0.45 µm PTFE syringe filter and then spin coated onto the NiO layer at 1400 rpm, followed by spinning at 9000 rpm to remove residual CN additive. A ZnO nanoparticle solution (2.5 wt% in IPA) was further diluted in IPA at a ratio of 1:5 and then spin-coated on top of the active layer at 5000 rpm. The devices were allowed to dry in a glovebox for 30 min

at room temperature and placed in an evaporation chamber. Next, 100 nm of Al was deposited under high vacuum less than  $10^{-6}$  Torr. The active surface area of the device, as defined by a metal shadow mask, was  $0.13 \text{ cm}^2$ . For the reference device, PEDOT:PSS (CLEVIOS PH1000), which substituted for the NiO layer, was spin-coated on top of the ITO substrate at 5000 rpm and annealed at  $150 \text{ }^\circ\text{C}$  in air.

Inverted bulk heterojunction polymer solar cells were fabricated using an ITO/ZnO/PTB7-Th:IEICO-4F/s-NiO/Ag structure. A ZnO nanoparticle solution (2.5 wt% in IPA) was further diluted in IPA at a ratio of 1:2 and then deposited on the ITO substrate, followed by annealing at  $150 \text{ }^\circ\text{C}$  for 10 min. The ZnO film was cooled to room temperature and placed in an  $\text{N}_2$ -filled glovebox to allow deposition of the solar cell active layer. The PTB7-Th:IEICO-4F blend solution was spin-coated onto the ZnO layer at 1400 rpm, followed by spinning at 9000 rpm. Next, the NiO aqueous solution (IPA 70% with 100  $\mu\text{L}$  of 2-butanol) was spin-coated on top of the active layer at 1000 rpm for 30 s, followed by spinning at 5000 rpm for 5 s. The devices were dried inside the glovebox for 10 min without post treatment. Once dried, the devices were placed in an evaporation chamber, and 100 nm of Ag was deposited under high vacuum less than  $10^{-6}$  Torr. The active surface area of the device was  $0.13 \text{ cm}^2$ . For fabrication of a reference device, after deposition of the active layer, devices were placed in an evaporation chamber to allow deposition of 5 nm of  $\text{MoO}_3$  and 100 nm of Ag under high vacuum less than  $10^{-6}$  Torr.

#### 4.2.3 Device Characteristic

Current density–voltage curves of solar cell devices were obtained using a Keithley 2401 source measurement unit under AM1.5G simulated illumination ( $100 \text{ mW cm}^{-2}$ ). A standard Si photodiode detector with a KG-3 filter (Newport Co., Oriel) was used to calibrate the intensity of simulated sunlight. All devices were measured using a solar simulator under an inert environment inside an  $\text{N}_2$ -filled glove box. The external quantum efficiency (EQE) of the optimized solar cell performance was determined using an IQE-200B (Newport Co., Oriel). The absorption and transmittance spectra of evaporated  $\text{MoO}_x$  (e- $\text{MoO}_x$ ) and NiO (s-NiO) were measured using a UV-VIS spectrophotometer (Varian, Carry 5000). The surface morphologies of the e- $\text{MoO}_x$  layers and NiO layer were measured by AFM (Nanocute, SII NanoTechnology). The surface potentials of the PEDOT:PSS layers and NiO layer were measured using the Kelvin probe force microscopy mode of the AFM instrument. UPS and XPS were carried out with an ESCALAB 250-XI surface analysis system equipped with a He discharge lamp providing He-I photons of energy 21.22 eV for UPS and a monochromatic Al- $K\alpha$  X-ray gun of photon energy 1486.6 eV for XPS. The base vacuum pressure of the analysis system was  $\approx 10^{-7}$  Torr. The

Fermi edge was calibrated using a clean Au film, and all spectra were plotted with respect to the determined Fermi level. All XPS measurements were calibrated with reference to the Au 4f<sub>7/2</sub> core level (83.98 eV) of a freshly deposited Au film. FTIR spectroscopy was conducted using a Bruker Invenio R spectrometer. The thickness of the polymer active layer was determined using stylus profilometry (Bruker Dektak XT). The hole mobilities of various hole transport layers (HTLs; namely NiO and e-MoO<sub>x</sub>) were measured by the steady-state space-charge-limited current (SCLC) method. The structure of the hole-only device was ITO/PEDOT:PSS/PTB7-Th:IEICO-4F/HTLs/Ag. The hole mobility of active layers/HTLs was determined by the Mott–Gurney law in the SCLC trap-free regime, using the slope of  $J^{0.5}$  versus  $V$ . Impedance spectroscopy (IS) was carried out using an impedance analyzer (IVIUM tech, IviumStat) under dark conditions, measuring the optoelectronic frequency response in the frequency range of 1 MHz to 1 Hz.

### 4.3 Results and discussion

**Figure 4.1a** and **Figure 4.1b** respectively show a schematic diagram of the inverted PSC and the chemical structures of the materials used in this study. Nickel nitrate hexahydrate [Ni(NO<sub>3</sub>)<sub>2</sub>·6H<sub>2</sub>O] was used as the precursor for synthesis of NiO nanoparticles. A mixture of Ni(OH)<sub>2</sub> precipitate and NaNO<sub>3</sub> was initially formed by chemical reaction of Ni(NO<sub>3</sub>)<sub>2</sub>·6H<sub>2</sub>O and NaOH. After removal of the NaNO<sub>3</sub> by rinsing, the Ni(OH)<sub>2</sub> precipitate was thermally decomposed at 270 °C to produce NiO nanoparticle powder. According to the transmission electron microscopy (TEM) image shown at the inset of **Figure 4.1c**, the NiO nanoparticles were uniform in shape and approximately 5 nm in diameter. More details related to the preparation process of NiO nanoparticle suspension are summarized in the experimental section (see also **Figure 4.2**). Fourier transform infrared (FTIR) spectroscopy was performed to determine the chemical structure of the NiO nanoparticle powder. The Ni–O stretching mode was observed at 448 cm<sup>-1</sup>, whereas the functional group NO<sub>3</sub><sup>-</sup> was detected at 1384 cm<sup>-1</sup>, and broad peaks at 3300 and 1620 cm<sup>-1</sup> were attributed to O–H stretching vibration of ethanol and bending vibration of H<sub>2</sub>O, respectively (**Figure 4.1c**). In general, NiO thin films deposited using NiO precursors prepared by anhydrous sol–gel methods have ligands.<sup>[11]</sup> Although the ligand promotes dissolution of the NiO precursor during processing, it can disturb charge transfer in a finished device. Thus, to achieve the desired hole transport properties, the ligand must be removed in post-treatment. However, annealing at greater than 400 °C is needed to remove these ligands, as shown by FTIR absorption spectra in **Figure 4.3a** and **Figure 4.3b**.<sup>[11]</sup> Consequently, solar cells of inverted structure cannot be created with a sol-gel-based NiO



precursor solution. Contrastingly, our NiO nanoparticles have no ligand (**Figure 4.1c**), do not require annealing, and can form high-quality NiO HTLs without damage to the photoactive layer. To explore the crystallization properties of NiO nanoparticle powder, high-resolution X-ray diffraction spectroscopy (HR-XRD) was conducted, revealing that the NiO nanoparticles had a face centered cubic (fcc) structure and average grain size of 4.88 nm as calculated using the Scherrer equation (**Figure 4.3c**).<sup>[12]</sup> Overall, the average grain size calculated from XRD was consistent with the average particle size obtained from TEM observation. Figure 1d shows the energy level diagram of the inverted PSCs with NiO HTL. For the electron transport layer, a solution-processable ZnO nanoparticle suspension was used. PTB7-Th and non-fullerene acceptor IEICO-4F were used as active materials.

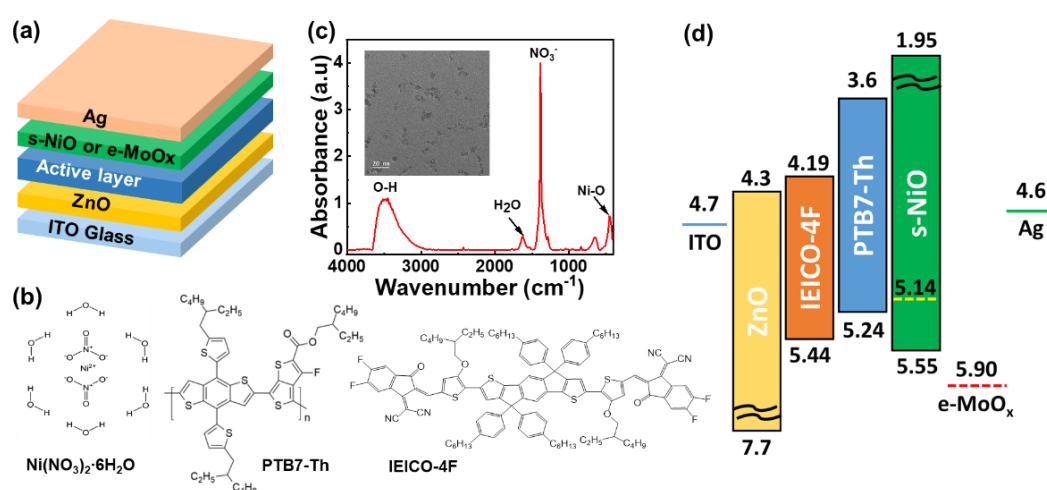


**Figure 4.1** (a) Schematic diagrams and (d) energy level diagrams of the inverted polymer solar cell. (b) Chemical structures of donor polymer material, acceptor material, and NiO precursor. (c) FTIR spectrum of NiO nanoparticle powder.

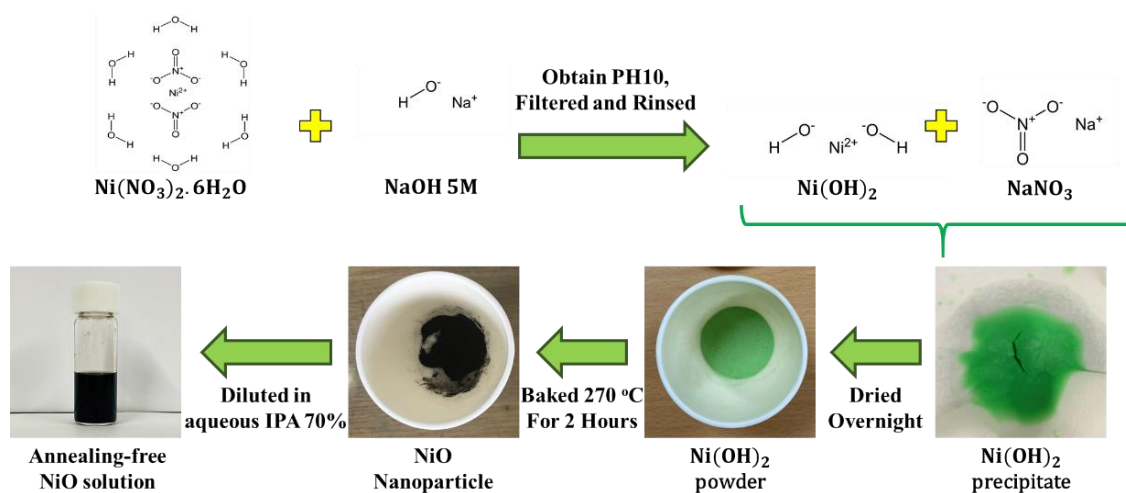


**Figure 4.2** Schematic diagram of the NiO nanoparticle synthesis procedure.

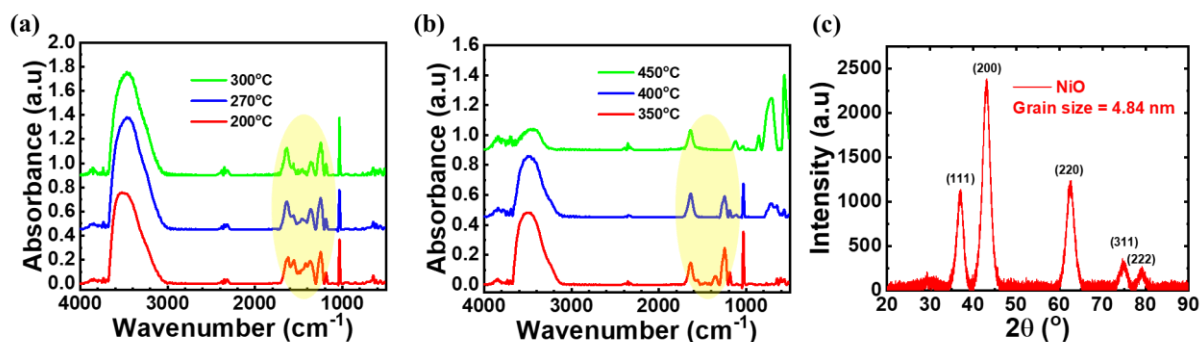


**Figure 4.3** (a) and (b) FTIR spectra of sol-gel NiO film as a function of annealing temperature ranged from 200 °C to 450 °C, (c) XRD spectra of NiO nanoparticle powder.

Although a solution-processable NiO solution was developed long ago, this solution could not be used to fabricate an inverted solar cell because of prohibited spin coating of a conventional water-based NiO solution onto a hydrophobic active layer. This wettability problem typically produces numerous pinholes in the deposited HTL layer. Unlike the case for the conventional structure, these pinholes in an inverted PSC can undesirably be filled with metal electrode material during deposition of the top electrode. These metal-filled pinholes can act as unplanned charge transport pathways of opposing charges, worsening photovoltaic performance considerably. To improve wettability, the typical solvent of DI water was initially replaced with a mixed solution of DI water (30%) and isopropyl alcohol (IPA, 70%). However, even this aqueous IPA solution failed to produce a clear and uniform film on top of the active layer, as shown in **Figure 4.4c**. Note that increasing the IPA content of the water/IPA solvent greatly decreases the solubility of NiO nanoparticles. The poor film morphology observed was likely due to rapid evaporation of IPA solvent. So, taking an idea from the use of Triton X-100 solvent additive in the solution-based deposition of PEDOT:PSS hole transport layers, a small amount of 2-butanol was added to slow solvent evaporation. A NiO film deposited using this additive showed clear and uniform macroscopic morphology (**Figure 4.4d**). 2-Butanol has been shown to allow uniform inkjet printing of solution-processed 2D-crystal ink by suppressing the coffee ring effect (CRE).<sup>[104]</sup> Although the present method of deposition was different, we attributed the greater film uniformity to the same CRE suppression effect, due to increased surface tension and thus increased wettability. The enhanced wettability of the NiO solution including 2-butanol was confirmed by contact angle measurements of NiO solution dropped on active layers; the NiO solution with 2-butanol exhibited a clearly smaller contact angle compared to that without 2-butanol (**Figure 4.4e–f**).

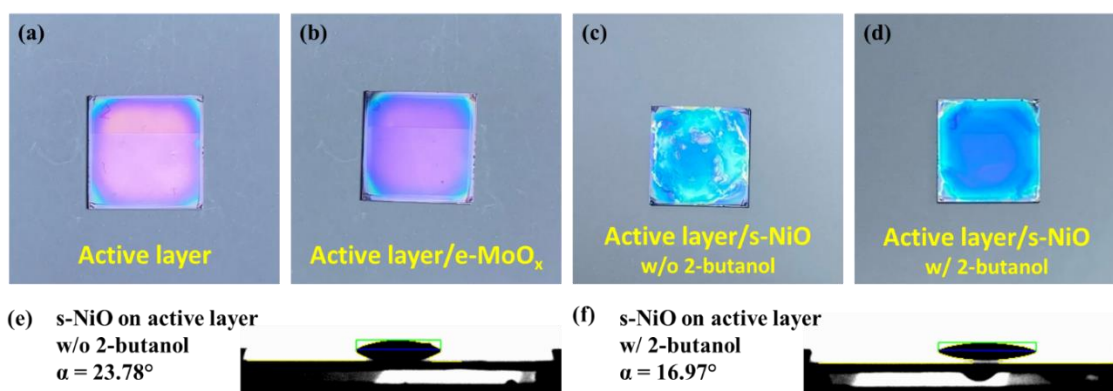


**Figure 4.4** (a) Digital photograph of PTB7-Th:IEICO-4F active layer. (b–d) Digital photographs of (b) e-MoO<sub>x</sub>, (c) s-NiO without 2-butanol, and (d) s-NiO with 2-butanol deposited on active layers. (e–f) Contact angle measurements on active layers of drops of NiO solutions (e) without and (f) with 2-butanol.

The microscopic morphology of the NiO film on the polymer active layer was investigated by atomic force microscopy (AFM). **Figure 4.5** shows a topographic image of NiO film prepared from NiO solutions with and without 2-butanol. The NiO film deposited using a solution with 2-butanol exhibited fine morphology and less cluster aggregation, confirming the role of 2-butanol in the formation of uniform and continuous NiO film on the polymer active layer. Transmittance spectra of HTLs of PEDOT:PSS, e-MoO<sub>x</sub>, and s-NiO deposited on the ITO substrate are shown in **Figure 4.6**. The band gaps of the e-MoO<sub>x</sub> and s-NiO films (**Figure 4.6b** and **Figure 4.6c**) were calculated as 3.24 and 3.6 eV, respectively. These results are consistent with other reports on MoO<sub>x</sub> and NiO.<sup>[5,12]</sup>

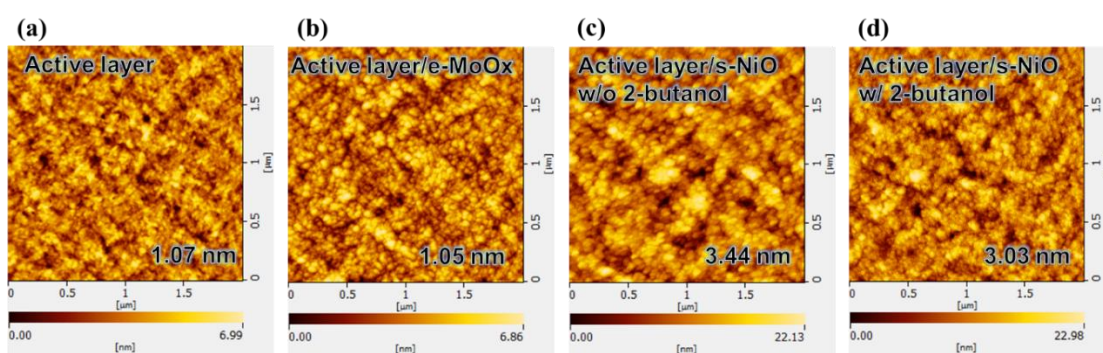


**Figure 4.5** (a) AFM topography of a polymer active layer. (b–d) AFM topography of HTL layers deposited on the polymer active layer: (b) e-MoO<sub>x</sub> and (c) s-NiO from a solution without 2-butanol and (d) s-NiO from a solution with 2-butanol.

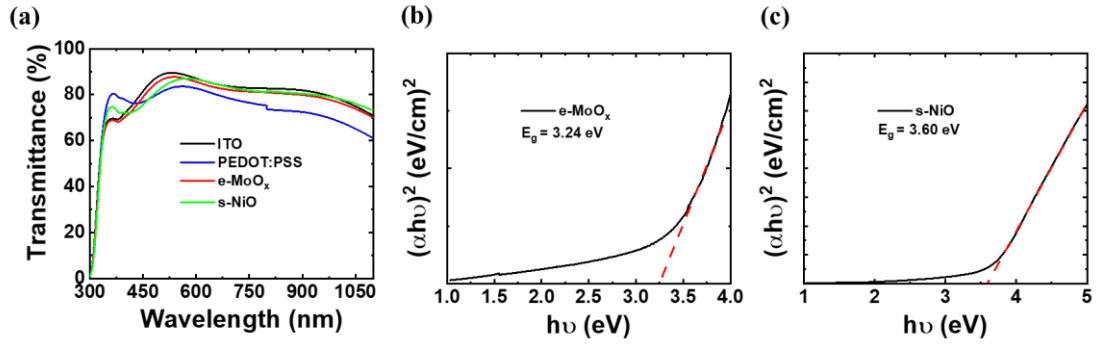


**Figure 4.6** (a) Transmittance spectra of PEDOT:PSS, e-MoO<sub>x</sub>, and s-NiO deposited on ITO substrates. (b–c) Tauc plots of (b) e-MoO<sub>x</sub> and (c) s-NiO films.

**Table 4.1** Photovoltaic performance parameters of inverted and conventionally structured polymer solar cells based on PTB7-Th:IEICO-4F blend films with s-NiO layers.

Device structure	Description	JV $J_{SC}$ [mA cm <sup>-2</sup> ]	EQE $J_{SC}$ [mA cm <sup>-2</sup> ]	$V_{OC}$ [V]	FF [%]	Best PCE [%]
	w/o HTL	20.99	19.72	0.286	43.4	2.60
ITO/ZnO/Active/HTL/Ag	e-MoO <sub>x</sub>	24.12	23.79	0.708	65.7	11.22
	s-NiO	23.99	23.01	0.719	65.1	11.23
	w/o HTL	21.88	20.06	0.512	31.3	3.51
ITO/HTL/Active/ZnO/Al	PEDOT:PSS	24.18	23.20	0.725	63.9	11.20
	s-NiO	24.20	23.01	0.713	65.0	11.22

\*Active layer: PTB7-Th:IEICO-4F

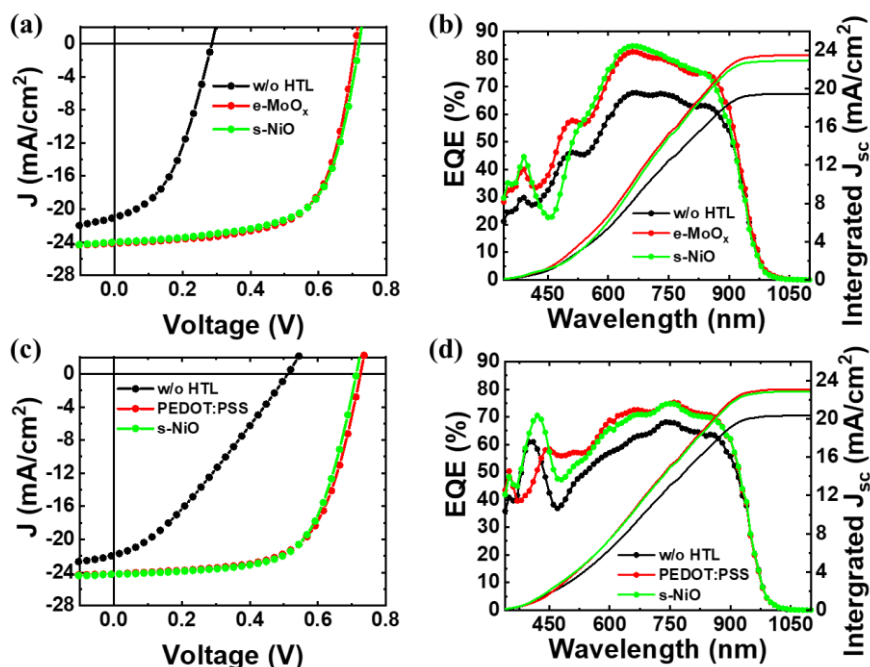


**Figure 4.7** (a)  $J$ - $V$  characteristics and (b) EQE spectra of inverted polymer solar cells based on PTB7-Th:IEICO-4F blend films with s-NiO and e-MoO<sub>x</sub> as hole transport layers. (c)  $J$ - $V$  characteristics and (d) EQE spectra of conventional polymer solar cells based on PTB7-Th:IEICO-4F blend films with s-NiO and PEDOT:PSS as hole transport layers.

Current density ( $J$ ) versus voltage ( $V$ ) characteristics and external quantum efficiency (EQE) spectra of inverted non-fullerene solar cells based on PTB7-Th:IEICO-4F and having the annealing-free solution-processable NiO layer (s-NiO with 2-butanol) were acquired, and the  $J$ - $V$  results were compared to those obtained from an inverted device with a thermally evaporated MoO<sub>x</sub> layer (e-MoO<sub>x</sub>) and a device with no HTL (**Figure 4.7a-b**). The HTL quite obviously played an important role in the achievement of high efficiency in the PSC. A solar cell with no HTL exhibited major loss in open circuit voltage ( $V_{oc}$ ) and short circuit current ( $J_{sc}$ ), leading to poorer power conversion efficiency (PCE). This device showed a notably low PCE of 2.6%, with  $J_{sc}$  of 20.99 mA cm<sup>-2</sup>,  $V_{oc}$  of 0.286 V, and a fill factor (FF) of 43.4%. This low efficiency was caused mostly by recombination of holes and electrons at the interface between the polymer active layer and anode electrode.<sup>[105]</sup> The solar cell with e-MoO<sub>x</sub> showed much better overall photovoltaic performance of 11.22% PCE, 24.12 mA cm<sup>-2</sup>  $J_{sc}$ , 0.708 V  $V_{oc}$ , and 65.7% FF. This result was consistent with a previous report.<sup>[106]</sup> The inverted solar cell with the s-NiO HTL performed comparably to the solar cell with the e-MoO<sub>x</sub> HTL, with 11.23% PCE, 23.99 mA cm<sup>-2</sup>  $J_{sc}$ , 0.719 V  $V_{oc}$ , and 65.1% FF. **Table 4.1** lists the measured parameters of photovoltaic performance inverted and conventionally structured polymer solar

cells based on PTB7-Th:IEICO-4F blend films with s-NiO layers. Note that no post annealing process was applied to the s-NiO HTL; the complete deposition process comprised spin casting of the NiO nanoparticle suspension onto the organic active layer, followed by drying in a glovebox for 10 min. The  $J$ - $V$  characteristics and photovoltaic performance of the inverted polymer solar cells based on PTB7-Th:IEICO-4F with different thicknesses of s-NiO were shown in **Figure 4.8** and **Table 4.2**, respectively.

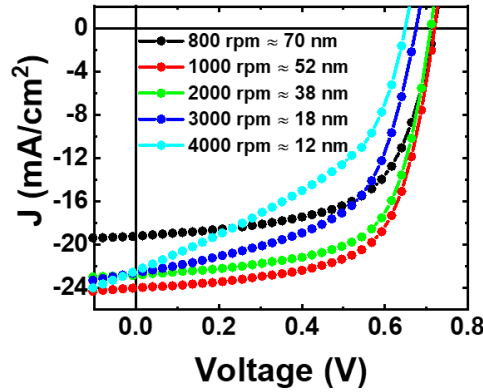


**Figure 4.8**  $J$ - $V$  characteristics of the inverted polymer solar cell based on PTB7-Th:IEICO-4F blend films with different thicknesses of NiO layer.

**Table 4.2** Photovoltaic performance of the inverted polymer solar cell based on PTB7-Th:IEICO-4F blend films with different thicknesses of NiO layer.

s-NiO spin speed	s-NiO Thickness (approximately)	$J_{sc}$ [ $\text{mA}/\text{cm}^2$ ]	$V_{oc}$ [V]	FF [%]	PCE [%]
800 rpm	70 nm	19.21	0.72	61.03	8.44
1000 rpm	52 nm	23.99	0.72	65.08	11.23
2000 rpm	38 nm	22.81	0.71	65.05	10.54
3000 rpm	18 nm	22.59	0.68	55.83	8.58
4000 rpm	12 nm	22.42	0.65	43.05	6.27

Spin-casting of an organic photoactive layer over the s-NiO layer posed no difficulty.  $J$ - $V$  characteristics and the EQE spectra of conventionally structured non-fullerene solar cells based on PTB7-Th:IEICO-4F with either PEDOT:PSS or s-NiO were acquired and compared and were compared to those of a cell with no HTL (**Figure 4.7c-d**). The conventionally structured solar cell with s-NiO HTL also showed a high PCE of 11.22%, without the application of a post annealing process. The PCE acquired was comparable with that of the conventionally structured



solar cell fabricated with a PEDOT:PSS HTL. PEDOT:PSS must be annealed at 120–150 °C to achieve good HTL performance,<sup>[107]</sup> whereas the presently developed s-NiO layer does not require annealing. Thus, s-NiO is a better HTL candidate for use in future roll-to-roll mass production.

To clarify the universality of s-NiO in polymer solar cells, we have applied s-NiO HTL on conventional fullerene solar cells based on PTB7-Th:PC<sub>71</sub>BM. The *J-V* characteristics, EQE spectra, and photovoltaic performance of the inverted and conventional fullerene solar cells are shown in **Figure 4.9** and **Table 4.3**. The device with s-NiO showed comparable performance with both inverted solar cell with e-MoO<sub>x</sub> HTL and conventional solar cells with PEDOT:PSS HTL. Note that the s-NiO was also well coated on the PTB7-Th:PC<sub>71</sub>BM polymer active layer (see **Figure 4.10**). Recently, new commercial PEDOT:PSS product, named ‘CLEVIOS™ HTL Solar’, was launched for inverted polymer solar cells. In direct comparison with s-NiO, the efficiency of the solar cell with ‘CLEVIOS™ HTL Solar’ was lower than that of the solar cell with s-NiO as shown in **Figure 4.11** and **Table 4.4**. The lower performance of solar cell with ‘CLEVIOS™ HTL Solar’ was attributed to the decreased *V*<sub>OC</sub>, which was a result of the low work-function of ‘CLEVIOS™ HTL Solar’ of 4.8 eV compared with that of s-NiO of 5.14 eV.

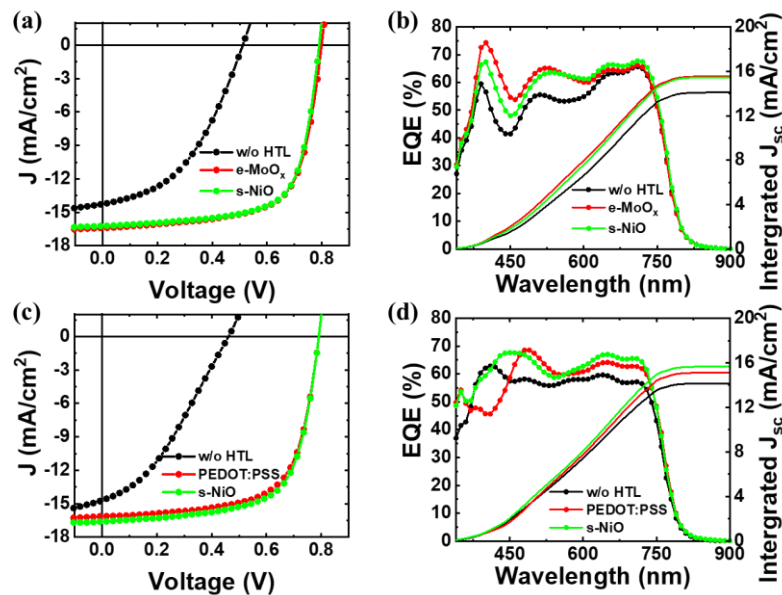


**Figure 4.9** (a) *J-V* characteristics and (b) EQE spectra of the inverted polymer solar cell based on PTB7-Th:PC<sub>71</sub>BM blend films with s-NiO and e-MoO<sub>x</sub> as hole transport layers. (c) *J-V* characteristics and (d) EQE spectra of the conventional polymer solar cell based on PTB7-Th:PC<sub>71</sub>BM blend films with s-NiO and PEDOT:PSS as hole transport layers.

**Table 4.3** Photovoltaic performance parameters of inverted and conventionally structured polymer solar cells based on PTB7-Th:PC<sub>71</sub>BM blend films with s-NiO layers.

Device Structure	Description	JV J <sub>sc</sub> [mA/cm <sup>2</sup> ]	EQE J <sub>sc</sub> [mA/cm <sup>2</sup> ]	V <sub>oc</sub> [V]	FF [%]	Best PCE [%]
ITO/ZnO/Active/HTL/Ag	w/o HTL	14.26	14.15	0.51	43.96	3.20
	e-MoO <sub>x</sub>	16.41	15.75	0.80	67.97	8.92
	s-NiO	16.23	15.60	0.79	69.13	8.86
ITO/HTL/Active/ZnO/Al	w/o HTL	14.70	14.30	0.46	34.48	2.33
	PEDOT:PSS	16.13	15.30	0.79	66.74	8.51
	s-NiO	16.61	15.86	0.79	67.44	8.85

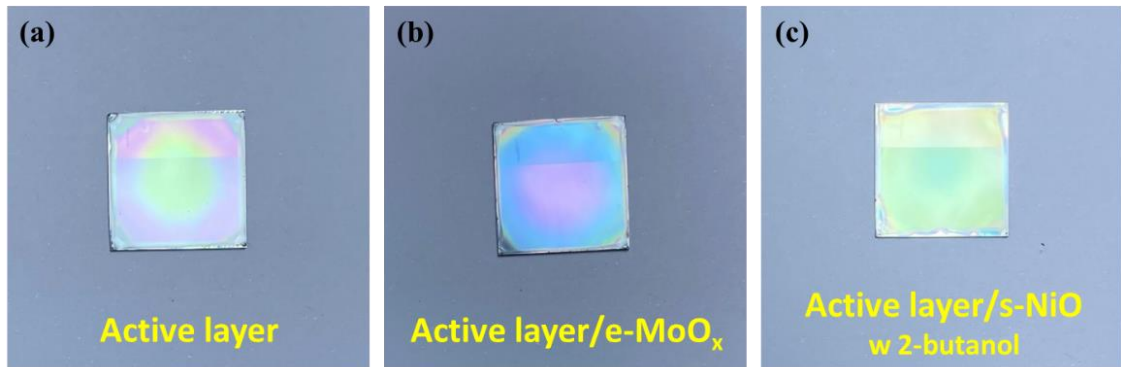


**Figure 4.10** (a) Digital photograph of PTB7-Th:PC<sub>71</sub>BM active layer. Digital photograph of (b) e-MoO<sub>x</sub>, and (c) s-NiO w/ 2-butanol deposited on active layer.

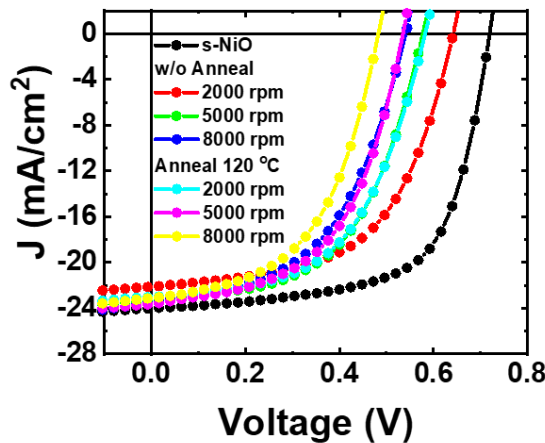


**Figure 4.11**  $J$ - $V$  characteristics of the inverted polymer solar cell based on PTB7-Th:IEICO-4F blend films with 'CLEVIOS™ HTL Solar' hole transport layers.



**Table 4.4** Photovoltaic performance of the inverted polymer solar cell based on PTB7-Th:IEICO-4F blend films with ‘CLEVIOS™ HTL Solar’ hole transport layers.

	Description	$J_{sc}$ [mA/cm <sup>2</sup> ]	$V_{oc}$ [V]	FF [%]	PCE [%]
	s-NiO	23.99	0.72	65.08	11.23
PEDOT:PSS	Spin speed 2000 rpm	22.11	0.64	56.41	7.98
HTL Solar	Spin speed 5000 rpm	23.31	0.58	54.76	7.40
w/o Anneal	Spin speed 8000 rpm	23.53	0.54	50.98	6.48
PEDOT:PSS	Spin speed 2000 rpm	23.01	0.58	54.48	7.27
HTL Solar	Spin speed 5000 rpm	23.62	0.54	53.76	6.86
Anneal 120 °C	Spin speed 8000 rpm	23.11	0.48	52.12	5.78

To compare in more detail the charge transport and recombination properties of e-MoO<sub>x</sub> and s-NiO HTLs, their light intensity dependence of  $J_{SC}$  and  $V_{OC}$ , hole mobility, and impedance spectroscopy were measured (**Figure 4.12**). Solar cells with e-MoO<sub>x</sub> or s-NiO HTLs both showed linear dependence of  $J_{SC}$  upon light intensity, with the same  $\alpha$  value of 0.94. In general,  $J_{SC}$  exhibits power-law dependence upon light intensity ( $I$ ), which can be expressed as  $J_{SC} \propto I^\alpha$ , where  $\alpha$  is a value obtained from linear fitting of data.<sup>[108]</sup> The value  $\alpha = 1$  corresponds to the ideal case in which bimolecular recombination is eliminated.<sup>[109]</sup> Therefore, the small deviation from  $\alpha = 1$  observed both solar cells indicated that bimolecular recombination was relatively weak in the short circuit condition of both devices. Another similarity of the two solar cells with the e-MoO<sub>x</sub> and s-NiO HTL was observed in the light intensity dependence of  $V_{OC}$ .  $V_{OC}$  exhibited a linear relationship with the logarithm of light intensity ( $\ln I$ ), which can be expressed as  $V_{OC} \propto n(kT/q)\ln(I)$ , where  $k$  is the Boltzmann constant,  $T$  is the absolute temperature,  $q$  is the elementary charge, and the ideality factor  $n$  is determined from fitting. Bimolecular recombination dominates when the  $n$  value is approximately equal to unity, whereas Shockley–Read–Hall recombination (monomolecular recombination) dominates for  $n$  values greater than unity.<sup>[110]</sup> Regarding the light intensity dependence<sup>[110]</sup> of  $V_{OC}$ , the  $n$  value of the cell with the e-MoO<sub>x</sub> HTL was 1.080 ( $kT/q$ ), and the  $n$  value of the solar cell with s-NiO HTL was 1.098 ( $kT/q$ ). Both solar cells showed  $n$  values higher than but close to 1.0, indicating predominance of monomolecular recombination, which usually occurs at defect states at the interface between the polymer active layer and the HTL. Although the solar cell with s-NiO HTL showed slightly higher  $n$  values, s-NiO deposited by the solution process showed a similar level of trap-assisted

recombination to that of e-MoO<sub>x</sub> deposited by thermal evaporation. These results indicate that the quality of our s-NiO with regard to defects is almost equivalent to that of e-MoO<sub>x</sub>.

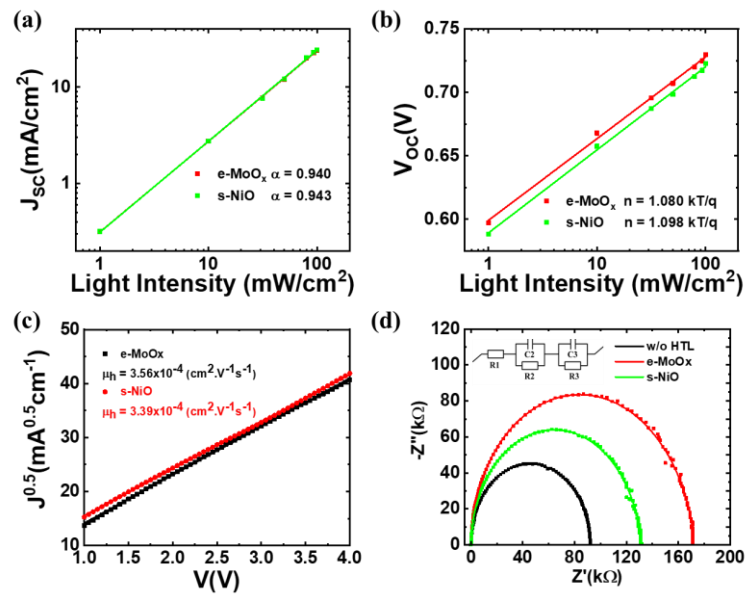


**Figure 4.12** (a–b) Light intensity dependence of (a)  $J_{sc}$  and (b)  $V_{oc}$ . (c) Hole mobilities of hole-only devices based on PTB7-Th:IEICO-4F blend films with e-MoO<sub>x</sub> and s-NiO hole transport layers and with no hole transport layer. (d) Nyquist plot of IS measurements collected under dark conditions of inverted polymer solar cells with various HTLs.

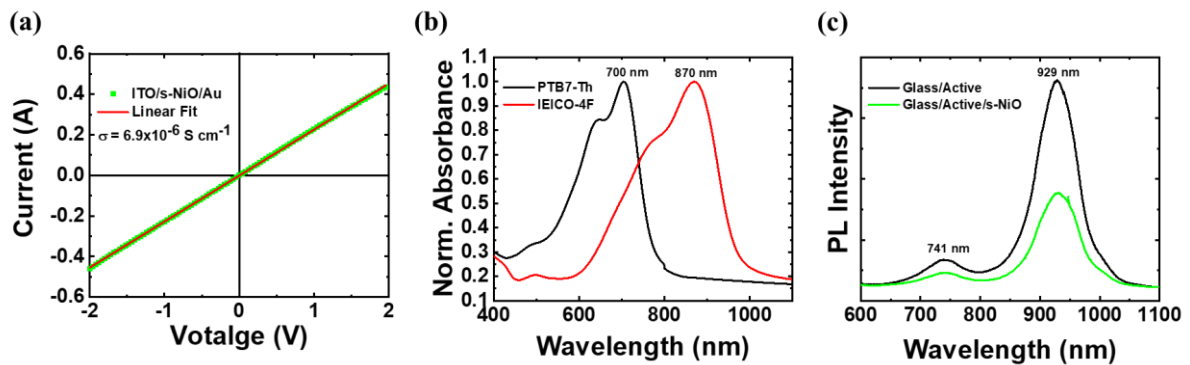


**Figure 4.13** (a) I–V curve of s-NiO film based on the structure of ITO/s-NiO/Au. (b) Absorption spectra of p-type polymer PTB7-Th and non-fullerene acceptor IEICO-4F, (c) Photoluminescence of Glass/PTB7-Th:IEICO-4F and Glass/PTB7-Th:IEICO-4F/s-NiO.

**Figure 4.12c** shows the hole mobility analysis obtained from hole-only devices with the structure of ITO/PEDOT:PSS/PTB7-Th:IEICO-4F/(e-MoO<sub>x</sub> or s-NiO)/Ag. Hole mobility was determined by the steady-state space-charge-limited current (SCLC) method, and hole mobility was defined as the mobility of the hole traveling from the polymer active layer to the anode

through the HTL. The polymer active layer was 110 nm thick and had the dielectric constant of 3.<sup>[111]</sup> The extracted hole mobility of the solar cell with s-NiO HTL was  $3.39 \times 10^{-4} \text{ cm}^2 \text{ V}^{-1} \text{ s}^{-1}$ , while that of the cell with the e-MoO<sub>x</sub> HTL was  $3.56 \times 10^{-4} \text{ cm}^2 \text{ V}^{-1} \text{ s}^{-1}$ , indicating that the e-MoO<sub>x</sub> and s-NiO HTLs had similar hole transport properties. The I-V curve of NiO film based on the structure ITO/s-NiO/Au is plotted in **Figure 4.13a**. As shown in **Figure 4.13a**, the conductivity value of s-NiO is estimated to be  $6.9 \times 10^{-6} \text{ S cm}^{-1}$ , which is similar to another report.<sup>[112]</sup> The photoluminescence (PL) of Glass/PTB7-Th:IEICO-4F and Glass/PTB7-Th:IEICO-4F/s-NiO with the excitation wavelength of 475 nm were also measured (see **Figure 4.13c**) to check the hole transport property of s-NiO. The PL intensity of the polymer active layer with s-NiO was lower than the PL intensity of the polymer active layer without s-NiO. In the sample without s-NiO layer, excited charge by incident excitation light has higher possibility of radiative recombination. However, in the sample with s-NiO, some portion of holes were transferred to s-NiO, thereby reducing the radiative recombination probability inside the polymer active layer.<sup>[113]</sup> To investigate the difference between the e-MoO<sub>x</sub> and s-NiO HTLs at the interface, impedance spectroscopy (IS) was conducted under dark conditions. **Figure 4.12d** shows Nyquist plots of the IS measurements, together with a plot for the device without an HTL for comparison. All Nyquist plots showed one semicircle without a transmission line. The absence of a transmission line indicates that the recombination resistance ( $R_{\text{rec}}$ ) dominated the transportation resistance ( $R_{\text{tr}}$ ). Under this strong recombination condition, dark-state IS data are normally interpreted using the Gerischer impedance model; the Gerischer resistance ( $R_{\text{G}}$ ) is defined as the square root of the product of  $R_{\text{rec}}$  and  $R_{\text{tr}}$ .<sup>[76,78,114]</sup> Under strong recombination,  $R_{\text{rec}}$  is equivalent to  $R_{\text{G}}$ . The device without the HTL exhibited the lowest real-part impedance, meaning that this device had the least recombination resistance (i.e., the highest recombination probability). In the comparison between e-MoO<sub>x</sub> HTL and s-NiO HTL, the device with s-NiO had lower recombination resistance. The overall device performance was not significantly different between these two devices, but it was observed that e-MoO<sub>x</sub>, deposited by thermal evaporation, performed somewhat better in terms of recombination at the interface. This IS result is consistent with the light intensity dependence of  $V_{\text{OC}}$ . A slightly higher  $n$  value was observed for the device with the s-NiO HTL in the previous measurements of light intensity dependence of  $V_{\text{OC}}$ .

To further understand the s-NiO HTL, X-ray photoelectron spectroscopy (XPS) and ultraviolet photoelectron spectroscopy (UPS) studies were conducted. XPS spectra of the Ni 2p<sub>3/2</sub> and O 1s states of the s-NiO film are shown in **Figures 4.14a** and **Figures 4.14b**,

respectively. The observed Ni 2p<sub>3/2</sub> state can be divided into three peaks: a broad peak centered at 860.9 eV and assigned to shake-up satellites of NiO, a peak centered at 853.7 eV and assigned to the oxidation state Ni<sup>2+</sup>, and a peak centered at 855.4 eV and assigned to the oxidation state Ni<sup>3+</sup>, comprised of Ni in NiOOH and Ni<sub>2</sub>O<sub>3</sub> species. The observed O 1s state can be deconvoluted into two peaks, with binding energy peaks at 529.2 and 531 eV, respectively, corresponding to the oxidation states Ni<sup>2+</sup> and Ni<sup>3+</sup>. These XPS analyses confirmed that the composition of the nickel oxide was nonstoichiometric, a result similar to that of other studies.<sup>[11,12]</sup> UPS spectra were acquired of the cut-off region and the HOMO region of the s-NiO HTL to investigate its energy level structure in detail and were compared to the corresponding e-MoO<sub>x</sub> HTL spectra (**Figures 4.14c–d**). **Table 4.5** summarizes various parameters extracted from the UPS such as WF, ion potential, electron injection barrier, and hole injection barrier.

**Table 4.5** Summary of the parameters obtained from UPS data of various HTL layers: PEDOT:PSS, e-MoO<sub>x</sub> and s-NiO. The notations E<sub>g</sub>, WF, IP, Φ<sub>e</sub>, and Φ<sub>h</sub> respectively denote the optical band gap, work function, ion potential, electron injection barrier, and hole injection barrier.

Condition	E <sub>g</sub> (eV)	WF (eV)	IP (eV)	Φ <sub>e</sub> (eV)	Φ <sub>h</sub> (eV)
ITO	N/A	4.78	N/A	N/A	N/A
PEDOT:PSS	N/A	5.10	N/A	N/A	N/A
e-MoO <sub>x</sub>	3.24	5.90	8.47	0.67	2.57
s-NiO	3.60	5.14	5.55	3.19	0.41

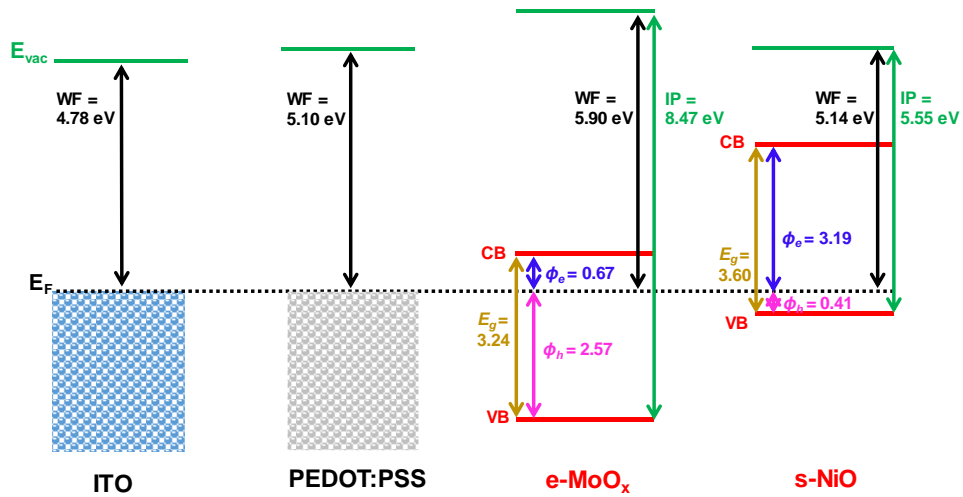


**Figure 4.15** Energy band diagrams of e-MoO<sub>x</sub> and s-NiO films based upon UPS measurements. Band gaps ( $E_g$ ) of e-MoO<sub>x</sub> and s-NiO films were extracted from transmittance spectra.

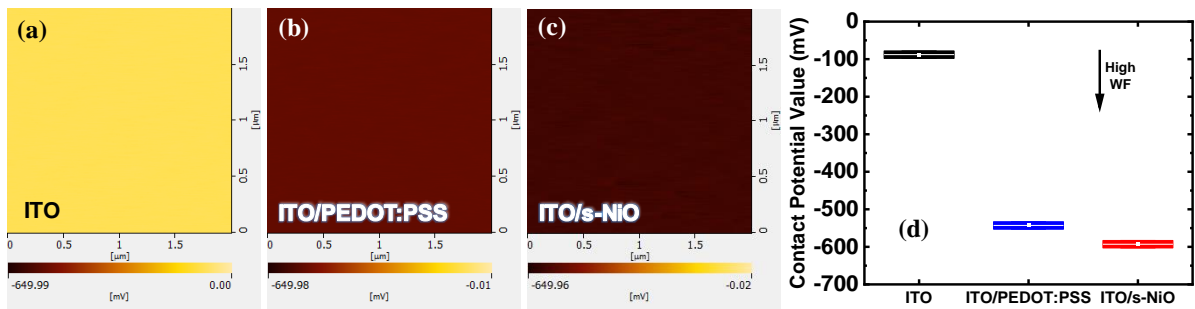


**Figure 4.16** (a–c) Surface potential images of (a) ITO, (b) ITO/PEDOT:PSS, and (c) ITO/s-NiO. (d) Summary of surface potential values of PEDOT:PSS and s-NiO deposited on ITO.

The energy band diagram extracted from the UPS study is presented in **Figure 4.15**. The reference WF of the ITO electrode layer was 4.78 eV. The extracted WF of the s-NiO HTL was 5.14 eV, similar to the 5.1 eV WF of PEDOT:PSS. The hole extraction barrier of s-NiO HTL was 0.41 eV, suitable for hole extraction without accumulation at the interface. The overall energy level diagram feature of e-MoO<sub>x</sub> was consistent with previous studies.<sup>[3,115]</sup> However, such an energy level configuration is advantageous for electron injection. Actually, the hole extraction mechanism of MoO<sub>x</sub> was different from that of NiO. Hole extraction occurs by recombination of electrons in the conduction band of e-MoO<sub>x</sub> and holes in the HOMO of the PTB7-Th polymer because the HOMO of PTB7-Th polymer is close to the conduction band of e-MoO<sub>x</sub>.<sup>[3]</sup> From these results, it is clear that the s-NiO exhibits typical intrinsic p-type hole transport, whereby photogenerated holes from the conjugated polymer are transported to the

anode through the valence band of s-NiO. **Figure 4.16** shows the surface potentials of ITO/PEDOT:PSS, ITO/s-NiO, and ITO examined with Kelvin probe force microscopy (KPFM) measurement. These surface potential measurements showed results consistent with the UPS results. The surface potential of e-MoO<sub>x</sub> was omitted in this experiment because the e-MoO<sub>x</sub> was easily oxidized in air and would lead to inaccurate results.<sup>[116]</sup> Instead, PEDOT:PSS was used in this potential comparison study. The measured surface potential of the s-NiO layer was  $-583$  mV, slightly lower than that of PEDOT:PSS,  $-533$  mV. Note that the measured surface potential of ITO was  $-78$  mV. Lower surface potential indicates higher WF; thus, the lower potential of s-NiO meant a higher WF compared to that of the PEDOT:PSS.<sup>[117]</sup>

Finally, the stability performance of a non-fullerene solar cell based on PTB7-Th:IEICO-4F was investigated. To test stability, changes in  $J_{SC}$ ,  $V_{OC}$ , FF, and PCE of inverted PSCs using either e-MoO<sub>x</sub> or s-NiO were monitored during continuous light illumination in air for 25 h, as shown in **Figure 4.17**. It is well known that non-fullerene-based solar cells have relatively poor stability compared with fullerene-based solar cells due to poorer photochemical stability and burn-in properties of the non-fullerene acceptor.<sup>[118,119]</sup> Some rapid degradation of PCE was observed in devices with e-MoO<sub>x</sub> HTLs, a finding similar to those of other reports on the stability of PTB7-Th:IEICO-4F solar cells.<sup>[119]</sup> Interestingly, the solar cells with s-NiO HTLs exhibited better stability than those with e-MoO<sub>x</sub> HTLs.

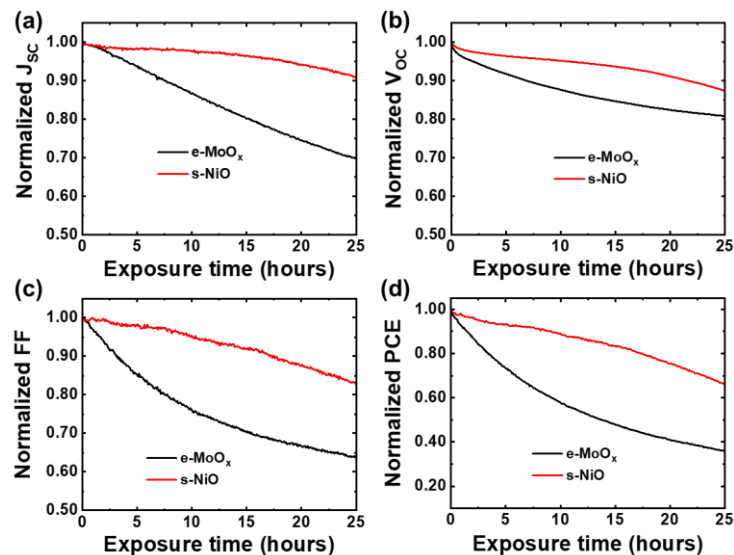


**Figure 4.17** Stability testing: changes in normalized (a)  $J_{SC}$ , (b)  $V_{OC}$ , (c) FF, and (d) PCE during continuous monitoring (interval: 5 min) of devices subjected to continuous illumination for 25 h.

#### **4.4 Conclusion**

Room-temperature, annealing-free, solution-processable NiO (s-NiO) was successfully developed and was applied to both conventional and inverted non-fullerene polymer solar cells based on PTB7-Th:IEICO-4F. To overcome the wettability problem, the solvent, which conventionally is DI water, was replaced with a mixed solution of DI water and isopropyl alcohol with a 2-butanol additive. This allowed the deposition of NiO nanoparticle suspension onto the hydrophobic active layer surface. Even without annealing or UV–ozone treatment, the inverted device using s-NiO exhibited efficiency equivalent to that of a reference device fabricated using evaporated MoO<sub>x</sub> (e-MoO<sub>x</sub>). In addition, conventionally structured solar cells with s-NiO HTLs exhibited similar photovoltaic performance to that of reference solar cells having PEDOT:PSS HTLs. To the best of our knowledge, this is the first report of application of s-NiO in inverted solar cells by solution processing without post-treatment. Because our NiO nanoparticle suspension has a low fabrication cost compared to commercial PEDOT:PSS and evaporated MoO<sub>x</sub>, it is a promising candidate for hole transport layers of future flexible polymer solar cells fabricated by the roll-to-roll processes.

## Chapter 5. Summary

In summary, the novel annealing-free solution-processable aqueous  $\text{MoO}_x$  and NiO nanoparticles suspension were successfully developed. In particular, the charge transport layer based on  $\text{MoO}_x$  prepared by an anhydrous sol-gel method with  $\text{MoO}_2(\text{acac})_2$  as precursor normally requires high-temperature annealing in air to achieve desired quality by removing acetylacetonate ligand (acac). For this reason, the non-fullerene solar cell based on PBDB-T-2F:Y6 with the general an- $\text{MoO}_x$  HTL prepared by the sol-gel method showed a poor efficiency of 7.7% without annealing. This poor efficiency was recovered to the normal value of 17% that typically observed in solar cells when this an- $\text{MoO}_x$  layer was annealed at 200 °C. However, the solar cell with aq- $\text{MoO}_x$  prepared by the aqueous sol-gel method showed almost comparable performance to the solar cell with the annealed an- $\text{MoO}_x$  HTL, even without high-temperature annealing. Moreover, the solar cell with aq- $\text{MoO}_x$  exhibited a higher efficiency and better stability without high-temperature annealing compared to the solar cells with PEDOT:PSS. We figured out that the hydrolysis reaction in aq- $\text{MoO}_x$  solution would break the bonding of  $\text{MoO}_2$  with acetylacetonate ligand. For this result, the aq- $\text{MoO}_x$  HTL shows the equivalent performance with an- $\text{MoO}_x$  HTL and PEDOT:PSS HTL without requiring high-temperature annealing.

On the other hand, the annealing-free solution-processable NiO (s-NiO) was successfully applied to both conventional and inverted non-fullerene polymer solar cells based on PTB7-Th:IEICO-4F. The conventional solvent of NiO nanoparticle suspension is DI water, which was hard to deposit onto the hydrophobic active layer. To overcome the wettability problem, the conventional solvent was replaced with a mixture of DI water and isopropyl alcohol with a 2-butanol additive. The high boiling point of 2-butanol decreased the evaporation rate of the mixture solvent while spun coating on the active layer. As a result, this allowed the deposition of NiO nanoparticle suspension onto the hydrophobic active layer surface. Furthermore, the inverted device using s-NiO exhibited efficiency equivalent to that of a reference device fabricated using evaporated  $\text{MoO}_x$  (e- $\text{MoO}_x$ ) without using high-temperature annealing or UV-ozone treatment. Moreover, conventionally structured solar cells with s-NiO HTLs exhibited similar photovoltaic performance to that of reference solar cells having PEDOT:PSS HTLs. To the best of our knowledge, this is the first report of application of s-NiO in inverted solar cells by solution processing without post-treatment. Although high-temperature annealing is not a difficult process in laboratory scale production, it is definitely not a simple process to apply in



roll-to-roll processes because of the inevitable long cooling step that follows. Thus, our aqueous annealing-free solutions such as aq-MoO<sub>x</sub> and s-NiO are promising candidates for hole transport layers of future flexible polymer solar cells fabricated by the roll-to-roll processes.

Furthermore, we also investigated the effect of three different additives (DIO, CN, DPE) on the performance of polymer-polymer solar cells based on a PTB7-Th:P(NDI2OD-T2). In general, the role of additive in organic solar cells based on the BHJ active layer is to induce good phase separation between the donor and acceptor. Although each solvent additive exhibited a unique optimization point, the efficiency enhancement between the solar cell without additive and the solar cell with additive was not significant. From the GIWAXS results, there was no significant morphology change in the polymer-polymer active layer due to the additive with optimal ratio. All polymer-polymer active layers with the optimal additive ratio had only face-on orientation, whereas a mixture of face-on orientation and edge-on orientation was found at all polymer-polymer active layers with the non-optimal additive ratio. This is likely the reason for the decrease in efficiency observed for excess additive. With IMVS results, we can conclude that the reason for enhanced performance in solar cells with additive was the reduced recombination rather than crystalline morphology improvements.

## References

- [1] Q. Liu, Y. Jiang, K. Jin, J. Qin, J. Xu, W. Li, J. Xiong, J. Liu, Z. Xiao, K. Sun, S. Yang, X. Zhang, L. Ding, *Sci. Bull.* **2020**, *65*, 272.
- [2] O. De Melo, V. Torres-Costa, A. Climent-Font, P. Galán, A. Ruediger, M. Sánchez, C. Calvo-Mola, G. Santana, V. Torres-Costa, *J. Phys. Condens. Matter* **2019**, *31*, 295703.
- [3] J. Meyer, S. Hamwi, M. Kröger, W. Kowalsky, T. Riedl, A. Kahn, *Adv. Mater.* **2012**, *24*, 5408.
- [4] K. Zilberberg, H. Gharbi, A. Behrendt, S. Trost, T. Riedl, *ACS Appl. Mater. Interfaces* **2012**, *4*, 1164.
- [5] J. J. Jasieniak, J. Seifert, J. Jo, T. Mates, A. J. Heeger, *Adv. Funct. Mater.* **2012**, *22*, 2594.
- [6] M. Nachman, L. N. Cojocaru, L. V. Rîbco, *Phys. status solidi* **1965**, *8*, 773.
- [7] X. Zhao, J. Chen, N. Park, *Sol. RRL* **2019**, *3*, 1800339.
- [8] U. Kwon, B. G. Kim, D. C. Nguyen, J. H. Park, N. Y. Ha, S. J. Kim, S. H. Ko, S. Lee, D. Lee, H. J. Park, *Sci. Rep.* **2016**, *6*, 1.
- [9] K. X. Steirer, P. F. Ndione, N. E. Widjonarko, M. T. Lloyd, J. Meyer, E. L. Ratcliff, A. Kahn, N. R. Armstrong, C. J. Curtis, D. S. Ginley, J. J. Berry, D. C. Olson, *Adv. Energy Mater.* **2011**, *1*, 813.
- [10] B. Mustafa, J. Griffin, A. S. Alsulami, D. G. Lidzey, A. R. Buckley, *Appl. Phys. Lett.* **2014**, *104*, 063302.
- [11] J. R. Manders, S.-W. Tsang, M. J. Hartel, T.-H. Lai, S. Chen, C. M. Amb, J. R. Reynolds, F. So, *Adv. Funct. Mater.* **2013**, *23*, 2993.
- [12] F. Jiang, W. C. H. Choy, X. Li, D. Zhang, J. Cheng, *Adv. Mater.* **2015**, *27*, 2930.
- [13] C. M. Proctor, M. Kuik, T. Q. Nguyen, *Prog. Polym. Sci.* **2013**, *38*, 1941.
- [14] G.-J. A. H. Wetzelaer, M. Kuik, P. W. M. Blom, *Adv. Energy Mater.* **2012**, *2*, 1232.
- [15] F. C. Krebs, T. Tromholt, M. Jørgensen, *Nanoscale* **2010**, *2*, 873.

- [16] L. Lu, L. Yu, *Adv. Mater.* **2014**, *26*, 4413.
- [17] J. Kalowekamo, E. Baker, *Sol. Energy* **2009**, *83*, 1224.
- [18] R. Søndergaard, M. Hösel, D. Angmo, T. T. Larsen-Olsen, F. C. Krebs, *Mater. Today* **2012**, *15*, 36.
- [19] Y. Liu, J. Zhao, Z. Li, C. Mu, W. Ma, H. Hu, K. Jiang, H. Lin, H. Ade, H. Yan, *Nat. Commun.* **2014**, *5*, 5293.
- [20] T. L. Nguyen, H. Choi, S. J. Ko, M. A. Uddin, B. Walker, S. Yum, J. E. Jeong, M. H. Yun, T. J. Shin, S. Hwang, J. Y. Kim, H. Y. Woo, *Energy Environ. Sci.* **2014**, *7*, 3040.
- [21] S.-H. Liao, H.-J. Jhuo, Y.-S. Cheng, S.-A. Chen, *Adv. Mater.* **2013**, *25*, 4766.
- [22] N. Wang, Z. Chen, W. Wei, Z. Jiang, *J. Am. Chem. Soc.* **2013**, *135*, 17060.
- [23] A. Facchetti, *Mater. Today* **2013**, *16*, 123.
- [24] T. Earmme, Y.-J. Hwang, N. M. Murari, S. Subramaniyan, S. A. Jenekhe, *J. Am. Chem. Soc.* **2013**, *135*, 14960.
- [25] Y.-J. Hwang, B. A. E. Courtright, A. S. Ferreira, S. H. Tolbert, S. A. Jenekhe, *Adv. Mater.* **2015**, *27*, 4578.
- [26] X. He, F. Gao, G. Tu, D. Hasko, S. Hüttner, U. Steiner, N. C. Greenham, R. H. Friend, W. T. S. Huck, *Nano Lett.* **2010**, *10*, 1302.
- [27] D. Mori, H. Benten, I. Okada, H. Ohkita, S. Ito, *Energy Environ. Sci.* **2014**, *7*, 2939.
- [28] M. Schubert, D. Dolfen, J. Frisch, S. Roland, R. Steyrlleuthner, B. Stiller, Z. Chen, U. Scherf, N. Koch, A. Facchetti, D. Neher, *Adv. Energy Mater.* **2012**, *2*, 369.
- [29] C. Mu, P. Liu, W. Ma, K. Jiang, J. Zhao, K. Zhang, Z. Chen, Z. Wei, Y. Yi, J. Wang, S. Yang, F. Huang, A. Facchetti, H. Ade, H. Yan, *Adv. Mater.* **2014**, *26*, 7224.
- [30] Y. J. Kim, C. E. Park, *APL Mater.* **2015**, *3*, 126105.
- [31] H. Yan, Z. Chen, Y. Zheng, C. Newman, J. R. Quinn, F. Dötz, M. Kastler, A. Facchetti, *Nature* **2009**, *457*, 679.
- [32] Y. Xu, C. Liu, D. Khim, Y. Y. Noh, *Phys. Chem. Chem. Phys.* **2015**, *17*, 26553.

- [33] D. Khim, W. H. Lee, K. J. Baeg, D. Y. Kim, I. N. Kang, Y. Y. Noh, *J. Mater. Chem.* **2012**, *22*, 12774.
- [34] L. Ye, S. Zhang, W. Zhao, H. Yao, J. Hou, *Chem. Mater.* **2014**, *26*, 3603.
- [35] M. Saito, I. Osaka, Y. Suzuki, K. Takimiya, T. Okabe, S. Ikeda, T. Asano, *Sci. Rep.* **2015**, *5*, 14202.
- [36] S. Nam, J. Seo, S. Woo, W. H. Kim, H. Kim, D. D. C. Bradley, Y. Kim, *Nat. Commun.* **2015**, *6*, 8929.
- [37] J. Choi, K.-H. Kim, H. Yu, C. Lee, H. Kang, I. Song, Y. Kim, J. H. Oh, B. J. Kim, *Chem. Mater.* **2015**, *27*, 5230.
- [38] K. Zhou, R. Zhang, J. Liu, M. Li, X. Yu, R. Xing, Y. Han, *ACS Appl. Mater. Interfaces* **2015**, *7*, 25352.
- [39] G. Shi, J. Yuan, X. Huang, Y. Lu, Z. Liu, J. Peng, G. Ding, S. Shi, J. Sun, K. Lu, H. Q. Wang, W. Ma, *J. Phys. Chem. C* **2015**, *119*, 25298.
- [40] C. R. McNeill, *Energy Environ. Sci.* **2012**, *5*, 5653.
- [41] W. Kim, J. K. Kim, E. Kim, T. K. Ahn, D. H. Wang, J. H. Park, *J. Phys. Chem. C* **2015**, *119*, 5954.
- [42] J. Zhao, S. Zhao, Z. Xu, B. Qiao, D. Huang, L. Zhao, Y. Li, Y. Zhu, P. Wang, *ACS Appl. Mater. Interfaces* **2016**, *8*, 18231.
- [43] N. K. Zawacka, T. R. Andersen, J. W. Andreasen, L. H. Rossander, H. F. Dam, M. Jørgensen, F. C. Krebs, *J. Mater. Chem. A* **2014**, *2*, 18644.
- [44] Y. Kim, H. R. Yeom, J. Y. Kim, C. Yang, *Energy Environ. Sci.* **2013**, *6*, 1909.
- [45] J. H. Seo, S. Y. Nam, K. S. Lee, T. D. Kim, S. Cho, *Org. Electron.* **2012**, *13*, 570.
- [46] H.-C. Liao, C.-C. Ho, C.-Y. Chang, M.-H. Jao, S. B. Darling, W.-F. Su, *Mater. Today* **2013**, *16*, 326.
- [47] R. Steyrlleuthner, M. Schubert, I. Howard, B. Klaumünzer, K. Schilling, Z. Chen, P. Saalfrank, F. Laquai, A. Facchetti, D. Neher, *J. Am. Chem. Soc.* **2012**, *134*, 18303.
- [48] S. K. Hau, H. L. Yip, N. S. Baek, J. Zou, K. O'Malley, A. K. Y. Jen, *Appl. Phys. Lett.*

- 2008**, 92, 253301.
- [49] S.-I. Na, S.-S. Kim, J. Jo, D.-Y. Kim, *Adv. Mater.* **2008**, 20, 4061.
- [50] S. H. Park, A. Roy, S. Beaupré, S. Cho, N. Coates, J. S. Moon, D. Moses, M. Leclerc, K. Lee, A. J. Heeger, *Nat. Photonics* **2009**, 3, 297.
- [51] H. Hoppe, N. S. Sariciftci, *J. Mater. Res.* **2004**, 19, 1924.
- [52] M. C. Scharber, D. Mühlbacher, M. Koppe, P. Denk, C. Waldauf, A. J. Heeger, C. J. Brabec, *Adv. Mater.* **2006**, 18, 789.
- [53] L. Hong, H. Yao, Z. Wu, Y. Cui, T. Zhang, Y. Xu, R. Yu, Q. Liao, B. Gao, K. Xian, H. Y. Woo, Z. Ge, J. Hou, *Adv. Mater.* **2019**, 31, 1903441.
- [54] H. Sun, T. Liu, J. Yu, T. K. Lau, G. Zhang, Y. Zhang, M. Su, Y. Tang, R. Ma, B. Liu, J. Liang, K. Feng, X. Lu, X. Guo, F. Gao, H. Yan, *Energy Environ. Sci.* **2019**, 12, 3328.
- [55] L. Ye, H. Hu, M. Ghasemi, T. Wang, B. A. Collins, J. H. Kim, K. Jiang, J. H. Carpenter, H. Li, Z. Li, T. McAfee, J. Zhao, X. Chen, J. L. Y. Lai, T. Ma, J. L. Bredas, H. Yan, H. Ade, *Nat. Mater.* **2018**, 17, 253.
- [56] L. Ye, S. Li, X. Liu, S. Zhang, M. Ghasemi, Y. Xiong, J. Hou, H. Ade, *Joule* **2019**, 3, 443.
- [57] D. Bilby, B. Frieberg, S. Kramadhati, P. Green, J. Kim, *ACS Appl. Mater. Interfaces* **2014**, 6, 14964.
- [58] D. Alemu, H. Y. Wei, K. C. Ho, C. W. Chu, *Energy Environ. Sci.* **2012**, 5, 9662.
- [59] K. S. Chen, J. F. Salinas, H. L. Yip, L. Huo, J. Hou, A. K. Y. Jen, *Energy Environ. Sci.* **2012**, 5, 9551.
- [60] Z. Hu, J. Zhang, Z. Hao, Y. Zhao, *Sol. Energy Mater. Sol. Cells* **2011**, 95, 2763.
- [61] T. M. Brown, J. S. Kim, R. H. Friend, F. Cacialli, R. Daik, W. J. Feast, *Appl. Phys. Lett.* **1999**, 75, 1679.
- [62] B. Ecker, J. C. Nolasco, J. Pallarés, L. F. Marsal, J. Posdorfer, J. Parisi, E. von Hauff, *Adv. Funct. Mater.* **2011**, 21, 2705.

- [63] K. W. Wong, H. L. Yip, Y. Luo, K. Y. Wong, W. M. Lau, K. H. Low, H. F. Chow, Z. Q. Gao, W. L. Yeung, C. C. Chang, *Appl. Phys. Lett.* **2002**, *80*, 2788.
- [64] M. P. De Jong, L. J. Van Ijzendoorn, M. J. A. De Voigt, *Appl. Phys. Lett.* **2000**, *77*, 2255.
- [65] M. Qiu, D. Zhu, X. Bao, J. Wang, X. Wang, R. Yang, *J. Mater. Chem. A* **2016**, *4*, 894.
- [66] W. Xu, Y. Liu, X. Huang, L. Jiang, Q. Li, X. Hu, F. Huang, X. Gong, Y. Cao, *J. Mater. Chem. C* **2016**, *4*, 1953.
- [67] S. Murase, Y. Yang, *Adv. Mater.* **2012**, *24*, 2459.
- [68] S. Chambon, L. Derue, M. Lahaye, B. Pavageau, L. Hirsch, G. Wantz, *Materials (Basel)*. **2012**, *5*, 2521.
- [69] K. Majhi, L. Bertoluzzi, K. J. Rietwyk, A. Ginsburg, D. A. Keller, P. Lopez-Varo, A. Y. Anderson, J. Bisquert, A. Zaban, *Adv. Mater. Interfaces* **2016**, *3*, 1500405.
- [70] A. Abdellaoui, L. Martin, A. Donnadiou, *Phys. Status Solidi* **1988**, *109*, 455.
- [71] Y. Gong, Y. Dong, B. Zhao, R. Yu, S. Hu, Z. Tan, *J. Mater. Chem. A* **2020**, *8*, 978.
- [72] Z. Tan, D. Qian, W. Zhang, L. Li, Y. Ding, Q. Xu, F. Wang, Y. Li, *J. Mater. Chem. A* **2013**, *1*, 657.
- [73] J. Yuan, Y. Zhang, L. Zhou, G. Zhang, H. L. Yip, T. K. Lau, X. Lu, C. Zhu, H. Peng, P. A. Johnson, M. Leclerc, Y. Cao, J. Ulanski, Y. Li, Y. Zou, *Joule* **2019**, *3*, 1140.
- [74] K. Jiang, Q. Wei, J. Y. L. Lai, Z. Peng, H. K. Kim, J. Yuan, L. Ye, H. Ade, Y. Zou, H. Yan, *Joule* **2019**, *3*, 3020.
- [75] W. T. Hadmojo, F. T. A. Wibowo, D. Y. Ryu, I. H. Jung, S. Y. Jang, *ACS Appl. Mater. Interfaces* **2017**, *9*, 32939.
- [76] S. Nho, G. Baek, S. Park, B. R. Lee, M. J. Cha, D. C. Lim, J. H. Seo, S. H. Oh, M. H. Song, S. Cho, *Energy Environ. Sci.* **2016**, *9*, 240.
- [77] V. Gonzalez-Pedro, E. J. Juarez-Perez, W. S. Arsyad, E. M. Barea, F. Fabregat-Santiago, I. Mora-Sero, J. Bisquert, *Nano Lett.* **2014**, *14*, 888.
- [78] J. Bisquert, I. Mora-Sero, F. Fabregat-Santiago, *ChemElectroChem* **2014**, *1*, 289.

- [79] W. O. George, *Spectrochim. Acta Part A Mol. Spectrosc.* **1971**, *27*, 265.
- [80] S. F. Tayyari, F. Milani-nejad, *Spectrochim. Acta - Part A Mol. Biomol. Spectrosc.* **2000**, *56*, 2679.
- [81] S. Pinchas, B. L. Silver, I. Laulicht, *J. Chem. Phys.* **1967**, *46*, 1506.
- [82] J. Sun, G. Yu, L. Liu, Z. Li, Q. Kan, Q. Huo, J. Guan, *Catal. Sci. Technol.* **2014**, *4*, 1246.
- [83] M. R. Pedrosa, J. Escribano, R. Aguado, V. Díez, R. Sanz, F. J. Arnáiz, *Polyhedron* **2007**, *26*, 3695.
- [84] G. Guzman, B. Yebka, J. Livage, C. Julien, *Solid State Ionics* **1996**, *86–88*, 407.
- [85] J. Mendez-Vivar, A. Campero, J. Livage, C. Sanchez, *J. Non. Cryst. Solids* **1990**, *121*, 26.
- [86] L. Seguin, M. Figlarz, R. Cavagnat, J. C. Lassègues, *Spectrochim. Acta Part A Mol. Biomol. Spectrosc.* **1995**, *51*, 1323.
- [87] M. R. Pedrosa, R. Aguado, V. Díez, J. Escribano, R. Sanz, F. J. Arnáiz, *Eur. J. Inorg. Chem.* **2007**, *2007*, 3952.
- [88] F. Cheng, Y. Wu, Y. Shen, X. Cai, L. Li, *RSC Adv.* **2017**, *7*, 37952.
- [89] J. W. Rabalais, R. J. Colton, A. M. Guzman, *Chem. Phys. Lett.* **1974**, *29*, 131.
- [90] N. Tokmoldin, S. M. Hosseini, M. Raoufi, L. Q. Phuong, O. J. Sandberg, H. Guan, Y. Zou, D. Neher, S. Shoaee, *J. Mater. Chem. A* **2020**, *8*, 7854.
- [91] S. Li, C.-Z. Li, M. Shi, H. Chen, *ACS Energy Lett.* **2020**, *5*, 1554.
- [92] G. Terán-Escobar, J. Pampel, J. M. Caicedo, M. Lira-Cantú, *Energy Environ. Sci.* **2013**, *6*, 3088.
- [93] J. He, Y. Wan, P. Gao, J. Tang, J. Ye, *Adv. Funct. Mater.* **2018**, *28*, 1802192.
- [94] J. P. Thomas, K. T. Leung, *Adv. Funct. Mater.* **2014**, *24*, 4978.
- [95] W. Song, X. Fan, B. Xu, F. Yan, H. Cui, Q. Wei, R. Peng, L. Hong, J. Huang, Z. Ge, *Adv. Mater.* **2018**, *30*, 1800075.

- [96] A. K. K. Kyaw, D. H. Wang, V. Gupta, J. Zhang, S. Chand, G. C. Bazan, A. J. Heeger, *Adv. Mater.* **2013**, *25*, 2397.
- [97] S. K. Hau, H. L. Yip, A. K. Y. Jen, *Polym. Rev.* **2010**, *50*, 474.
- [98] H. N. Tran, S. Park, F. T. A. Wibowo, N. V. Krishna, J. H. Kang, J. H. Seo, H. Nguyen-Phu, S. Jang, S. Cho, *Adv. Sci.* **2020**, *7*, 2002395.
- [99] K. Zilberberg, S. Trost, J. Meyer, A. Kahn, A. Behrendt, D. Lützenkirchen-Hecht, R. Frahm, T. Riedl, *Adv. Funct. Mater.* **2011**, *21*, 4776.
- [100] J. Cheng, X. Ren, H. L. Zhu, J. Mao, C. Liang, J. Zhuang, V. A. L. Roy, W. C. H. Choy, *Nano Energy* **2017**, *34*, 76.
- [101] Z. Yi Wang, S. H. Lee, D. H. Kim, J. H. Kim, J. G. Park, *Sol. Energy Mater. Sol. Cells* **2010**, *94*, 1591.
- [102] S. Seo, I. J. Park, M. Kim, S. Lee, C. Bae, H. S. Jung, N. G. Park, J. Y. Kim, H. Shin, *Nanoscale* **2016**, *8*, 11403.
- [103] S. Pereira, A. Gonçalves, N. Correia, J. Pinto, L. Pereira, R. Martins, E. Fortunato, *Sol. Energy Mater. Sol. Cells* **2014**, *120*, 109.
- [104] G. Hu, L. Yang, Z. Yang, Y. Wang, X. Jin, J. Dai, Q. Wu, S. Liu, X. Zhu, X. Wang, T. C. Wu, R. C. T. Howe, T. Albrow-Owen, L. W. T. Ng, Q. Yang, L. G. Occhipinti, R. I. Woodward, E. J. R. Kelleher, Z. Sun, X. Huang, M. Zhang, C. D. Bain, T. Hasan, *Sci. Adv.* **2020**, *6*, 5029.
- [105] H. Xu, H. Xu, F. Yuan, D. Zhou, X. Liao, L. Chen, Y. Chen, Y. Chen, *J. Mater. Chem. A* **2020**, *8*, 11478.
- [106] H. Aqoma, I. F. Imran, F. T. A. Wibowo, N. V. Krishna, W. Lee, A. K. Sarker, D. Y. Ryu, S. Jang, *Adv. Energy Mater.* **2020**, *10*, 2001188.
- [107] Y. Kim, A. M. Ballantyne, J. Nelson, D. D. C. Bradley, *Org. Electron.* **2009**, *10*, 205.
- [108] Z. Liu, S. Niu, N. Wang, *J. Colloid Interface Sci.* **2018**, *509*, 171.
- [109] D. H. Kim, J. Ryu, F. T. A. Wibowo, S. Y. Park, J. Y. Kim, S. Y. Jang, S. Cho, *ACS Appl. Energy Mater.* **2020**, *3*, 8375.
- [110] A. K. K. Kyaw, D. H. Wang, C. Luo, Y. Cao, T.-Q. Nguyen, G. C. Bazan, A. J.



- Heeger, *Adv. Energy Mater.* **2014**, *4*, 1301469.
- [111] X. Song, N. Gasparini, L. Ye, H. Yao, J. Hou, H. Ade, D. Baran, *ACS Energy Lett.* **2018**, *3*, 669.
- [112] P. C. Chen, S. H. Yang, *ACS Appl. Energy Mater.* **2019**, *2*, 6705.
- [113] J. You, L. Meng, T. Bin Song, T. F. Guo, W. H. Chang, Z. Hong, H. Chen, H. Zhou, Q. Chen, Y. Liu, N. De Marco, Y. Yang, *Nat. Nanotechnol.* **2016**, *11*, 75.
- [114] E. Von Hauff, *J. Phys. Chem. C* **2019**, *123*, 11329.
- [115] M. Kröger, S. Hamwi, J. Meyer, T. Riedl, W. Kowalsky, A. Kahn, *Appl. Phys. Lett.* **2009**, *95*, 123301.
- [116] Irfan, H. Ding, Y. Gao, C. Small, D. Y. Kim, J. Subbiah, F. So, *Appl. Phys. Lett.* **2010**, *96*, 243307.
- [117] J. H. Lee, J. Kim, G. Kim, D. Shin, S. Y. Jeong, J. Lee, S. Hong, J. W. Choi, C. L. Lee, H. Kim, Y. Yi, K. Lee, *Energy Environ. Sci.* **2018**, *11*, 1742.
- [118] E. M. Speller, A. J. Clarke, J. Luke, H. K. H. Lee, J. R. Durrant, N. Li, T. Wang, H. C. Wong, J. S. Kim, W. C. Tsoi, Z. Li, *J. Mater. Chem. A* **2019**, *7*, 23361.
- [119] X. Song, N. Gasparini, M. M. Nahid, S. H. K. Paleti, J. L. Wang, H. Ade, D. Baran, *Joule* **2019**, *3*, 846.

## Publication List

- [1] Nho, Sungho, Do Hui Kim, Sujung Park, **Hong Nhan Tran**, Bogyu Lim, and Shinuk Cho. "Carbazole and rhodanine based donor molecule with improved processability for high performance organic photovoltaics." *Dyes and Pigments* 151 (2018): 272-278.
  
- [2] **Tran, Hong Nhan**, Do Hui Kim, Sujung Park, and Shinuk Cho. "The effect of various solvent additives on the power conversion efficiency of polymer-polymer solar cells." *Current Applied Physics* 18, no. 5 (2018): 534-540.
  
- [3] **Tran, Hong Nhan**, Sujung Park, Febrian Tri Adhi Wibowo, Narra Vamsi Krishna, Ju Hwan Kang, Jung Hwa Seo, Huy Nguyen-Phu, Sung-Yeon Jang, and Shinuk Cho. "17% Non-Fullerene Organic Solar Cells with Annealing-Free Aqueous MoO<sub>x</sub>." *Advanced Science* 7, no. 21 (2020): 2002395.
  
- [4] **Tran, Hong Nhan**, Duc Quang Dao, Yung Jin Yoon, Yun Seop Shin, Jin San Choi, Jin Young Kim, and Shinuk Cho. "Inverted polymer solar cells with annealing-free solution-processable NiO." *Small* (2021): 2101729.

## Patent

- [1] **Patent Number:** 10-2238865  
**Title of the Invention:**  
저온 용액 공정이 가능한 벌크 헤테로정션 고분자 태양 전지 및 이의 제조방법  
Bulk heterojunction polymer solar cell capable of low temperature solution process, and preparation method thereof
  
- [2] **Patent Number:** 10-2021-0037650 (Submitted)  
**Title of the Invention:**  
니켈 산화물 용액 및 이를 이용한 열처리가 필요없는 태양전지의 제조방법  
Nickel oxide solution and a method of manufacturing a solar cell that does not require annealing using the same

## Korean Abstract

고분자 태양전지 계면 엔지니어링을 위한 가공성이 향상된 전이금속산화물 개발

울산대학교 대학원  
물리학과  
전홍난

고분자 태양전지는 가볍고 유연하며 제조 공정이 간단하고 생산 단가가 낮다는 장점들을 바탕으로 실리콘 기반 태양전지를 대체할 차세대 태양전지로 주목받고 있다. 고품질의 새로운 유기 반도체 광활성층 물질의 합성에 힘입어 최근 non-fullerene 태양전지는 18% 이상의 높은 광전 변환 효율을 기록하고 있다. 추가적인 소자 성능 및 안전성 향상을 위해서는 양질의 광활성층 물질의 개발뿐 아니라, 고분자 광활성층과 전극 사이의 계면에서 일어나는 전하의 수송과 분리를 효과적으로 제어하는 연구도 필요하다. 전이금속 산화물은 고분자 태양전지의 전하수송층 (또는 전극 계면층)으로써 널리 이용되고 있다. 예를 들면 ZnO, SnO<sub>2</sub> 와 같은 물질들은 전자 수송층으로, V<sub>2</sub>O<sub>5</sub>, WO<sub>3</sub>, NiO 와 같은 물질들은 정공 수송층으로 이용된다. 그러나 졸-겔(sol-gel) 방법으로 제작되는 전이금속 산화물 층은 유기 리간드를 제거하기 위해 200 도 이상의 고온 열처리 공정을 거쳐야 한다. 하지만, 유연 기판은 100 도 이상의 온도를 견디지 못하기 때문에 고온 공정이 필수적인 현재의 전이금속 산화물은 유연 소자 산업에 적용하기 힘들다. 따라서 유연 고분자 태양전지 제작에 활용할 열처리 공정이 필요 없는 (annealing-free) 전이금속 산화물 층에 대한 연구가 필요하다.

본 논문에서는 용액 공정 기반의 산화 몰리브덴 (MoO<sub>x</sub>)과 산화 니켈 (NiO)을 새롭게 개발하여 고분자 태양전지의 정공수송층에 적용하였다. MoO<sub>x</sub>와 NiO 층은 열처리 공정 없이도 우수한 정공 수송 특성을 보였다.

Chapter 1에서는 고분자 태양전지의 기본 원리와 고분자 태양전지의 특성을 분석하는 다양한 방법들에 대하여 간단히 소개하였다.

Chapter 2에서는 1-chloronaphthalene, 1,8-diiodoctane, diphenyl ether 의 세 solvent additive 가 PTB7-Th:P(NDI2OD-T2) 벌크 이종접합(bulk-heterojunction;

BHJ) 기반 고분자-고분자 태양전지 소자의 성능에 미치는 영향을 조사하였다. Solvent additive 를 사용한 경우와 그렇지 않은 경우 태양전지 소자의 효율을 직접적으로 비교하였을 때 solvent additive 를 사용한 소자의 성능이 소폭 개선되었다. 그러나 소자 성능이 크게 증가하진 않았는데, 이는 Additive 의 최적의 비율이 특성에 따라 달랐기 때문으로 판단되었다. 게다가, 고분자-고분자 태양전지의 성능은 additive 의 종류에 크게 의존하지도 않았다. 최적 제작 조건을 찾는 것은 최고 효율을 달성하기 위해 중요하다. 일반적으로 BHJ 기반 고분자 태양전지의 광활성층에서 solvent additive 의 역할은 모폴로지를 조절하여 donor 와 acceptor 사이의 상 분리가 잘 이루어지도록 유도하는 것으로 알려져 있다. 그러나 grazing-incidence wide-angle X-ray scattering(GIWAXS) 분석 결과 additive 에 의한 고분자-고분자 광활성층에서 모폴로지의 변화는 크지 않았다. 그보다, modulated impedance spectroscopy 분석을 통해 additive 를 사용한 고분자-고분자 태양전지의 성능 향상이 재결합 특성 향상에 의한 것으로 분석되었다.

Chapter 3에서는 새로운 annealing-free  $\text{MoO}_x$  정공수송층을 개발하였다. 일반적으로 무수 졸-겔 방법으로 제작된 금속 산화물 기반의 전하수송층은 공기 중에서 고온의 열처리 공정을 거쳐야 품질을 확보할 수 있다. 열처리는 실험실에서 수행하기에는 간단한 공정이지만, roll-to-roll 공정과 같이 대량 생산에 적용하려면 가열된 기판을 식히기 위한 공정을 추가적으로 필요로 하기 때문에 간단하지 않다. 따라서 고분자 태양전지의 대규모 상업화를 위해서는 annealing-free 용액 공정 금속 산화물 개발이 필수적이다. 이러한 이유로 상온에서 공정 가능한 annealing-free 수용성  $\text{MoO}_x$  용액을 새롭게 개발하였고, non-fullerene Y6 기반의 (PBDB-T-2F:Y6) BHJ 고분자 태양전지에 적용하였다. 졸-겔 방법으로 제작한  $\text{MoO}_x$  precursor 에

물을 첨가해 가수분해를 유도하여 우수한 전기적 특성을 갖는 annealing-free  $\text{MoO}_x$  정공수송층을 성공적으로 개발하였다. 무수 졸-겔 방법으로 제작한 일반적인  $\text{MoO}_x$  층을 열처리 없이 적용하였을 때 PBDB-T-2F:Y6 non-fullerene 태양전지는 7.7%의 낮은 효율을 보였다. 이러한  $\text{MoO}_x$  층을 200°C 에서 열처리하면 17.1%의 효율을 보이는데, 이는 PBDB-T-2F:Y6 non-fullerene 정구조 태양전지 소자에서 일반적으로 나타나는 값이다. 그러나 수용성  $\text{MoO}_x$  층을 사용한 소자는 열처리 공정

없이도 17.0%의 효율을 보여, 고온에서 열처리 공정을 거친 소자와 비견될 만한 성능을 보였다. 게다가, annealing-free 수용성  $\text{MoO}_x$ 를 적용한 태양전지 소자는 고온 열처리 공정 없이도 PEDOT:PSS를 사용한 소자와 비교하여 성능과 안정성이 더욱 향상되었다.

Chapter 4에서는 새로운 annealing-free 용액 공정이 가능한 NiO를 개발하여 정구조와 역구조 non-fullerene 고분자 태양전지에 모두 적용하였다. 일반적으로 NiO는 본질적 p-type 물질로 동작하며 열적·화학적 안정성이 높아 역구조 유기태양전지의 정공수송층으로 사용할 수 있는 가능성이 매우 높다. 그러나 이러한 NiO는 물을 용매로 하여 습윤성 문제가 있고, 고온에서의 열처리 공정을 필요로 하여 유기태양전지에 적용이 어려웠다. 습윤성 문제를 극복하기 위해, 일반적으로 사용되는 deionized(DI) water 용매를 isopropyl alcohol과 DI water 혼합물로 대체하고 소량의 2-butanol을 첨가하였다. 새로이 개발된 NiO nanoparticle suspension(s-NiO)으로 소수성 광활성층 표면에 고품질의  $\text{NiO}_x$  박막을 성공적으로 형성시킬 수 있었다. PTB7-Th (p-type 고분자)와 IEICO-4F (non-fullerene)를 기반으로 한 역구조 non-fullerene 태양전지에 s-NiO를 정공수송층으로 적용한 결과  $\text{MoO}_x$ 를 열증착법으로 제작한 기존의 역구조 유기태양전지의 성능과 비슷한 11.23%의 효율을 달성하였다. 또한 정구조 유기태양전지에서 정공수송층으로 PEDOT:PSS 대신 s-NiO를 적용하였을 때에도 유사한 효율을 보였다.

## Acknowledgments

First of all, I would like to respectfully thank my supervisor, Professor Shinuk Cho for his valuable guidance, encouragement, and support during my Ph.D. study at the University of Ulsan. It has been my great happiness to complete my Ph.D. study under his guidance.

I would like to express my sincere thanks to my thesis committee members: Professor Sunglae Cho (University of Ulsan), Professor Young-Han Shin (University of Ulsan), Professor Jung Hwa Seo (Dong-A University), and Dr. Dong Chan Lim (Korea Institute of Materials Science) for their valuable time, insightful comments, and suggestions on my Ph.D. thesis.

I would like to thank all Professors of the Department of Physics at the University of Ulsan for their lectures and supports during my courses.

I express my sincere gratitude for the financial supports of Brain Korea 21 Plus (BK21+), the Energy Harvest Storage Research Center (EHSRC), and the University of Ulsan.

I would like to express my warm gratitude to my labmates in the Organic Electronic Physics Laboratory (OEPL) for the insightful discussions, encouragement, helps, and memorable moments during my study.

I would like to thank all co-authors for their discussions and helps in my publications.

Last but not least, I would like to thank my wife and my daughter, my beloved parents, and my beloved parents-in-law for their encouragement, support, and love.

Ulsan, August 2021

Hong Nhan Tran